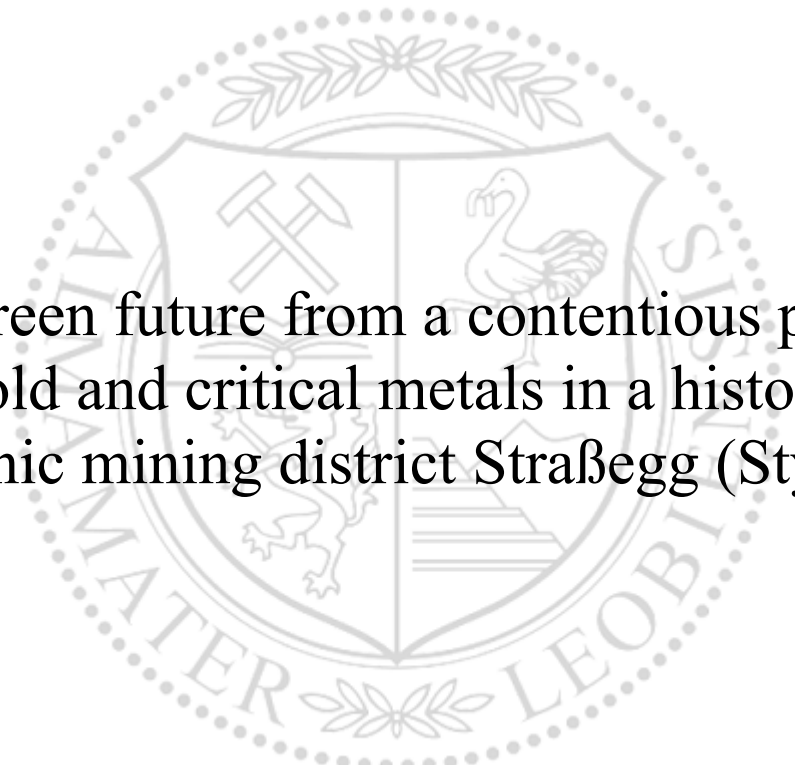




Chair of Geology and Economic Geology

Master's Thesis



A green future from a contentious past:  
Gold and critical metals in a historic  
arsenic mining district Straßegg (Styria)

Jasmin Maren Hiller, B.Sc.

May 2024

Vorgelegt von:

Jasmin Mareen Hiller, BSc

Betreuer:

Univ.-Prof. Mag.rer.nat. Dr. mont Frank Melcher

Dr. Phillip Gopon



**MONTANUNIVERSITÄT LEOBEN**  
www.unileoben.ac.at

**EIDESSTATTLICHE ERKLÄRUNG**

Ich erkläre an Eides statt, dass ich diese Arbeit selbstständig verfasst, andere als die angegebenen Quellen und Hilfsmittel nicht benutzt, den Einsatz von generativen Methoden und Modellen der künstlichen Intelligenz vollständig und wahrheitsgetreu ausgewiesen habe, und mich auch sonst keiner unerlaubten Hilfsmittel bedient habe.

Ich erkläre, dass ich den Satzungsteil „Gute wissenschaftliche Praxis“ der Montanuniversität Leoben gelesen, verstanden und befolgt habe.

Weiters erkläre ich, dass die elektronische und gedruckte Version der eingereichten wissenschaftlichen Abschlussarbeit formal und inhaltlich identisch sind.

Datum 22.05.2024

Unterschrift Verfasser/in  
Jasmin Mareen Hiller

## Acknowledgments

First and foremost, I would like to thank my supervisor, Dr. Phillip Gopon, for his time, guidance, and patience, without whom this thesis would not have been possible. I extend my gratitude to the Chair of Geology and Economic Geology, especially Univ.-Prof. Mag.rer.nat. Dr.mont Frank Melcher, for enabling this research, to Ivaylo Martinov for preparing the samples, and to Dr. mont. Viktor Bertrandsson Erlandsson for his assistance with the LA-ICP-MS and for the insightful discussions.

I greatly appreciate the Chair of Resource Mineralogy for providing access to the EPMA and Raman laboratories. Special thanks go to Dr. rer. nat. Monika Feichter and Ao. Univ.-Prof. Ronald Bakker for their assistance and support.

I wish to thank Dr. Catherine Mottram of the University of Portsmouth for her patience and supervision during the U-Pb dating.

I am also thankful to Mag. Dr. Hans-Peter Bojar and Thomas Brunner for their support throughout my master's thesis, particularly with the field work.

Furthermore, I much appreciate the assistance of Brigitte Mang and Christiane Pretzenbacher in administrative matters.

I owe a very special thanks to Martin Pregler for his unwavering support, encouragement, and empathic ear throughout my academic journey. And, of course, to my mother for always being such a source of strength.

Finally, I am filled with gratitude and joy for the unforgettable time and support I received from my friends during my studies, especially Ann-Cristin, Sandra, David, Sabrina, Nadine, and Philipp.



## Abstract

To reach Europe's ambitious goals for the "Green Deal", the supply of resources to build the Green Energy Infrastructure needs to be assured. At this moment, recycling is not able to handle the exponential increase in demand for precious and critical raw materials. Therefore, it is still necessary to explore new and alternative sources of these metals. At Straßegg (Styria, Austria) an abandoned medieval As-Ag-Au mining district contains several mine waste dumps with up to 14,000 tonnes of material. The main sulfide minerals in the deposit are arsenopyrite, chalcopyrite, and pyrite as well as several sulfosalts such as boulangerite, bournonite, and galena. Due to the limited ore processing ability in previous centuries, the deposit and its waste still contain abundant precious metals and critical raw materials.

The potential of sulfide minerals to host critical and precious metals is already known from Carlin-type Au-deposits, orogenic gold and epithermal deposits. These elements are incorporated as inclusions, nanoparticles, or in the crystal structures of the sulfide mineral. Pyrite is especially known for its ability to incorporate Au, Ag, As, Co, Cu, Ga, Ge and Ni into the crystal structure by the substitution of  $S^{2-}$  or  $Fe^{2+}$  with  $As^{2+/2-}$ . A distortion of the lattice as well as partial charge imbalances allow the incorporation of metals. Arsenopyrite is also capable of incorporating various metals, when the ratio of Fe:As:S is disturbed and Au, Co, Mn, Ni, Sb, Se and Te might be incorporated. Chalcopyrite is a potential host for Ag, Bi, Cd, Co, Ga, Hg, In, Mn, Pb, Se, Sb, Sn, Tl and Zn.

This thesis applies a combination of whole rock geochemistry and trace element mapping to identify element correlations and zonation patterns to better understand the evolution of the deposit and its potential as a source of critical metals. Arsenopyrite appears to be a host for Au, Co, Ni, Pb and Sb. Pyrite contains appreciable Au, As, Co and Ni. The trace metal content is generally related to an elevated amount of As in arsenopyrite and pyrite. Chalcopyrite is enriched in Ag, In, Pb and Zn.

The thesis highlights several ore stages for Straßegg, beginning with an Fe-rich fluid, followed by an As-rich fluid, and finally a Pb-Sb-Ag rich one. Each of these main stages has been subdivided into a series of substages depending on the element correlations noted in the element maps.

Additionally, U/Pb age dating was conducted on calcite veins from Straßegg and Flatschach, another historical mining district in the Eastern Alps, to compare the temporal evolution of mineralization in the Eastern Alps. Due to the high content of common Pb in Straßegg calcite, the age dating was unsuccessful, while those from Flatschach provided ages spanning from the Oligocene to the Pliocene.

## Kurzfassung

Um das ambitionierte „Green Deal“ Ziel Europas zu erreichen, muss die Versorgung mit Ressourcen, welche den Ausbau der grünen Energieinfrastruktur unterstützen sollen, sichergestellt werden. Durch Recycling allein ist es zu diesem Zeitpunkt nicht möglich, die exponentiell steigende Nachfrage nach kritischen Rohstoffen zu decken. Daher ist es noch immer notwendig, neue und alternative Quellen für Metalle zu erschließen.

In Straßegg (Steiermark, Österreich) befinden sich in einem stillgelegten mittelalterlichen As-Ag-Au-Bergbaubezirk noch mehrere Abraumhalden mit bis zu 14.000 Tonnen Material. Die wichtigsten Sulfidminerale in der Lagerstätte sind Arsenopyrit, Chalkopyrit und Pyrit sowie verschiedene Sulfosalze wie Boulangerit, Bournonit und Galenit. Aufgrund der begrenzten Erzverarbeitungsmöglichkeiten in den vorherigen Jahrhunderten enthalten die Lagerstätte und ihre Halden noch reichlich Edelmetalle und kritische Rohstoffe.

Kritische Metalle sowie Edelmetalle in Sulfiden sind bereits aus Carlin-Au-Lagerstätten, orogenen Goldlagerstätten und epithermalen Lagerstätten bekannt. Diese Elemente sind in Form von Einschlüssen, Nanopartikeln oder in den Kristallstrukturen der Sulfidminerale enthalten. Insbesondere Pyrit ist für seine Fähigkeit bekannt, Au, Ag, As, Co, Cu, Ga, Ge und Ni durch die Substitution von  $S^{2-}$  oder  $Fe^{2+}$  durch  $As^{2+/2-}$  in die Kristallstruktur einzubauen. Eine Verzerrung des Gitters sowie partielle Ladungsungleichgewichte ermöglichen den Einbau der Metalle. Auch Arsenopyrit ist in der Lage, verschiedene Metalle wie Ag, Bi, Cd, Co, Ga, Hg, In, Mn, Pb, Se, Sb, Tl und Zn einzubauen, wobei das Verhältnis von Fe:As:S verändert wird.

In dieser Masterarbeit wird eine Kombination aus geochemischen Gesamtgesteinsanalysen und Verteilungsbildern („mapping“) von Spurenelementen in Sulfidmineralen angewandt, um die Elementkorrelationen und Zonierungsmuster zu ermitteln und somit die Entwicklung der Lagerstätte sowie ihr Potenzial als Quelle kritischer Metalle zu verstehen. Arsenopyrit scheint ein Wirtsmineral für Au, Co, Ni, Pb und Sb zu sein. Pyrit enthält nennenswerte Gehalte an Au, As, Co und Ni. Chalkopyrit ist angereichert an Ag, Pb und Zn. Der Gehalt an Spurenmetallen ist im Allgemeinen mit einem erhöhten Gehalt an As in Pyrit und Arsenopyrit verbunden.

Zudem wurden neue Phasen der Vererzung für Straßegg beschrieben, beginnend mit einem Fe-reichen Fluid, gefolgt von einem As-reichen und schließlich einem Pb-Sb-Ag-reichen Fluid. Jede dieser Phasen wurde in eine Reihe von Unterphasen unterteilt, die von den in den Verteilungsbildern verzeichneten Elementkorrelationen abhängen.

Des Weiteren wurden U/Pb-Altersdatierungen an Kalzitgängen aus Straßegg und Flatschach, einem weiteren historischen Bergbaubezirk in den Ostalpen, durchgeführt, um die zeitliche Entwicklung der Mineralisationen in den Ostalpen zu verstehen. Aufgrund des hohen Gehalts an common Pb im Kalzit von Straßegg war die Altersdatierung erfolglos, während die Altersdatierung aus Flatschach Alter von Oligozän bis zum Pliozän ergab.

# Table of contents

<b>1 Introduction</b>	<b>1</b>
<b>2 Geographic location and Geology</b>	<b>3</b>
2.1 <i>Geographic location</i>	3
2.2 <i>Regional Geology-Tectonostratigraphic framework of the Paleozoic of Graz</i>	3
2.2.1 General tectonic setting of the Graz Paleozoic nappe complex	3
2.2.2 Metamorphic conditions at the Graz Paleozoic nappe complex	5
2.3 <i>Lithologies of Straßegg</i>	6
2.3.1 Hochschlag formation	7
2.3.2 Waitzbauer formation	7
2.3.3 Pramerkogel formation	9
2.3.4 Heilbrunn formation	9
2.4 <i>Ore mineralization in Straßegg</i>	9
2.5 <i>Mining history of Straßegg</i>	11
2.6 <i>Geology of Flatschach (Murtal deposit)</i>	12
<b>3 Methods</b>	<b>14</b>
3.1 <i>Sample location</i>	15
3.1.1 Sample location of Flatschach	15
3.2 <i>Whole rock geochemistry</i>	15
3.3 <i>Optical Microscopy</i>	17
3.4 <i>Scanning electron microscopy (SEM)</i>	17
3.5 <i>Electron beam microprobe (EPMA)</i>	17
3.6 <i>Laser ablation-induced coupled plasma mass spectrometry (LA-ICP-MS)</i>	18
3.6.1 Element mapping on pyrite	18
3.6.2 Chalcopyrite trace element spot analysis	18
3.7 <i>Carbonate U-Pb age dating</i>	19
<b>4 Results</b>	<b>21</b>
4.1 <i>Sample location</i>	21
4.2 <i>Whole rock geochemistry</i>	23
4.2.1 Qualitative results of the whole rock geochemistry	23
4.2.2 Element correlations of the whole rock geochemistry results	26
4.3 <i>Petrography</i>	32
4.3.1 <i>Petrographic descriptions of samples</i>	36
22JH07a	36
22JH07b	37
22JH08a	37
22JH09a	38
22JH09b	39
22JH10	39
22JH14a	40
22JH14b	41
22JH14c	42

22JH29b	42
22JH31a	43
22JH34b	43
A0976	44
A0977	45
A0978	45
A0979	45
A0980	45
A0981	46
A0982	46
<b>4.4 EPMA maps element maps of arsenopyrite</b>	<b>48</b>
4.4.1 EPMA element map 22JH08a	48
4.4.2 EPMA element map 22JH07b	50
4.4.3 EPMA element map 22JH14b-map 1	52
4.4.4 EPMA element map 22JH14b-map 2	55
4.4.5 EPMA element map 22JH10	55
<b>4.5 LA-ICP-MS element maps of pyrite</b>	<b>58</b>
4.5.1 LA-ICP-MS element map 22JH31a	58
4.5.2 LA-ICP-MS element map A0982-map 1	60
4.5.3 LA-ICP-MS element map A0982-map 2	61
4.5.4 LA-ICP-MS element map 22JH14b-map 1	63
4.5.5 LA-ICP-MS element map 22JH14b-map 2	63
<b>4.6 Chalcopyrite in-situ spot analyses</b>	<b>67</b>
<b>4.7 U/Pb age dating</b>	<b>69</b>
4.7.1 U/Pb age dating Straßegg 22JH11a	69
4.7.2 U/Pb age dating Flatschach	70
22GS52a	70
22GS52b	70
22GS52d	71
F562	71
FL-CA-1	72
F441	74
FL-AG-1	75
4.7.3 U/Pb reference material	78
4.6.3.1 Primary reference material	78
4.6.3.2 Secondary reference material	78
<b>5 Discussion</b>	<b>79</b>
<b>5.1 Major and trace element geochemistry and microscopy</b>	<b>79</b>
5.1.1 Element distribution	79
5.1.2 Major element zoning in arsenopyrite and implications for substitution mechanisms	79
5.1.3 Major element zoning in pyrite and implication for substitution mechanisms	80
5.1.4 Evolution of the mineralization and genetic model	81
5.1.4.1 Pre-ore stage and ore stage 1	81
5.1.4.2 Ore stage 2	83
5.1.4.2.1 Cd:Zn ratio in chalcopyrite	84
5.1.4.3 Ore stage 3	85
5.1.4.4 Post-ore stage remobilization	85
<b>6 Conclusion</b>	<b>90</b>

<b>Abbreviations</b>	<b>95</b>
<b>List of Figures</b>	<b>96</b>
<b>List of Tables</b>	<b>100</b>
<b>Appendix</b>	<b>101</b>
<b>Electronic Appendix</b>	<b>103</b>

# 1 Introduction

The demand for new technology has rapidly increased since the European 'Green Deal' was first announced by the European Commission 2019, which aims to make Europe the first climate-neutral continent. To achieve positive movement in the direction of climate neutrality, it is necessary to transition resource strategy to a circular economy model.

Waste minimization and improved recycling processes are of course key components of sustainable industry. Yet, the necessity for raw materials remains prevalent. Technical reprocessing standards are still in their infancy and products have a comparatively long life-cycle. Developing new strategies to reactivate an idle supply source through the reprocessing of landfills and old mine tailings would allow new Critical Raw Materials (CRM) and Strategic Raw Material (SRM) to be obtained (Mathieux *et al.*, 2017), while also decreasing climate-critical factors, such as CO<sub>2</sub>-emissions, associated with opening a new mine. Abandoned mining districts still provide resources in their tailing systems, which are easily to access, due to the fact, that the material is already excavated from the bedrock.

340 abandoned Cu-Au-As mining districts are known in Austria alone (see IRIS data-base, Weber *et al.*, 2019), in addition to two active metallic ore mine operations. Straßegg is one such historic mining district. Located in the Eastern Alps in the state of Styria, it is described as an epithermal quartz-vein type deposit with Au-As-Ag mineralization and is hosted in greenschists of the Pramerkogel unit in the Graz Paleozoic Nappe system. Traces of mining activity and several mine waste facilities are still exposed in the abandoned mining area (Antes, 1998; Bojar *et al.*, 2001; Modl *et al.*, 2022). According to Bojar *et al.* (2001), the Straßegg deposit is characterized by two main stages of ore mineralization: an initial arsenopyrite and pyrite-dominated stage, followed by a later stage of mineralization involving various Pb sulfides.

Previous research has indicated the aptitude for both pyrite and arsenopyrite to host trace elements including Ag, As, Bi, Co, Cu, Hg, Ni, Pb, PGEs, Sb, Se, Te, Tl and Zn (Reich *et al.*, 2005; Deditius *et al.*, 2014; Gopon *et al.*, 2019; Wu *et al.*, 2019; Mavrogonatos *et al.*, 2020). Chemically distinct element zonation is a well-known occurrence in arsenopyrite, especially involving Au, Co, Mn, Ni, Sb, Se, and Te (Cook *et al.*, 2013; Fougereuse *et al.*, 2016). A similar propensity has been observed in chalcopyrite, especially for Ag, Bi, Cd, Co, Ga, Hg, In, Mn, Pb, Se, Sb, Sn, Tl and Zn (George *et al.*, 2018; Torró *et al.*, 2022).

In 2023, the European Commission published a list of CRMs And SRMs, which included a multitude of ore metals, including As, Bi, Co, Ni, Sb, known to be commonly hosted in arsenopyrite, chalcopyrite, and pyrite. Given the genesis of the Straßegg deposit, it is plausible that several of these critical elements occur in the pyrite minerals present, and furthermore, due to inadequate historical ore processing methods and economic interest, there is a high potential for mine tailings in Straßegg to be enriched in these overlooked precious metals.

This thesis explores this theory through the thorough analysis of samples obtained from mine tailings in Straßegg. Bulk rock geochemistry aims to establish distinct CRM and ore mineralization trends. Trace element concentrations and signatures of Straßegg arsenopyrites, chalcopyrites and pyrites are investigated with optical microscopy, coupled with scanning electron microscopy (SEM), laser ablation induced coupled plasma mass spectrometry (LA-ICP-MS), and electron probe microanalysis (EPMA). It was intended to first quantify the trace elements, and then to determine their distribution in the

various sulfide minerals. Finally, due to the sparsity of mineralization ages in the Eastern Alps, U/Pb age dating of vein calcite was systematically performed in order to establish temporal and geological correlations between the Straßegg deposit and the additional historic mining district of Flatschach in Styria.

## 2 Geographic location and Geology

### 2.1 Geographic location

Straßegg is a mountain pass northeast of Graz which connects the Mur and Feistritz River valleys (State of Styria, Austria; Figure 1). The ridge at the top of that pass separates the townships of Breitenau am Hochlantsch and Gasen. Straßegg is part of the Eastern Alps, more specific within the Fischbacher Alpen. The former mining area is situated on the northern side of the mountain Pramerkogel (Figure 4). The mining area comprises a near continuous band of mining remnants that is 1.8 km in length and 300 m in width. Within this band numerous traces of historic mining activity in the form of old adits, exploration pits and mine waste piles can be found (Antes, 1998; Modl *et al.*, 2022).



Figure 1: Straßegg (marked with a red dot) in Styria (in green) in Austria; (Basemap: OSM, 2023).

### 2.2 Regional Geology-Tectonostratigraphic framework of the Paleozoic of Graz

#### 2.2.1 General tectonic setting of the Graz Paleozoic nappe complex

The historic mining district Straßegg is located within the Upper Austroalpine Nappe System. The nomenclature of the nappes and units of this nappe system are heavily debated, this study uses the most recent terminology after Schmid *et al.* (2004). In this nomenclature the Upper Austroalpine is separate from detached Mesozoic and Paleozoic sediments of the Northern Eastern Alps (Schmid *et al.*, 2004).

The Upper Austroalpine is comprised of four nappe systems. In order from the structurally highest to the lowest: the Drauzug-Gurktal nappe, the Ötztal-Bundschuh nappe, the Koralpe-Wölz high-pressure nappe and the Silvretta-Seckau nappe. The Drauzug-Gurktal nappe system is subdivided in the Graz Paleozoic nappe, the Gurktal nappe as well as the Steinach nappe (Schmid *et al.*, 2004). Straßegg is contained within the Graz Paleozoic nappe (Bojar *et al.*, 2001; Modl *et al.*, 2022).

The Graz Paleozoic nappe complex has an aerial extent of approximately 1250 km<sup>2</sup> (Ebner *et al.*, 2001) and is between 1 to 2 km thick (Gasser *et al.*, 2010). The nappe complex is bounded in the northeast by the Anger Crystalline Complex. The southeast margin is the Radegund Crystalline complex and the



Styrian Basin (Figure 2), which is comprised of Neogene sediments. The margin to the southwest is the Koralm Crystalline Complex and the northwest by the Gleinalm Crystalline Complex. Parts of the western Graz Paleozoic nappe complex are overlain by the Cretaceous Gosau extensional basin (Ebner *et al.*, 2001; Krenn *et al.*, 2008; Gasser *et al.*, 2010). The surrounding and/or basal crystalline of Graz Paleozoic nappe are described by Gasser *et al.* (2010) as high-grade metamorphosed during the Permian to Cretaceous.

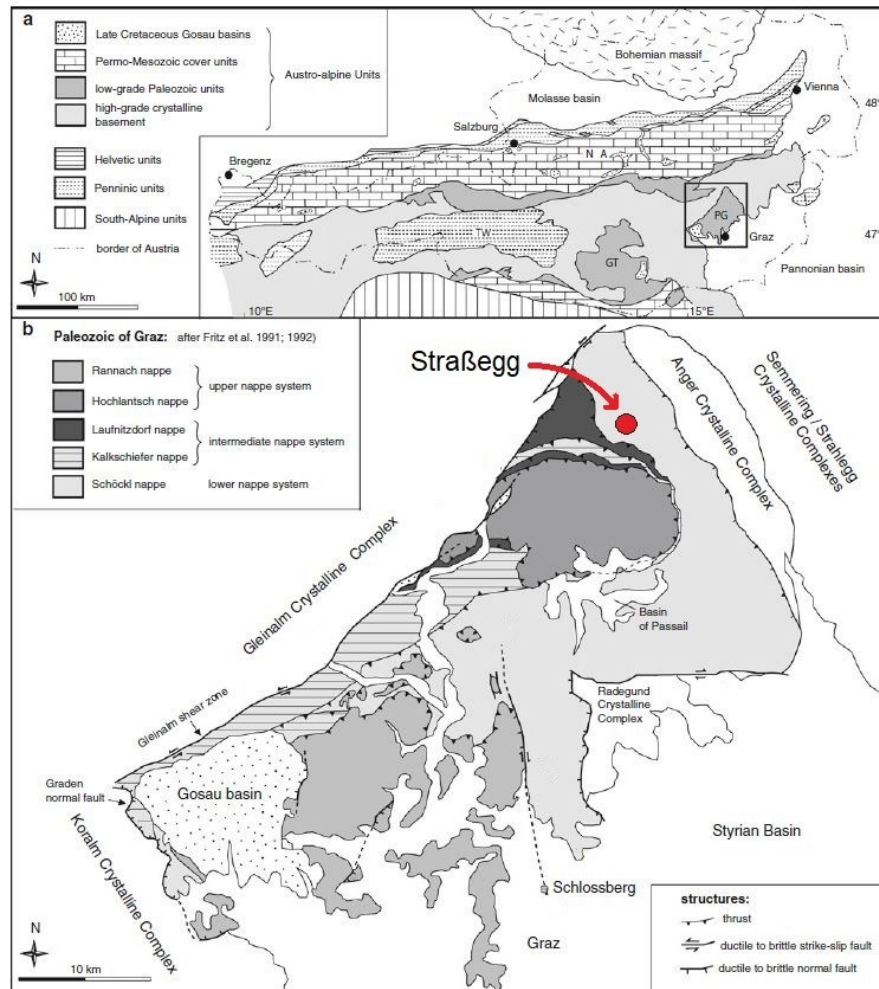


Figure 2: The Graz Paleozoic modified after Gasser *et al.* (2010); a) shows an overview of the tectonic units of the Eastern Alps; b) shows the Graz Paleozoic nappe complex. The red dot marks the location of Straßegg.

Gasser *et al.* (2010) suggest splitting the Grazer Paleozoic nappe complex into an upper and a lower nappe, separated by the Rannach thrust (Figure 2). Previous research proposed three nappe complexes (Ebner *et al.*, 2001; Rantitsch *et al.*, 2005), but in this thesis the nomenclature after Gasser *et al.* (2010) is used. The upper nappe system is comprised of the following sedimentary facies Rannach, Hochlantsch and Kalkschiefer; while the lower nappe contains the Schöckl, Laufnitzdorf, and parts of the Kalkschiefer facies (Figure 2; Figure 3). The Rannach thrust cuts the structural features of the lower nappe system in some parts and is therefore considered to be younger than these units. The upper nappe systems has an general fold axis trend E-W and NE-SW, while the lower nappe systems has a E-W lineation (Gasser *et al.*, 2010).

In total 35 sedimentary formations are discerned in the Graz Paleozoic nappe complex by Flügel & Hubmann (2000) which are summarized by Gasser *et al.* (2010) into 13 rock units.

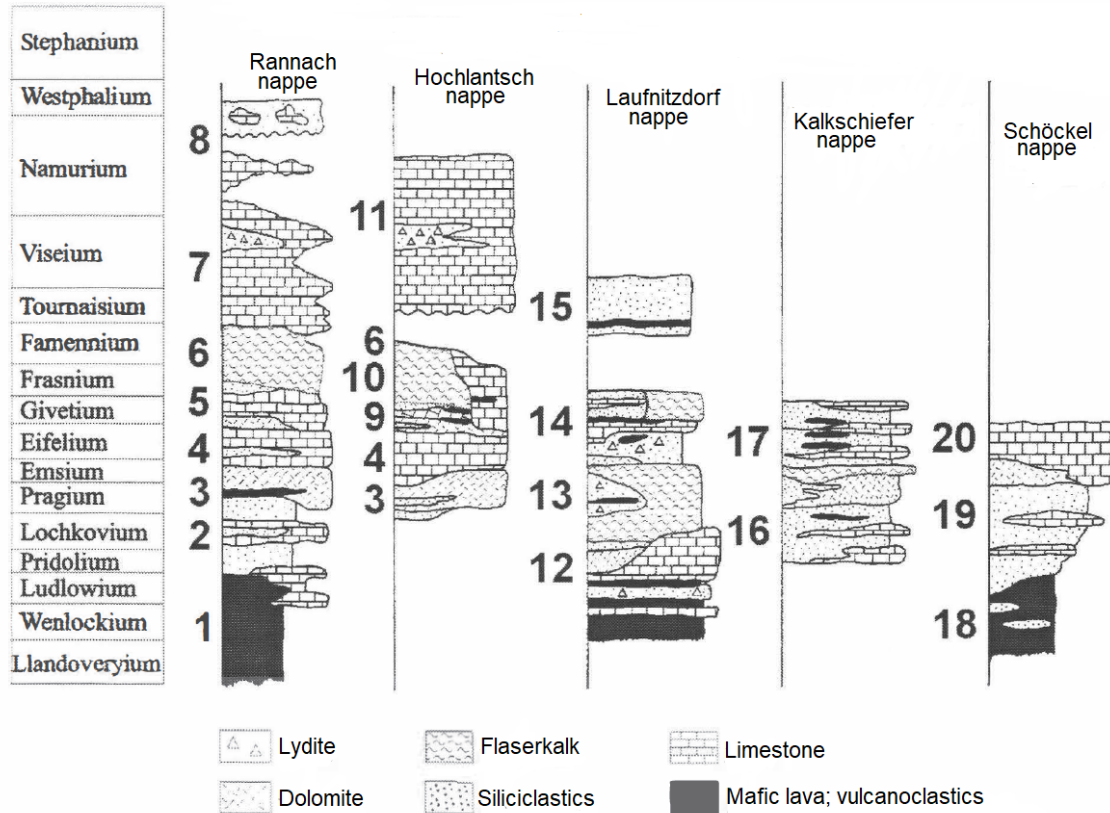


Figure 3: Nappes and units of the Graz Paleozoic nappe complex modified after Ebner *et al.* (2001), formation is abbreviated with fm. Straßegg is part of the Schöckel nappe (Bojar *et al.*, 2001); 1) Kehr-fm., Kötschberg fm.; 2) Parmasegg fm.; 3) Flösserkogel fm., Bameder fm.; 4) Barrandeikalk; 5) Kollerkogel fm.; 6) Steinberg fm.; 7) Sanzenkogel fm.; 8) Höchkogel fm.; 9) Tyrnaueralm fm.; 10) Zachenspitze fm., Hochlantsch fm.; 11) Bärenschtütz fm.; 12) Hackensteiner fm., 13) Harrberger fm.; 14) St. Jakob fm.; 15) Dornerkogel fm.; 16) Kogler fm.; 17) Hubenhalt fm.; 18) Taschen fm.; 19) Schönberg fm.; 20) Schöckel fm., Hochschlag fm.

## 2.2.2 Metamorphic conditions at the Graz Paleozoic nappe complex

The rocks of Graz Paleozoic nappe complex consist of low-grade greenschist metamorphic rocks of Silurian to Carboniferous age (Rantitsch *et al.*, 2005; Krenn *et al.*, 2008; Gasser *et al.*, 2009). The oldest Silurian rocks consist of volcanoclastic sediments produced by intracontinental rifting and high Silurian volcanism (Flügel & Hubmann, 2000; Rantitsch *et al.*, 2005; Krenn *et al.*, 2008; Gasser *et al.*, 2010). The environment changes to coastal facies resulting in sandy limestones and dolomitic rock during the earlier Devonian. In the late Devonian to Carboniferous the Graz Paleozoic nappe complex was dominated by pelagic limestone (Gasser *et al.*, 2010). The pressure and temperature conditions for the metamorphic overprinting for the different facies increases from the uppermost to the lowest nappe system. Temperatures vary between 200 to 300°C for the upper to above 300°C for the lower units (Gasser *et al.*, 2010). Rantitsch *et al.* (2005) determined higher temperatures of 500±50°C at the margins of the Graz Paleozoic nappe complex.

The formation of the Eastern Alps can be attributed to two significant collisional events during the Cretaceous and Paleogene. Variscan (Late Carboniferous) influence on the Graz Paleozoic nappe complex is not evident (Rantitsch *et al.*, 2005). The possibility of Variscan metamorphism is suggested by results of  $^{40}\text{Ar}/^{39}\text{Ar}$  age-dating in muscovite (Carboniferous) of the Gurktal nappe system. Variscan mica in sediments are deposited in karstified rock of the upper nappe system of the Graz Paleozoic nappe complex and could therefore be evidence for the age. The characteristic Permo-mesozoic sediments which are used to differentiate between Variscan and Eo-alpine metamorphism in the Eastern Alps, are not present in the Graz Paleozoic nappe complex (Gasser *et al.*, 2010).

The formation of the nappe stack of the Graz Paleozoic nappe complex is suggested to have occurred during an early Cretaceous thrusting and NW compressional event during the Alpine orogeny (Neubauer *et al.*, 1995; Bojar *et al.*, 2001; Krenn *et al.*, 2008). Bojar *et al.* (2001) discerned an age of 120 Ma for the event from syn-kinematically grown minerals in shear zones of the compression. Evidence that the stacking occurred before the late Santonian/early Campanian is comes from the deposition of the Kainach basin sediments above the thrust structure of the Graz Paleozoic nappe complex (Neubauer *et al.*, 1995; Rantitsch *et al.*, 2005). Additional Rb/Sr and K/Ar age dating indicates an early Cretaceous age of the Graz Paleozoic nappe complexing as well (Neubauer *et al.*, 1995). Neubauer *et al.* (1995) suggested peak metamorphic (greenschist) condition with a lower intercept U/Pb age at  $139 \pm 6$  Ma utilizing zircon dating.

However Gasser *et al.* (2010) mentioned that age-dating did not confirm an Eo-Alpine thrusting event so far because the bulk of all age data of the Graz Paleozoic shows that the time period covers an variable interval from  $\sim 90$  to  $\sim 240$  Ma. Therefore, the authors are not convinced by a Cretaceous deformation. Research by Rantitsch *et al.* (2005) suggested a Permian burial causing a metamorphic overprint of the Graz Paleozoic nappe stack.

A late Cretaceous extensional event, which is coupled within the formation of the Kainach Gosau basin and the exhumation of the Gleinalm crystalline affected the area of the Graz Paleozoic nappe complex. Ar/Ar dating on mica and hornblendes dated the Kainach Gosau basin to 100 to 80 Ma (Neubauer *et al.*, 1995; Bojar *et al.*, 2001).

### 2.3 Lithologies of Straßegg

Lithologic names and descriptions for Straßegg are similarly debated, and herein we primarily use the terms and description from Bojar *et al.* (2001). The area of Straßegg is part of the Schöckel nappe, which belongs to the lower nappe complex of the Graz Paleozoic nappe complex (Bojar *et al.*, 2001). The nappe system is greenschist metamorphic overprinted and subdivided into the Peggau- and Passail groups (Ebner *et al.*, 2001).

The origin of rocks of the Peggau-group varies between euxinic influenced and carbonate sedimentation of pre-Devonian to Devonian age (Flügel & Hubmann, 2000; Ebner *et al.*, 2001). Important for Straßegg are the subdivisions of the Hochschlag formation and the Schönberg formation, as the main mining was within the Waitzbauer member of the latter (Flügel & Hubmann, 2000).

The Passail group is discerned as in pre-Devonian age. Ebner *et al.* (2001) describes abundant sericite phyllites with intercalations of chlorite schist. In Straßegg the Heilbrunn formation can be found, which is subdivided into the Pramerkogel and Heilbrunner complexes (Antes, 1998; Flügel & Hubmann, 2000).

Bojar *et al.* (2001) simplified the occurring lithologies in Straßegg to the Hochschlag, Waitzbauer, Pramerkogel and the Heilbrunn formations. To minimize confusion these formations are used in the Master thesis and are exemplified in the following (Table 1). The strike all units with the Straßegg area is generally NW-SE (Bojar *et al.*, 2001).

Table 1: Petrographic description of the formations in Straßegg modified after Antes (1998) and Bojar *et al.* (2001).

	Abundant Mineralogy	Description
<b>Hochschlag formation</b>	<i>Carbonates</i>	<ul style="list-style-type: none"> <li>▪ Most abundant are limestone and dolomites</li> <li>▪ Intercalations of black shales</li> <li>▪ 800 m thick formation</li> <li>▪ Metamorphose condition: low grade greenschist-facies (&gt;300°C)</li> </ul>
<b>Waitzbauer formation</b>	<i>Black shales</i>	<ul style="list-style-type: none"> <li>▪ Sericite-chlorite phyllites</li> <li>▪ Intercalation of dark limestone and lydites</li> <li>▪ Organic material, pyrite mineralization</li> <li>▪ 200 – 300 m thick formation</li> </ul>
<b>Pramerkogel formation</b>	<i>Metabasic rocks</i>	<ul style="list-style-type: none"> <li>▪ Chlorite-muscovite-albite-carbonate-(biotite) schist</li> <li>▪ Host of the vein type ore mineralization</li> <li>▪ 200 m thick formation</li> </ul>
<b>Heilbrunn formation</b>	<i>Metapelites</i>	<ul style="list-style-type: none"> <li>▪ Muscovite-biotite-chlorite phyllites and chlorite-muscovite-albite-(biotite-garnet) schist</li> <li>▪ 2.5 km thick formation</li> <li>▪ Metamorphic conditions: 450-500°C; 6kbar</li> </ul>

### 2.3.1 Hochschlag formation

Carbonate (both limestones and dolomites) is the main rock type of the Hochschlag formation, with a thickness up to 800 m (Figure 4; Table 1). Intercalations of minor black shales and greenschists are present. The Hochschlag formation has experienced greenschist facies metamorphism above 300°C, as evidenced by illite crystallinity and vitrine reflectivity (Bojar *et al.*, 2001).

### 2.3.2 Waitzbauer formation

Below the Hochschlag formation is the Waitzbauer formation of Devonian age, with a thickness between 200 and 300 m (Figure 4; Table 1; Antes, 1998). Main rock types of the Waitzbauer formation are dark limestones and metavolcanics (such as sericite-chlorite phyllites). Dark coloration of both lithologies is due to the occurrence of graphite. Disseminated pyrite is present in the limestones and metavolcanics (Bojar *et al.*, 2001). The exploration report of the company MINEREX (1987) described no high values of As or any other heavy metals in the black shales of the Waitzbauer formation.



Although there is an ore mineralization in the formation, the exploited ore mineralization occurs as vein type in the Pramerkogel formation (Antes, 1998).

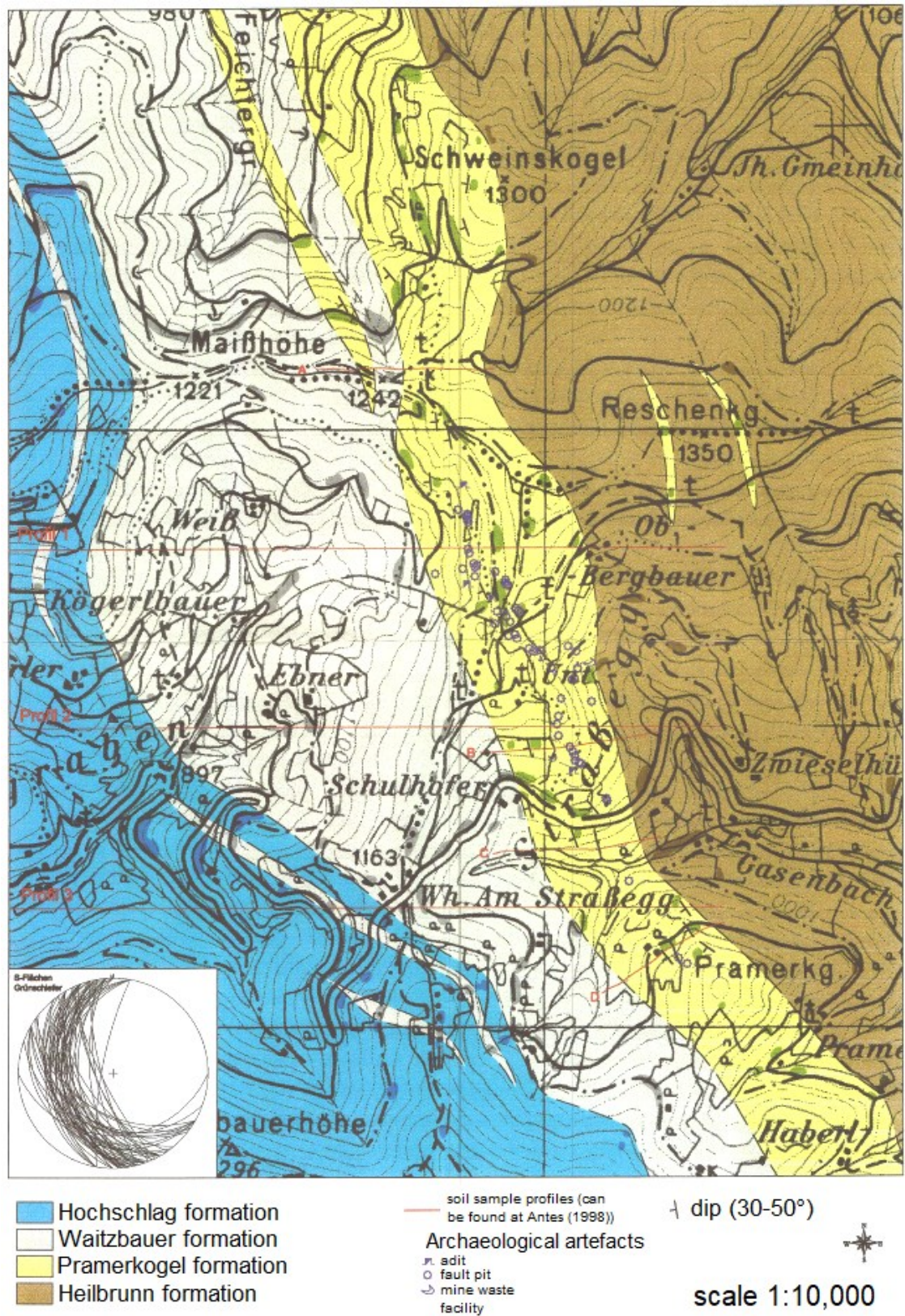


Figure 4: Geological map of Straßegg modified after Antes (1998), mining artefacts can be found within the Pramerkogel formation.

### 2.3.3 Pramerkogel formation

The Pramerkogel formation, with a thickness about maximal 200 m (Figure 4; Table 1; (Antes, 1998)) is the most important formation for the ore mineralization, consisting mostly of high greenschist facies metabasic rocks, indicated by the parageneses of albite-actinolite-epidote-chlorite. Research on hornblende cores suggest a retrograde low grade metamorphic overprinting of a higher (amphibolite facies) grade (Bojar *et al.*, 2001).

Bojar *et al.* (2001) described the unit as chlorite-muscovite-albite-carbonate-(biotite) schists along with subordinate massive albite-chlorite-epidote amphibolite. Heavy minerals, As- and Au concentration are abundant in the greenschist (MINEREX, 1987; Bojar *et al.*, 2001).

### 2.3.4 Heilbrunn formation

Underlying the Pramerkogel formation are the metapelites of the Heilbrunn formation, a 2.5 km thick layer of muscovite-biotite-chlorite-phyllites and chlorite-muscovite-albite(biotite-garnet) schist which is at Straßegg just about 800 m thick (Figure 4; Table 1; (Antes, 1998; Bojar *et al.*, 2001)). Minor metabasic rocks also occur within the Pramerkogel formation, which have undergone metamorphism at around 450-500°C and a pressure of about 6 kbar, based on Mn-zoned garnet (Bojar *et al.*, 2001).

## 2.4 Ore mineralization in Straßegg

The Pramerkogel formation hosts sulfide mineralization with arsenopyrite, pyrite and Pb-Sb-sulfides, as well as electrum. The ore mineralization is restricted to this unit, near the boundary to the overlying Waitzbauer formation, which consists of mainly black shale (Weber, 1990; Antes, 1998; Bojar *et al.*, 2001). The main gangue mineral is quartz, with lesser amounts of calcite. These quartz veins can be up to 1.5 m thick and contain several centimeter-thick, massive sulfide mineralization (MINEREX, 1987). The alteration zone of the veins in the Pramerkogel formation consist of Fe-dolomite, quartz, plagioclase and minor muscovite (Bojar *et al.*, 2001). The folding of the veins is mostly NW-SE striking and cuts the foliation at low angles. Late tectonic activity resulted in the folding of the veins and the foliation. The protolith of these rocks were basalts and tuffs, which underwent low-grade metamorphism to greenschist with formation temperatures of 300 to 350°C (Bojar *et al.*, 2001).

Veins can be found in all four units of Straßegg, but the composition of these is distinct. Depending on the composition of the host rocks, the most abundant veins which occur are quartz with calcite or dolomite in rims of the vein or disseminated. The veins with mixed composition have often a quartz core and are subsequently followed by carbonate and dolomite (Bojar *et al.*, 2001).

The ore mineralization is described in several references since the early 20th century. In one of the first publications, Friedrich (1933) describes the ore mineralization as hydrothermal vein mineralization that started within a quartz gangue mineral, additionally with pyrite and arsenopyrite. Later tectonic movement fractured these minerals as well as chalcopyrite, sphalerite and carbonates crystallized replacing former minerals. The input of antimony (Sb) stopped the processes and the element interacted with Fe and Cu of former phases. Lastly lead entered the system and the galena grew.



In more recent work Bojar *et al.* (2001) suggest two main ore stages (Table 2). Stage one is mainly dominated by Fe- and As-bearing ore minerals like arsenopyrite, gersdorffite, pyrite and pyrrhotite. These minerals occur in quartz veins, as mm-to-centimeter sized crystals. The most abundant ore mineral is arsenopyrite, which is typically fractured, with lesser amounts of pyrite. Gold occurs as electrum in fractures and along grain boundaries (Bojar *et al.*, 1998). Arsenopyrite geothermometer suggests a formation temperature for the first ore stage around 400°C.  $\delta^{34}\text{S}$  values indicate a homogeneous, magmatic source for the S in the vein sulfides (Bojar *et al.*, 2001), likely derived from the greenschist lithologies of the Pramerkogel formation (Bojar *et al.*, 1994). The Au mineralization is thought to have occurred through either rapid cooling or depressurization of the ore fluid. The sulfide mineralization is estimated at 300-350°C based on fluid inclusion thermometry, with estimated pressures between 3.8 to 5.8 kbar (Bojar *et al.*, 2001). Bojar *et al.* (1998) suggested that ore stage one was affected by tectonic activity, which led to the ore minerals often being fractured and deformed. Dominant elements in the second ore stage are Pb and Sb. Significant ore minerals that occur are boulangerite, bournonite, chalcopyrite, galena and jamesonite. The range of additional minerals of the assemblage is wider (Bojar *et al.*, 1998). Ore stage two is associated with this tectonism, filling fractures of crystals of ore stage one with a new generation of ore minerals.

Dating the ore mineralization in Straßegg was not successful in former research. Bojar *et al.* (2001) estimate the mineralization to be related to a late Cretaceous extension event, linked to the exhumation of the Gleinalm crystalline. Antes (1998) provides one  $^{207/206}\text{Pb}$  age of a sample from a mine waste facility of about 145 Ma. With the assumption of the credibility of the obtained age, Antes (1998) suggested a possible mineralization during the alpine orogeny.

Table 2: Paragenetic table of ore stages.

	ore stage 1	ore stage 2
Arsenopyrite	■	
Pyrite	■	
Pyrrhotin	■	
Chalcopyrite		■
Galena		■
Bolangerite		■
Jamseonit		■
Bournonite		■
Tetrahedit		■
Cd-,Ni- and Te-phases		■

Previous research established two different/further? ore mineralization styles (MINEREX, 1987; Bojar *et al.*, 1994; Antes, 1998). This thesis is primarily concerned with the vein-type mineralization concerned but for completeness they are described below.

The second type of ore mineralization occurs outside of the vein system. Arsenopyrite is the most abundant ore mineral occurring as up to two-centimeter-thick euhedral crystals, with minor chalcopyrite and galena. Gold can be found as electrum in fractures (Bojar *et al.*, 1994).

The third mineralization style is a stratabound massive arsenopyrite mineralization with a maximum size of 1 m<sup>2</sup> (Bojar *et al.*, 1994). It occurs at the boundary to the Hochschlag formation and is microscopically highly fractured (Bojar *et al.*, 1994; Antes, 1998).

## 2.5 Mining history of Straßegg

Old Celtic and Roman settlements existed in Straßegg, but the first historic evidence of mining comes in the form of 14<sup>th</sup> century artefacts, when Ag-exploitation started (Bojar, 1989) followed by active mining in the 15<sup>th</sup> century (Modl *et al.*, 2022). Soon after mining for Ag and Au started as well. The main sales market for metals from Straßegg was Venice at this time, exporting As<sub>2</sub>O<sub>3</sub> to the Mediterranean and the Middle East (Bojar, 1989; Modl *et al.*, 2022). Applications for As included the glass industry (especially Murano glass), colour pigment or as Hittrach, an intoxicant used as a performance enhancing drug (Modl *et al.*, 2022).

Arsenic production in Styria had nearly no competitors, with the nearest competition in Freiberg (Saxony, Germany). Therefore the mining in Straßegg had a monopoly in As production for a long time, with the peak of production in the 16<sup>th</sup> century (Modl *et al.*, 2022). One century after the first reference to the mine, the miners complained about the hardness and the low quantity of the rock that they needed to exploit. Due to this loss of competitiveness and a conflict with Venice, Straßegg experienced an economic downturn. The owner was compelled to request a reduction in fees to address the challenges posed by the lengthy transport route (Bojar, 1989).

At the end of the 16<sup>th</sup> century, poor/deadly working conditions and opening of competitor mines in Kothgraben, St. Lambrecht and Rotgülden/Lungau (located in the Eastern Alps) (Bojar, 1989), finally forced the mine almost to close, and only minor production remained. The final abandonment of the mine was in 1826 after dozens of the population died due to “Rote Ruhr” (a disease likely caused by arsenic poisoning from the primitive extraction methods in use). Another re-opening was suggested in 1866, but never happened (Bojar, 1989; Weber, 1990).

In 1986 the company MINEREX started an exploration project on the Au-mineralization in Straßegg with geochemical mapping and trenching. The results were promising with average gold grades between 1-6 ppm reported in trenches over a length of 1-3 m, and hand samples contained up to 40 ppm Au, 202 ppm Ag and 34 % As. High Au content were noted to be related to elevated As (MINEREX, 1987).

Today several archaeological artefacts have been found around Straßegg. Old adits, as well as a sublimation furnace have been uncovered and are still visible (Modl *et al.*, 2022). In addition, there are 45 mine waste dumps in the district with an estimated combined tonnage of 14,000 tn. (see IRIS database, Weber *et al.*, 2019; Schedl & Lipiarski, 2021).



## 2.6 Geology of Flatschach (Murtal deposit)

During the U/Pb dating that was done for this thesis, samples from Straßegg were examined as well as from surrounding districts in the Murtal, such as Flatschach (Figure 5). This was done to understand the role of Straßegg within the wider mineralization that occurs in the area. All deposits investigated belong to the larger ‘Green transformations’ project of which this thesis was funded by. As a result, a brief overview of the geology of the Murtal deposit is given below.

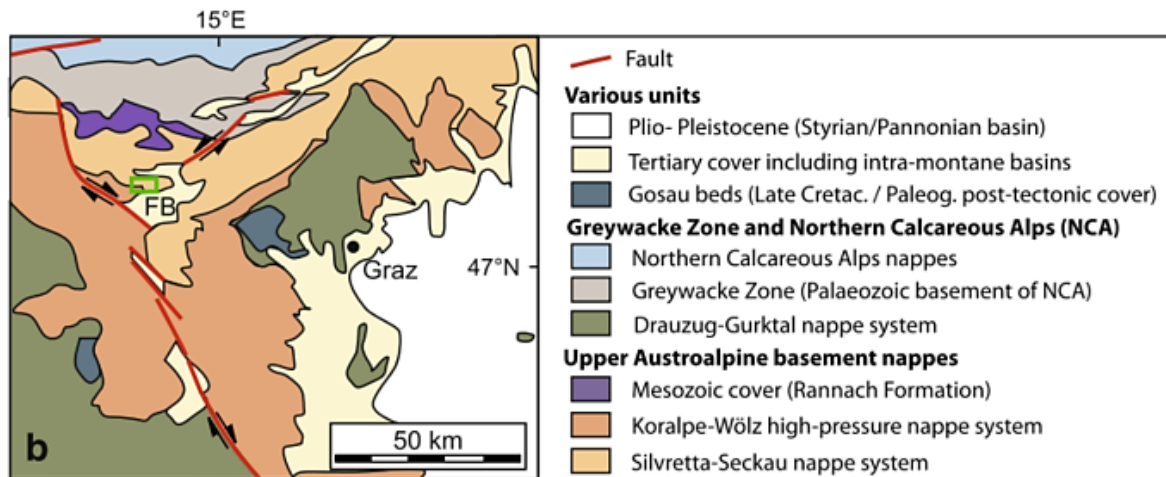


Figure 5: Geologic map of the Murtal after Raith *et al.* (2015); the area of Flatschach is marked within a green box.

The ore mineralization in Flatschach is a structurally controlled Cu-Au-vein type, with a disseminated, patchy or banded character, main gangue minerals are quartz and calcite. The Flatschach mining district is found within the Silvretta-Seckau and the Koralpe-Wölz nappe systems (Raith *et al.*, 2015). These units are part of the base of the Upper Austroalpine nappe complex (Schmid *et al.*, 2004). Three different sub-districts ('Reviere') in Flatschach (Weissenbach, Adlitz and Brunngraben) are known to be the host of eight main ore veins which are thought to be near continuous throughout the district. The veins of the northern districts Weissenbach and Adlitz dip 70-80° degrees NW and strike NE-SW. The veins in the third district, Brunngraben, dip 72-76° degrees SE and strike NNE-SSW. Brunngraben is known for abundant arsenopyrite and pyrite, while chalcopyrite dominates in the districts of Weissenbach and Adlitz. The trend here is that in structurally lower and further west mineralization copper dominates, and structurally higher and further east Au-As dominates. Host rocks of the Cu-Au mineralization are mostly amphibolite, which is massively foliated, as well as biotite gneiss, with a well foliation, and orthogneiss. Because of over unconformably laying sediments of the Neogene the age is estimated to pre-Miocene (Raith *et al.*, 2015).

Raith *et al.* (2015) described three main ore stages, where the first is dominated by Cu-Fe-As sulfides (Figure 6). The second stage is associated with a replacement of minerals of stage one, with abundant Cu-(Fe)-sulfides and Cu-arsenides. Ore stage three comprises supergene weathering, where oxides, hydroxides and copper carbonates formed. Gold mineralization occurs in all three ore stages (Raith *et al.*, 2015).

	Stage 1 Hypogene mesozonal	Stage 2 Hypogene epizonal	Stage 3 Supergene
<b>Ore minerals</b>			
Pyrite	—————		
Arsenopyrite	—————		
Chalcopyrite	—————		
Bornite/ Enargite		-----	
Cu sulfides		—————	—————
Cu arsenides		—————	----- ?
Gold			—————
Copper			—————
Bismuth minerals		-----	
<b>Gangue</b>			
Quartz		-----	-----
Calcite		?	
Dolomite/ankerite	?	—————	----- ?
Oxides /hydroxides		-----	—————

Figure 6: Paragenetic table of the Cu-Au mineralization in Flatschach after Raith et al. (2015).

### 3 Methods

For this work 34 mineralized samples were collected in Straßegg (Figure 7, Figure 8) and supplemented with 7 existing thin sections of the deposit of the collection of the Montanuniversität Leoben.

The samples were crushed and sent to the laboratory Actlabs/Canada for whole rock geochemistry. The idea was to compare the samples and to choose high grade samples for further investigation.

Thereafter, a petrographic investigation was conducted to delineate the features of the different ore mineralization stages. Petrography was conducted using a combination of an optical microscope as well as a scanning electron microscope (SEM). Additionally, the BSE signal in the SEM images was used to detect any heterogeneity/zonation within the grains, so that further investigation with microanalytical techniques would be conducted.

Heterogeneities/zonation were measured with a combination of Electron beam microprobe (EPMA) and the Laser ablation-induced coupled plasma mass spectrometry (LA-ICP-MS). Due to the presence of significant heterogeneity in the minerals, a series of semi-quantitative maps was conducted for representative samples, as well as spot analyses of chalcopyrite with LA-ICP-MS.

Calcite U/Pb age dating was conducted at the University of Portsmouth (UK) and included samples from Flatschach (Styria, Austria), a deposit in the vicinity of Straßegg. The results of the dating are to be compared with each other in order to determine a possible connection between the different ore mineralization locations.

Detailed descriptions of the individual methods can be found below.

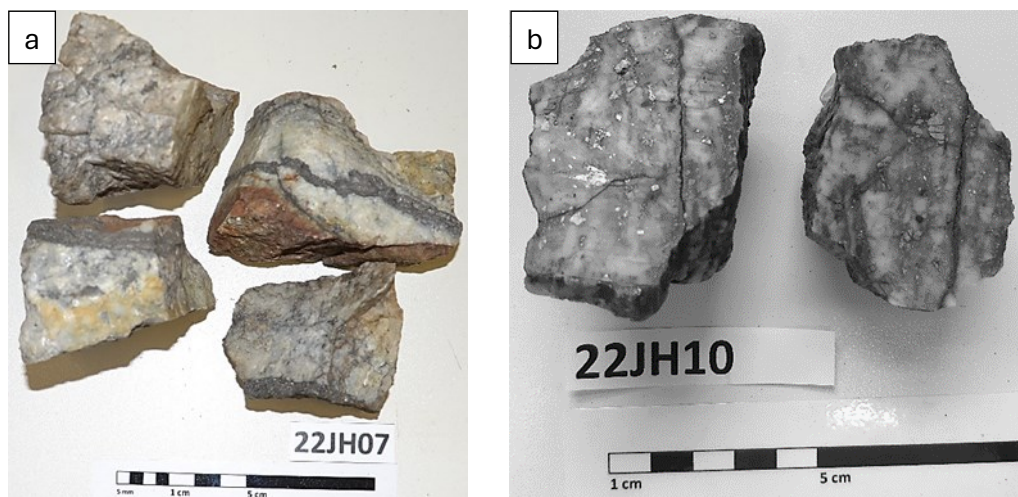


Figure 7: Photos of samples; a) sample 22JH07, which originates of a mine waste facility, shows an ore in quartz; b) sample 22JH10 is a float sample, which shows in quartz disseminated ores. These ores are mostly arsenopyrite, minor pyrite.

### 3.1 Sample location

During a three-day field campaign (in June 2022), 34 samples were collected from the main mining areas (north of the main road; Figure 8) of the historic mining district Straßegg. The samples were collected mostly from mine waste facilities or in areas known to have had former mining activity. These are named as 22JHXXx (first two digits = year; letters = collected initials [Jasmin Hiller]; XX = sample number; x=optional last letter = refer to same sample year, collector and location but subordinated the sample). The samples were selected based on visible ore mineralization.

Additionally, 11 samples were collected by the company AUREX Biomining AG (sample names 21TBXX [TB = Thomas Brunner]) and seven samples were taken from the Paar-Collection of the Montanuniversität Leoben in the form of already prepared polished sections.

The samples by AUREX Biomining AG were collected in both the northern and southern parts of the study area (Figure 8). These were mostly from abandoned waste piles, as well as in the surrounding area of those. The focus of the sampling by the company was the whole district. The samples of the Paar-Collection lack specific GPS-coordinates but were documented to originate from Straßegg.

#### 3.1.1 Sample location of Flatschach

The samples of Flatschach were sampled and provided by Sandra Niederl (currently ongoing MSc. Thesis). These have been used for the U/Pb dating to see whether there is a significant relationship between the deposits Flatschach and Straßegg. The corresponding coordinates can be found in the Table 13.

### 3.2 Whole rock geochemistry

To determine the elements that are present in the sample, whole rock geochemistry analyses were conducted. Independent of this thesis the AUREX Biomining AG conducted whole rock chemistry on two samples (Sample ID 21TB01; 21TB02). For comparison a complete list of elements of all sessions (including the samples of the AUREX Biomining AG) is presented in the appendix.

Two additional whole rock geochemistry sessions were conducted. At first, another eight samples of the company AUREX Biomining AG (Sample ID 21TB03 to 21TB10) in Winter 2021 and second nine samples of the 34 samples collected for this study in Fall 2023. These samples were crushed using an agate mill and sent out for whole rock geochemistry analyses by Actlabs/Canada. The methods used at Actlabs are a combination of Instrumental Neutron Activation Analysis (INAA) with multi-acid digestion ICP and ICP-MS. Some of the send-in samples have been selected to prepare as thin sections as well. Powder splits of these samples will be stored in the collection of the Chair of Geology and Economic Geology for use in further work (Montanuniversität Leoben).

Note, the method as well the detection limits vary between the two laboratories that were used for the analyses of the samples gathered as part of this thesis and the samples that have been analyzed on behalf of AUREX Biomining AG. All plots based on this data use the color scale imola by Crameri (2018) for a reproducible representation of the data.

Table 3: Samples list and which methods were conducted on them marked with an "x".

	whole-rock geochemistry	Epoxide mount	SEM	EPMA	LA-ICP-MS	ccp in-situ spot analysis	U/Pb dating
A0976		x	x				
A0977		x	x				
A0978		x	x				
A0979		x	x				
A0980		x	x				
A0981		x	x				
A0982		x	x		x		
21TB01	x						
21TB02	x						
21TB03	x						
21TB04	x						
21TB05	x						
21TB06	x						
21TB07	x						
21TB08	x						
21TB09	x						
21TB10	x						
22JH01	x						
22JH02	x						
22JH01	x						
22JH02	x						
22JH07a		x	x				
22JH07b		x	x	x			
22JH07c	x						
22JH08a		x	x	x			
22JH09a		x	x				
22JH09b		x	x				
22JH09c	x						
22JH10		x	x	x	x		
22JH11a							x
22JH12	x						
22JH14a		x	x		x		
22JH14b		x	x	xx	x		
22JH14c		x	x				
22JH14c	x						
22JH29b	x	x	x				
22JH31a		x	x		x	x	
22JH32	x						
22JH34a	x						
22JH34b		x	x				

### 3.3 Optical Microscopy

Different ore minerals and their paragenetic stage can be identified by microscopic investigations. Textural features, such as cracks, alterations and mineralization phases are visible. Therefore, samples of 22JHxx and the ones of the Paar-collection were prepared in the Chair of Geology and Economic Geology (Montanuniversität Leoben), using round polished epoxy mounts (22JHxx diameter 4 cm; samples of Paar collection diameter 3 cm) for optical microscopy and further investigation.

To document the optical microscopy results a Keyence VHX 6000 digital microscope was used, provided by the Chair of Geology and Economic Geology (Montanuniversität Leoben). Stitched overview images of the entire slide as well as detailed pictures have been made and are described and discussed in the following chapters.

### 3.4 Scanning electron microscopy (SEM)

To complement the observations of the thin sections by optical microscopy, a Zeiss Evo MA 10 SEM coupled with a Bruker Quantax EDX detector at the Chair of Geology and Economic Geology (Montanuniversität Leoben) was used. Before using the SEM, the samples were coated with a ~20 nm film of carbon using a Polaron Emitech K950X sputter coater. The work conducted on the SEM supported the petrographic description with the optical microscope and gave additional information about the element distribution in the minerals.

The SEM was additionally used to uncover zonation styles in single grains of for example pyrite and arsenopyrite. Different beam conditions and grayscales had to be used for different minerals because of the different backscatter values for the various sulfides investigated.

### 3.5 Electron beam microprobe (EPMA)

EPMA analyses (element maps) were conducted on a JEOL Superprobe JXA 8200 at the Chair of Resource Mineralogy (Montanuniversität Leoben). The EPMA is equipped with a cathodoluminescence detector and 5 WDS spectrometers. Analyses on arsenopyrite were conducted in one session from the 30.10.2023 to 02.11.2023 on selected samples. Analytical conditions are given in Table 4.

Table 4: EPMA spectrometer adjustments for element mapping on arsenopyrite.

spectrometer	WDS			EDS
	Xtal	Xtal	Element (Line)	Element (Line)
1	TAP	LDE1	As (La)	Fe (Ka)
2	TAP	PETJ	Sb (Lb)	S (Ka)
3	LIF	PETJ	Ni (Ka)	As (Ka)
4	LIFH	PETH	Co (Ka)	Pb (La)
5	LIFH	PETH	Au (La)	Ag (La) Cu (Ka)

Conditions: 25keV 80nA

The raw map data from the EPMA was processed in the program ImageJ (Schneider *et al.*, 2012) to emphasize the contrast and differences in the elemental distribution in the element maps. The maps have been edited to change contrast and brightness as well as smoothing or sharpening of the image. As with the LA-ICP-MS, reproducible and reader-friendly element maps are created, using the scientific colour element map batlowW by Crameri (2018). All in all, five quantitative element maps of different sizes were produced.

## 3.6 Laser ablation-induced coupled plasma mass spectrometry (LA-ICP-MS)

### 3.6.1 Element mapping on pyrite

After the observations with the optical microscope and the SEM, single pyrite crystals were analyzed by trace element mapping using an ESI NWR213 Nd:YAG laser ablation system coupled to a Agilent 8800 triple quadrupole ICP-MS, at the Chair of General and Analytical Chemistry, (Montanuniversität Leoben). Arsenopyrite crystals as well as Pb-phases were not analyzed, because of the As and Pb contamination issue. Therefore, the focus of the LA-ICP-MS was on pyrite crystals. The sessions were conducted between the 17.04.2023 to 20.04.2023.

The pyrites have been ablated with a spot size of 50  $\mu\text{m}$  with laser fluency of 2-3  $\text{J}/\text{cm}^2$  with a 10 Hz repetition rate. A 5  $\mu\text{m}$  line scan was used with a scan speed of 3  $\mu\text{m}/\text{s}$ . Carrier gas was He with a flow rate of 0.75 L/min. A 30-second pre-ablation background collection was conducted, followed by 60-seconds of laser ablation and data acquisition. For cell wash-out, a 30-second delay after individual ablation cycles.

All in all, the elements that correlate in the whole rock geochemistry are used to evaluate the distributions of elements between different patterns of the pyrite crystals. The element masses that were analyzed are  $^{57}\text{Fe}$ ,  $^{59}\text{Co}$ ,  $^{60}\text{Ni}$ ,  $^{63}\text{Cu}$ ,  $^{66}\text{Zn}$ ,  $^{71}\text{Ga}$ ,  $^{74}\text{Ge}$ ,  $^{75}\text{As}$ ,  $^{95}\text{Mo}$ ,  $^{107}\text{Ag}$ ,  $^{115}\text{In}$ ,  $^{118}\text{Sn}$ ,  $^{121}\text{Sb}$ ,  $^{125}\text{Te}$ ,  $^{197}\text{Au}$ ,  $^{205}\text{Tl}$ ,  $^{208}\text{Pb}$  and  $^{209}\text{Bi}$ . In addition, spot analyses were made in chalcopyrite to determine the element content (Chapter 3.6.1 Chalcopyrite trace element spot analysis). All in all, five elemental element maps of pyrite were produced and 29 spot analysis in chalcopyrite conducted.

The matrix-matched sulfide standard, therefore Mass-1 was utilized (Wilson *et al.*, 2002). Periodically, the standard was ablated to ensure qualitative data.

The software Lolite 4 was used for the creation of the element maps and data quantification of the mapped elements (Paton *et al.*, 2011). The scientific colour element maps by Crameri (2018) were used to create clear element distributions without any distortion, to make reproducibility possible and to enable good readability even for readers with a colour-vision deficit. The colour element map batlowW was used to prepare the LA-ICP-MS element maps.

### 3.6.2 Chalcopyrite trace element spot analysis

Apart from the element mapping carried out with LA-ICP-MS, in-situ spot analyses on chalcopyrite were conducted. Element masses analyzed are:  $^{51}\text{V}$ ,  $^{52}\text{Cr}$ ,  $^{55}\text{Mn}$ ,  $^{59}\text{Co}$ ,  $^{60}\text{Ni}$ ,  $^{66}\text{Zn}$ ,  $^{71}\text{Ga}$ ,  $^{74}\text{Ge}$ ,  $^{75}\text{As}$ ,  $^{82}\text{Se}$ ,  $^{95}\text{Mo}$ ,  $^{107}\text{Ag}$ ,  $^{111}\text{Cd}$ ,  $^{115}\text{In}$ ,  $^{118}\text{Sn}$ ,  $^{121}\text{Sb}$ ,  $^{125}\text{Te}$ ,  $^{197}\text{Au}$ ,  $^{201}\text{Hg}$ ,  $^{205}\text{Tl}$ ,  $^{208}\text{Pb}$  and  $^{209}\text{Bi}$ . The same ESI NWR213 Nd:YAG laser ablation system coupled to an Agilent 8800 triple quadrupole ICP-MS (Department of Applied Geosciences and Geophysics, Montanuniversität Leoben) was used here as in the trace element



mapping. The chalcopyrite was ablated with a spot size diameter of 50  $\mu\text{m}$  with laser fluency set to 2-3  $\text{J}/\text{cm}^2$ . The repetition rate was about 10 Hz. He served as the carrier gas at a rate of 0.75 L/min. A background collection of 30 seconds was conducted prior to ablation, followed by 60 seconds of laser ablation and data acquisition. Each ablation cycle was succeeded by a 30-second delay for cell wash-out. The data analysis was made within one session.

The matrix-matched sulfide standard, therefore Mass-1 was utilized (Wilson *et al.*, 2002). For quality control the standard MUL-ZnS1 was used (Onuk *et al.*, 2017). Periodically, the standard was ablated to correct for instrumental drift. The reduction of the data was conducted within the software Lolite 4 (Paton *et al.*, 2011).

During the spot analyses, the laser was positioned avoiding fractures, inclusions, or other impurities. Implications of impurities, that still have been hit, were excluded, and are presented in a secondary table. To avoid distorted data by extreme maxima and minima values, P95 and P05 values were used.

### 3.7 Carbonate U-Pb age dating

The samples selected for calcite U-Pb were prepared by the sample preparation laboratory of the Chair of Geology and Economic Geology as polished round epoxy mounts with a diameter of 1 inch. Prior to analyses in Portsmouth, the polished sections were characterized, and the carbonates identified using a combination of optical microscopy, SEM and RAMAN spectroscopy were used. In total, eight samples were examined. At the Chair of Resource Mineralogy (Montanuniversität Leoben) the Raman Horiba LabRAM HR Evolution was used, which is part of the Raman-TERS-AFM laboratory. Mappings of calcite have been done.

In a second step, the U-Pb dating was performed in one analytical session from the 21.11.2022 to 24.11.2022 at the University of Portsmouth (School of Earth and Environmental Science at the University of Portsmouth, UK). An ASI RESOLUTION<sup>©</sup> 193 nm ArF excimer laser coupled to an Agilent 8900 Triple Quad mass spectrometer was used. With working parameters of a 38  $\mu\text{m}$ , 10 Hz,  $\sim 4.5 \text{ J}/\text{cm}^2$  line on NIST612 glass, which yield a typical sensitivity of  $\sim 730,000\text{-}850,000$  cps  $^{238}\text{U}$  and a  $^{202}\text{Hg}$  background of 1500-2000 cps. Helium was used as the carrier gas and the gas flow was set to 0.300 L/min. The plasma generation was set to 1350 W with 15 L/min of Ar plasma flow. Auxiliary gas flow of 0.9 L/min and nebulizer flow of 1.3-1.5 l/min.

The carbonates in the samples were analyzed by using 80  $\mu\text{m}$  spot size, laser fluence of  $\approx 3.0 \text{ J}/\text{cm}^2$  and a repetition rate of 8 Hz. The following masses were measured and had integration time of (10 ms  $^{202}\text{Hg}$ ,  $^{204}\text{Pb}$ ) (20 ms  $^{232}\text{Th}$ ,  $^{235}\text{U}$ ,  $^{238}\text{U}$ ,  $^{208}\text{Pb}$ ), (50 ms  $^{206}\text{Pb}$ ) and (70 ms  $^{207}\text{Pb}$ ).

As primary references SRM614 glass (NIST614; 0.82 ppb U and 2.3 ppb Pb; GEOREM;  $^{238}\text{U}/^{206}\text{Pb}$  ratio of 0.2236;  $^{207}\text{Pb}/^{206}\text{Pb}$  0.8704 and  $^{206}\text{Pb}/^{208}\text{Pb}$  2.0995- GEOREM) and WC-1 carbonate (254.4 $\pm$ 6.4 Ma; Roberts *et al.*, 2017) were used. Mudtank zircon (732 $\pm$ 5 Ma; (Black, L. P., Gulson B.L., 1978; Jackson *et al.*, 2004) and Duff Brown Limestone (64 $\pm$ 2 Ma; Hill *et al.*, 2016) were used as a secondary reference material to test long-term reproducibility. Both, primary and secondary reference materials were ablated between every 8 unknown spots. Analyses of Mudtank during the analytical period yielded a  $^{206}\text{Pb}/^{238}\text{U}$  Concordia age of 726 $\pm$ 3.7 Ma MSWD 1.2 (0.82 % from reported age). Analyses of Duffbrown during the analytical period yielded a  $^{206}\text{Pb}/^{238}\text{U}$  intercept age of 62.08 $\pm$ 0.45 Ma MSWD 2.6 (3 % from reported age).



Before each analysis three pulses of pre-ablation with a 100  $\mu\text{m}$  spot size and a 15 s washout were used to clean. The dataset underwent reduction, with corrections made for background, instrumental U-Pb drift, downhole fractionation (exponential fitting), U/Pb isotope mass bias and peak correction accomplished using Lolite©3.4 software (Paton *et al.*, 2011).

Propagated analytical uncertainties are included in 2 sigma uncertainties. Final quoted uncertainties incorporate an extra 2 % uncertainty added in quadrature to account for typical long-term reproducibility of analytical equipment and reproducibility. For secondary reference material 2 % were added as well.

The data is presented in Wetherill and Tera-Wasserburg plot created by the software IsoplotR (Vermeesch, 2018) and are uncorrected for common Pb.

## 4 Results

### 4.1 Sample location

The samples have been collected in the main mining area of Straßegg (Figure 4). Figure 8 shows an overview of the area and origin of each sample. Table 5 shows the coordinates, the sampler and the type of sample. Samples have been collected adjacent to/ in adits, as float sample or from mine waste facilities.

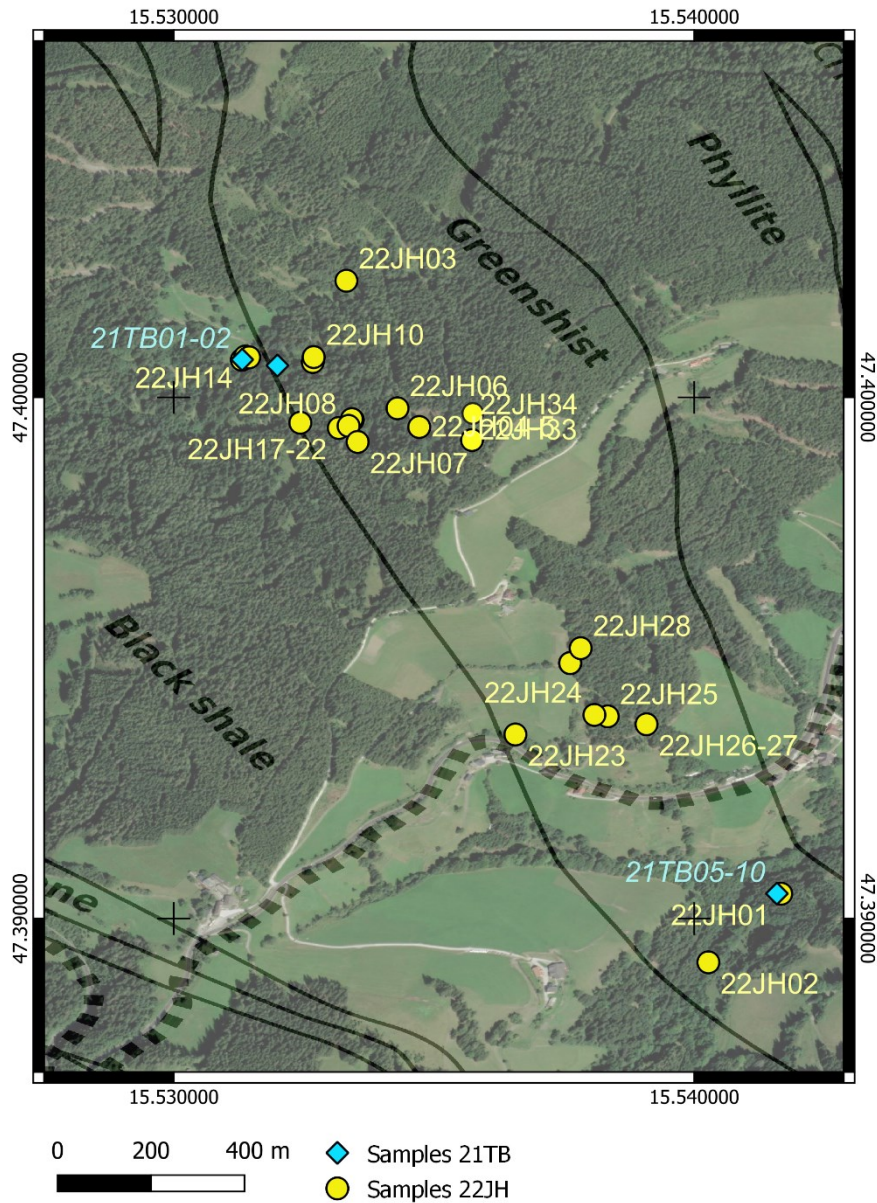


Figure 8: Map of the sample location; Lithology of Straßegg modified after Antes (1998); (Basemap: Esri satellite 2023).

Table 5: Sample ID, location, sampler, and description of the type. Samples of the Paar collection (A0976-A0982) have no distinct coordinates and are described to originate by a mine waste facility.

Sample ID	Latitude	Longitude	Sampler	Type
A0976				Mine waste facility
A0977				Mine waste facility
A0978				Mine waste facility
A0979	Paar-Collection of the Montanuniversität Leoben (no coordinates available)			Mine waste facility
A0980				Mine waste facility
A0981				Mine waste facility
A0982				Mine waste facility
21TB01	47.40072440	15.53131515	Thomas Brunner	Mine waste facility
21TB02	47.40072440	15.53131515	Thomas Brunner	Mine waste facility
21TB03	47.40061222	15.53199249	Thomas Brunner	Mine waste facility
21TB04	47.40061222	15.53199249	Thomas Brunner	Mine waste facility
21TB05	47.39047931	15.54159038	Thomas Brunner	Adit Gasen
21TB06	47.39047931	15.54159038	Thomas Brunner	Adit Gasen
21TB07	47.39047931	15.54159038	Thomas Brunner	Adit Gasen
21TB08	47.39047931	15.54159038	Thomas Brunner	Adit Gasen
21TB09	47.39047931	15.54159038	Thomas Brunner	Adit Gasen
21TB10	47.39047931	15.54159038	Thomas Brunner	Adit Gasen
22JH01	47.39490200	15.53761790	Jasmin Hiller	Adit Gasen
22JH02	47.39446360	15.53812810	Jasmin Hiller	Adit Gasen/ Float sample?
22JH03	47.39390770	15.53808360	Jasmin Hiller	Mine waste facility
22JH04	47.39353190	15.53656500	Jasmin Hiller	Mine waste facility
22JH05	47.39353190	15.53656500	Jasmin Hiller	Mine waste facility
22JH06	47.39941300	15.53317210	Jasmin Hiller	Mine waste facility
22JH07	47.40078460	15.53137460	Jasmin Hiller	Mine waste facility
22JH08	47.39958420	15.53342200	Jasmin Hiller	Mine waste facility
22JH09	47.39951340	15.53243330	Jasmin Hiller	Mine waste facility
22JH10	47.39935600	15.53217820	Jasmin Hiller	Float sample
22JH11	47.40095750	15.53283900	Jasmin Hiller	Float sample
22JH12	47.40076910	15.53145040	Jasmin Hiller	Float sample
22JH13	47.39945420	15.53335980	Jasmin Hiller	Float sample
22JH14	47.39914520	15.53353400	Jasmin Hiller	Float sample
22JH15	47.39929310	15.53373910	Jasmin Hiller	Float sample
22JH16	47.40120180	15.53315770	Jasmin Hiller	Mine waste facility
22JH17	47.39979080	15.53430010	Jasmin Hiller	Mine waste facility
22JH18	47.39979080	15.53430010	Jasmin Hiller	Mine waste facility
22JH19	47.39979080	15.53430010	Jasmin Hiller	Mine waste facility
22JH20	47.39979080	15.53430010	Jasmin Hiller	Mine waste facility
22JH21	47.39979080	15.53430010	Jasmin Hiller	Mine waste facility
22JH22	47.39979080	15.53430010	Jasmin Hiller	Mine waste facility
22JH23	47.39943210	15.53471770	Jasmin Hiller	Mine waste facility
22JH24	47.38916000	15.54027340	Jasmin Hiller	Mine waste facility
22JH25	47.38357880	15.55878590	Jasmin Hiller	Mine waste facility
22JH26	47.38867000	15.54016290	Jasmin Hiller	Mine waste facility
22JH27	47.38867000	15.54016290	Jasmin Hiller	Mine waste facility
22JH28	47.38867040	15.54003300	Jasmin Hiller	Mine waste facility
22JH29	47.39081250	15.54243170	Jasmin Hiller	Mine waste facility
22JH30	47.39128930	15.54391920	Jasmin Hiller	Mine waste facility
22JH31	47.39128930	15.54391920	Jasmin Hiller	Mine waste facility
22JH32	47.39212140	15.54494300	Jasmin Hiller	Mine waste facility
22JH33	47.40120300	15.53645801	Phillip Gopon	Mine waste facility/ Float sample?
22JH34	47.40080430	15.53601911	Phillip Gopon	Mine waste facility/ Float sample?

## 4.2 Whole rock geochemistry

In the following, the results of the whole rock geochemistry is presented. Table 6 shows quantitative whole-rock geochemical results of each sample for selected elements. Complete results of all elements can be found in the appendix. Note that the samples 21TB01 and 21TB02 are analyzed by a different method and are provided by AUREX Biomining AG, therefore detection limits vary between both methods. Results below the detection limits were incorporated into the median by assuming 50 % of the lower detection limit (LOD) as their value. The whole rock geochemical data provide an insight into what elements are present in the rocks from Straßegg, but also the correlations between the elements. This is important for identifying which elements are related to each other in terms of mineralization generation.

In Figure 9, Figure 10, Figure 11 and Figure 12 are different ternary correlation plots where the third elements abundance is indicated by the symbol color.

### 4.2.1 Qualitative results of the whole rock geochemistry

The majority of the samples indicate highly elevated contents of As (Table 6). Most of them exceed the upper detection limit of 10,000 ppm, but a few samples (for example 22JH02 - a float sample collected below a closed adit) show As contents as low as 82.3 ppm. In this sample Cu, Cr, Ni, Mn and Sr content is relatively elevated compared to the other samples.

In general, the content of Au is elevated in the samples where As exceeds the upper detection limit. The maximum content of Au is about 61.7 ppm in sample 21TB01, which is also enriched in Ag, As, Mn, Pb, Sb and Sr. The median Au content of the samples is 6.6 ppm. In general, the content of Ag decreases with decreasing Au content. The maximum Au content is measured in sample 21TB02 with 104 ppm, where the Au content is diminished compared to sample 21TB01. Notable is the high content of Pb in each of these two samples. Together with sample 21TB04 and 22JH34a these samples have Pb values exceeding 5,000 ppm and in general high contents of Ag, As and Au. The median Ag value for all 19 samples is 4.54 ppm and for Pb 202 ppm.

Antimony contents correlate with Pb. The maximum Sb content is about 23,700 ppm in sample 21TB01, which is also highly enriched in As, Au, Mn and Pb. The median Sb value is 506 ppm.

Bismuth contents range from 0.1 to 25.1 ppm (median 0.3 ppm), with two samples having no detectable Bi (LOD 0.1 ppm). When the content of Bi is elevated, Pb contents are also the highest.

In the case of Cd, more than half of the samples are below the detection limits (LOD 0.1 ppm), with the remainder in a range between 0.1 to 7.88 ppm (with a median of 0.05 ppm).

More than half of the data exhibit Cr contents below the detection limit of 0.1 ppm (median value 0.5 ppm). Nevertheless, the content increases in sample 21TB09 (collected in an adit) to a maximum of 504 ppm. Notably Mn is also elevated (5,140 ppm) in this sample.

In general, the content of Mn fluctuates in the samples from several tens up to thousands of ppm. The result is a Mn median value of 91 ppm, with the trend being the less As the more Mn.

Vanadium is enriched in several samples but never exceeds 91 ppm, the median value is 24 ppm. High V correlates with elevated Mn content.

Nickel is often elevated in samples with lower As contents but also with higher Pb content. The maximum Ni content is around 256 ppm (sample 21TB09). Notable is that the As content in this sample is relatively low. Generally, the highest contents of Ni do not correlate with the As-enriched samples. These trends can be more clearly visualized in the correlation plots which are shown in Chapter 4.2.2 *Element correlations of the whole rock geochemistry results*.

The content of Co varies between 2.8 and 84.3 ppm, with five samples below the detection limit. Cobalt's median value is about 12 ppm.

Copper fluctuates between 6.2 and 1,155 ppm, with a median of 14 ppm. Samples with elevated Cu contents also display high Pb levels. The general trend is that with increasing Cu contents the As content is elevated as well, but one of the samples buck this trend and contain substantial Cu but only minor As (sample 22JH02).

The Fe content fluctuates between 1.89 wt% and 34.4 wt%, with a mean of about 15.07 %. Gallium ranges from 0.3 to 14.9 ppm, the median is 2.1 ppm. The Ge content in 16 samples is below 0.5 ppm, with one below the detection limit (LOD Ge = 0.1 ppm). The maximum is 5.8 ppm, the median is 0.3 ppm.

Indium concentrations are similar to that of Ge, as almost half the samples are below the LOD (0.1 ppm), with the rest falling in the range between 0.2 to 3.5 ppm and a median value of 0.2 ppm.

Molybdenum ranges between 1 and 3.1 ppm, the median value is 2 ppm. Only one sample was below the Mo LOD of 1 ppm. Selenium is generally below 10 ppm (median value 4.2 ppm), with one sample below the LOD of 0.1 ppm. Tellurium is also less abundant in these samples, typically below 1 ppm. Four samples are below the LOD of 0.1 ppm, and the median Te value is 0.5 ppm.

Rubidium ranges from 0.098 to 79.3 ppm, the median is 3.5 ppm. In general, no relation to As, Pb nor another element is visible. Scandium and W generally exhibit low content, Sc and W are often falling below the detection limit (LOD Sc = 0.1 ppm; LOD W = 1 ppm; note that for the two samples 21TB01/-02 of the AUREX Biomining AG, the LOD is different). Scandium (median 0.74 ppm) and W (median 0.5 ppm) reach their maximum in samples less enriched in As or Pb. Sample 21TB09 has once again high contents of these elements (see Cr and Mn above), with Sc and W contents of 54 ppm and 227 ppm. Strontium does not show a clear pattern of correlation with the content of another element and is not related to neither As nor Pb. The median is 39.49 ppm, the maximum is 268 ppm in sample 21TB09.

Tin is below the LOD (1 ppm) in 12 of the 19 samples. The maximum Sn content is 3 ppm, with the median value being 0.5 ppm.

The content of Ti stays below 0.1 ppm, and two samples are below LOD (0.01 ppm). The maximum is 0.15 ppm in sample 21TB09, and the median is 0.05 ppm. Zn does not seem to show correlation to any other element, reaches a maximum content of 77 ppm, and has a median value of 7.5 ppm.

Table 6: Selected results of the whole rock geochemistry analysis. Samples 21TB01 to 02 and 21TB03 to 22JH34a have different detection limits and are analyzed in different laboratories. For further information see Chapter 3 and the appendix. The median value of the content is used to prevent strong influence by extrem outliers, for samples which do not reach the detection limit, half of the LOD was used.

	Ag	As	Au	Bi	Cd	Co	Cr	Cu	Fe	Ga	Ge	In	Mn	Mo	Ni	Pb	Rb	S	Sb	Sc	Se	Sr	Sn	Te	Ti	V	W	Zn
sample	ppm	ppm	ppm	ppm	ppm	ppm	ppm	ppm	%	ppm	ppm	ppm	ppm	ppm	ppm	ppm	ppm	%	ppm	ppm	ppm	ppm	ppm	ppm	ppm	ppm	ppm	ppm
21TB01	94	>10000	61.7	5.89	7.88	7.09	14.75	52.6	15.2	1.02	0.238	2.6	6620	1.44	45.8	50900	2.39	5.48	23700	1.62	5.51	66.9	0.09	0.184	0.001	8.7	0.08	77
21TB02	104	>10000	10.6	25.1	0.46	16.95	6.93	1155	19.15	0.95	0.113	3.5	116	1.57	16.75	24300	3.3	>10.0	3530	0.735	8.87	9.39	0.19	0.459	0.001	5.3	0.05	7.7
21TB03	10.1	>10000	4.09	0.8	<0.1	<0.1	<1	27.7	34.4	1.5	0.2	0.2	34	1	8	595	13.7	16.7	896	<0.1	9.3	4.1	<1	1.1	0.03	14	<1	4.1
21TB04	78.9	>10000	12	13.7	0.6	34.9	<1	466	21.4	3.4	0.3	0.2	43	2	29.3	>5000	34.7	12.2	1210	<0.1	<0.1	16.8	<1	0.6	0.04	24	<1	7.3
21TB05	4.17	>10000	8.13	0.2	<0.1	84.3	<1	6.2	23.4	0.9	0.2	0.2	39	2	55.6	138	10.6	11.6	672	<0.1	4.3	21.5	<1	0.5	0.02	11	<1	3.3
21TB06	4.19	>10000	8.18	0.2	<0.1	73.2	<1	6.9	21.1	2.8	0.3	0.2	83	2	51.7	202	24.4	10.8	562	<0.1	4.1	49.6	<1	0.4	0.05	31	<1	8.9
21TB07	0.21	1420	0.049	<0.1	0.1	5.7	73	4.4	2.38	14.9	0.1	<0.1	1060	2	22	78	78.3	0.02	8.7	<0.1	0.1	108	<1	<0.1	0.3	68	53	21.9
21TB08	5.75	>10000	14.1	0.3	0.2	67.3	<1	6.7	25.9	1.8	0.2	0.2	162	2	63.5	218	22.8	12.9	656	<0.1	4.8	77.9	<1	0.5	0.05	18	<1	14.7
21TB09	0.58	1710	0.146	0.3	0.3	36.8	504	4.2	9.82	13.4	0.1	0.2	5140	<1	256	158	28.3	0.04	14.2	54	0.2	268	2	<0.1	0.15	60	227	71.6
21TB10	3.48	>10000	6.16	0.3	<0.1	22.6	<1	8.4	21	1.9	0.2	0.2	64	2	43.6	584	18.7	10.2	493	2.3	4.1	63.9	<1	0.4	0.05	21	<1	7.7
22JH01	4.54	>10000	6.61	0.3	1.3	<0.1	<1	11.6	13.5	1.8	5.8	<0.1	70	3.1	98.3	167	23.5	12.7	454	<0.1	4.8	60.1	<1	0.8	0.05	21	<1	76.1
22JH02	0.3	82.3	0.01	0.1	0.2	19.9	138	105	2.23	2.1	<0.1	<0.1	738	2.9	56.3	20.4	8.3	1.32	0.8	2.1	3.7	111	<1	<0.1	0.07	51	<1	11.8
22JH07c	3.21	>10000	2.41	<0.1	<0.1	<0.1	<1	14	5.21	0.3	1.5	<0.1	42	2	21	127	0.9	3.45	214	<0.1	1.7	2.8	<1	0.6	<0.01	2	<1	2.4
22JH09c	16.8	>10000	10.4	0.9	<0.1	<0.1	477	18.5	13.5	4.5	5.2	<0.1	35	3.8	16.6	343	73.5	13.6	753	2	8.7	7.4	2	1.6	0.08	42	<1	3.2
22JH12	18.6	>10000	3.28	1.1	<0.1	7.3	<1	84.9	13.3	0.3	4	<0.1	25	2.1	4.8	1420	3.3	9.8	506	<0.1	5.1	4.1	<1	0.8	<0.01	4	<1	3
22JH14d	2.21	>10000	4.3	0.3	<0.1	12.3	<1	8.1	11.8	7.8	2.7	<0.1	91	2.5	71.3	46.1	79.3	7.01	415	2.6	3.3	27.4	2	0.6	0.09	52	<1	7.1
22JH29a	19.3	>10000	11.4	0.4	<0.1	12	<1	15	12.7	5.2	2.7	<0.1	207	2.2	44.1	67.3	49.6	5.52	388	2	3	106	1	0.5	0.1	41	<1	7.1
22JH32a	0.29	9810	0.107	0.1	<0.1	2.8	80	7.7	1.89	2.6	0.5	<0.1	154	1.1	8	262	28.7	0.75	37.8	2	0.3	14.1	<1	<0.1	0.06	25	<1	5.8
22JH34a	96.1	>10000	13.6	13.2	0.6	<0.1	<1	1440	15.2	7.9	3.2	0.3	160	2.4	16.9	>5000	51.3	5.29	659	7.3	6.9	39.4	3	0.7	0.08	91	<1	24.9
Median	4.54	10000	6.61	0.30	0.05	12.00	0.50	14.00	13.50	2.10	0.30	0.20	91.00	2.00	43.60	202.00	23.50	8.41	506.00	0.74	4.20	39.40	0.50	0.50	0.05	24.00	0.50	7.70

#### 4.2.2 Element correlations of the whole rock geochemistry results

To highlight potential complicated correlations, three elements each are compared per graph (Figure 9, Figure 10, Figure 11, Figure 12). However, to avoid having to normalize data to plot on a ternary we plot a normal x and y scatter plot, where the color of the data point shows the concentration of the third element. To indicate a possible trend of the data, the values of the x and y axis were used to construct a best fit trendline.

Silver/gold and As are compared to each other in Figure 9a. Silver and Au exhibit weak correlation, with the highest and lowest detected values of both elements roughly corresponding to each other, which is indicated by the trendline. Furthermore, increasing As content with an increasing amount of Ag or Au is indicated and often exceeds the upper detection limit of 10,000 ppm (Table 6). Lead plotted as a function of Ag and Au content, shows a slightly different trend, which can be seen in Figure 9b. It shows no correlation with Au. The four highest data points display peak values above the upper detection limit of 5,000 ppm Pb and are related to elevated Ag content, which reaches their highest content of a range from ~79 to 104 ppm. In the data of the AUREX Biomining AG this upper detection limit is higher and values of up to 50,900 ppm are reached. Compared with the correlation of Ag/Au in dependency of As, the difference is the general lower content of Pb. Still, Ag seems to follow a weak trend to increasing Pb content. Copper in comparison to Ag and Au shows a fluctuating behavior (Figure 9c). The increasing trend of Ag/Au is followed by a slight increase in Cu. Some values of Cu rise to 1,155 ppm, but most of the analyses are below 100 ppm. Compared with the Ag/Au comparison in Figure 9a and d, the Cu data has a tendency to follow the Pb values in a similar manner.

Silver/copper shows a general increasing trend, within some outliers of elevated Cu. Additionally, higher Ag/Cu contents correlate with higher Pb contents (Figure 9d). A similar, but weaker, trend is shown in Figure 9e, where the increase of Ag/Cu is followed by an increase in As. However, Table 6 indicates that the As content is generally high. The lowest content of As matches up with the lowest content of Ag and Cu. Figure 9f shows the correlation between Pb/Cu depending on As. It shows again that Pb and Cu are correlating, but are generally independent of As.

The quantities of Ge and Ga typically fall within a lower range, with Ge consistently exhibiting minor contents than Ga. As a general trend, Ge does not correlate with Ga (Figure 9g; h). The Ge content never surpasses 5.8 ppm, while Ga never exceeds 15 ppm. The content of neither Ge nor Ga shows a correlation to As (Figure 9g) or Pb (Figure 9h).

The comparison between Co/Ni content reveals a similar magnitude of elemental content. Generally, the content of Ni is higher than that of Co, which often is below the detection limit (Table 6). The resulting trend for both elements show a slight increase. The distribution of As in correlation with both elements fluctuates and does not follow a clear tendency (Figure 10a), but when compared to Pb, a slightly higher amount is observed with the increase of Co and/or Ni (Figure 10b). Figure 10c shows the comparison between Co and Ni as a function of Au. The content of Au varies and does not show any correlation between the elements.

Silver shows some correlation to Sb (Figure 10d; e; f). Compared to Cu (Figure 10d), As (Figure 10e) and Pb (Figure 10f) concentrations are elevated when Ag and Sb are elevated as well.

The Au vs Sb plot reveals a consistent upward trend (Figure 10g; h). The highest Au values correspond to elevated Sb values. Furthermore, with an increasing amount of both elements As also increases



(Figure 10g). Figure 10h indicates the correlation in dependence of Pb, which reveals an increasing content with the Au/Sb trendline.

The V vs. Mn plot (Figure 11a; b) does not exhibit a clear relationship between these elements either. Vanadium ranges from 2 ppm to 91 ppm, while Mn shows generally higher values, starting at 25 ppm, with several samples exceeding 1000 ppm and reaching a maximum of 6,620 ppm. The As (Figure 11a) and the Pb (Figure 11b) content seem to be unaffected by the content of Mn and V. These two elements seem to be unrelatable to any of the ore stages.

Chromium in relation to V fails to show a discernible trend either, as more than half of the Cr samples fall below detection limit. Though some samples reach a maximum Cr value of up to 504 ppm. In contrast to Cr, the content of V remains at a lower range as described above. A comparison to Mn (Figure 11c) reveals no correlation with Cr/V. In view of Cr/Ni and Co correlation in Figure 11d, no trend is discernible. Note that the content of Cr is generally often below LOD (Table 6).

Neither Se nor Te content is elevated in the samples of the whole rock geochemistry data (Table 6). There are no correlations with neither As nor Pb (Figure 11e; f).

The Ag vs. Zn graph illustrates an anticorrelation between both elements (Figure 11g; h). Correlating As (Figure 11g) with these two elements indicates that with lower Ag content As is depleted as well. Lead vs As (Figure 11h) shows no real trend, although the Pb content also higher with elevated Ag.

The correlation between Bi and Au is characterized by a continuous upward trend (Figure 12a). Although three data points for Bi fall below the detection limit, the majority exhibit a clear dependency on Au. Additionally, there is a generally high As content which shows a stronger correspondence to increasing Au compared to the increase of Bi. While the Pb (Figure 12b) content is less elevated than that of As, the same correlation (Bi vs. Au) shows an increase in the Pb content with the increase of both elements (Figure 12b).

The In/Cd relationship in the samples shows no clear overall trend (Figure 12c). The content is generally low, with almost half of the samples of both elements falling below the detection limit (LOD Cd=0.1 ppm; LOD In=0.1 ppm). The maxima do not surpass 7.88 ppm for Cd and 2.6 ppm for In. Copper content fluctuates and does not exhibit a consistent trend within the correlation of In vs. Cd. The Cd/Zn vs. Cu correlation shows no trend, with many analyses below the detection limit (Figure 12d).



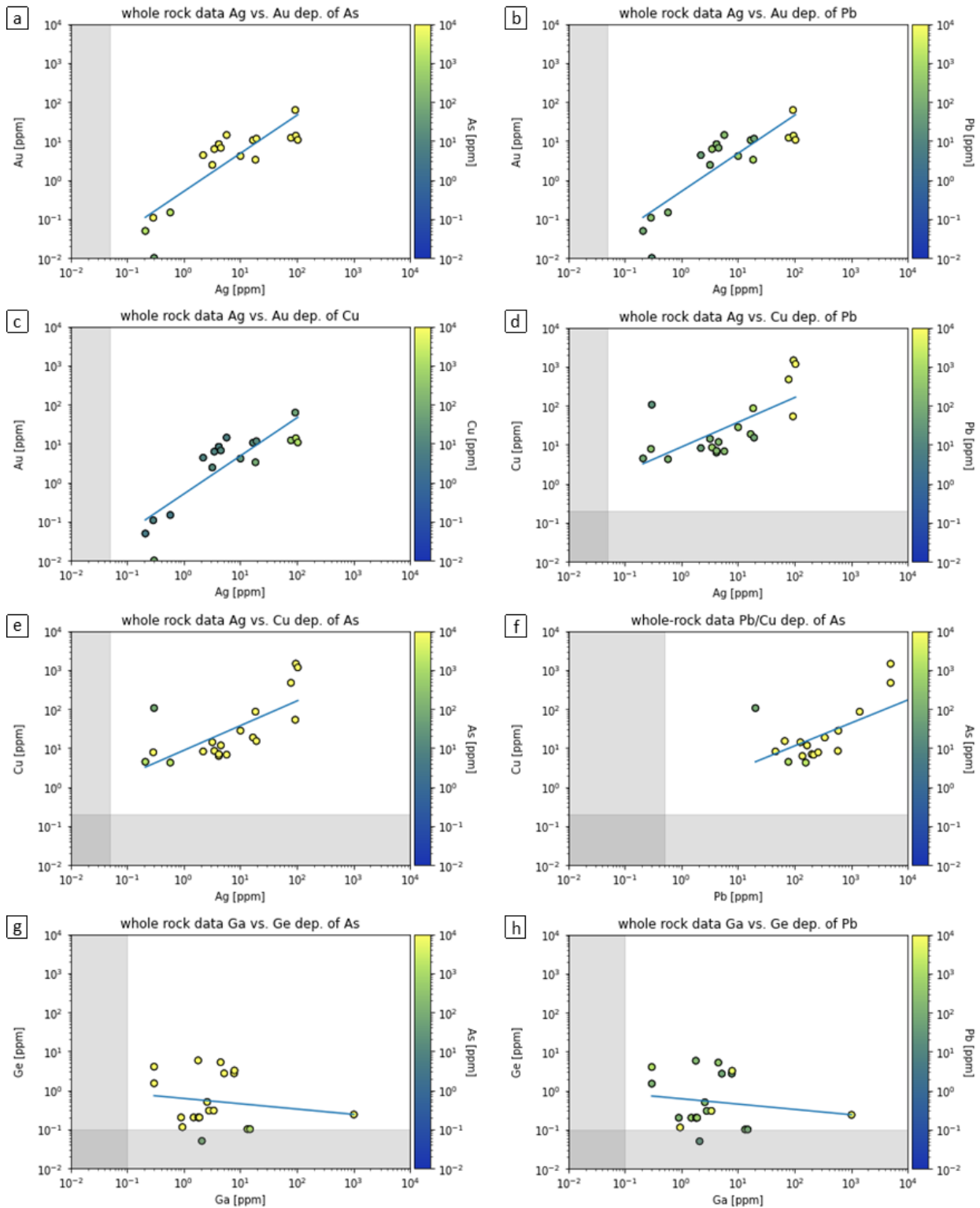


Figure 9: Whole rock geochemistry element correlation. Each graph shows three elements compared to each other. Two elements are on the axis, the third is depicted by the color bar. Measurements below LOD were taken as one half of the LOD. The LOD range (on elements of the axis) are marked within the grey fields. In each graph an attempt was made to model a best fit function. a) Ag vs. Au in dependence of As; b) Ag vs. Au in dependence of Pb; c) Ag vs. Au in dependence of Cu; d) Ag vs. Cu in dependence of Pb; e) Ag vs. Cu in dependence of As; f) Pb vs. Cu in dependence of As; g) Ge vs. Ga in dependence of As; h) Ge vs. Ga in dependence of Pb.

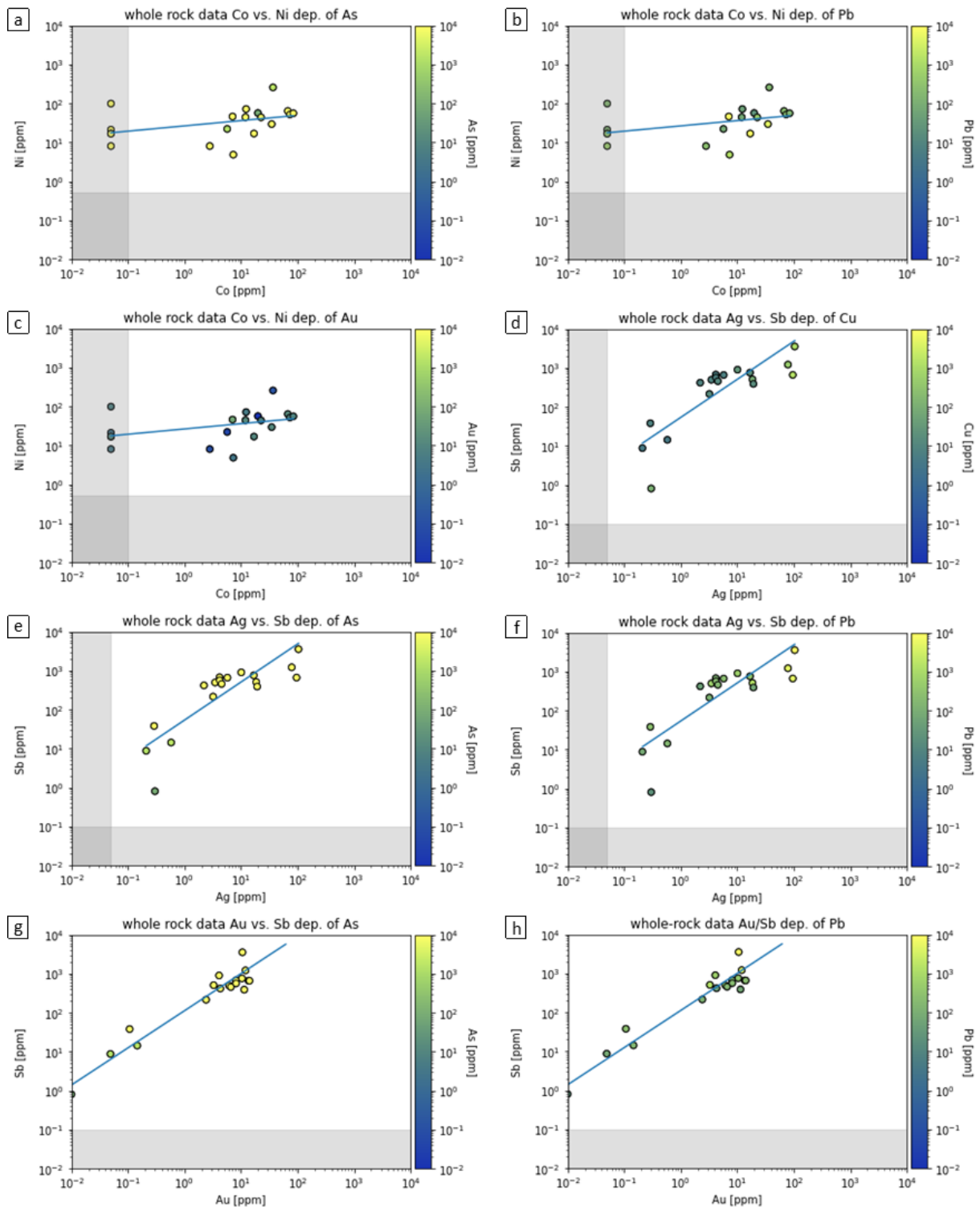


Figure 10: Whole rock geochemistry element correlation. Each graph shows three elements compared to each other. Two elements are on the axis, the third is depicted by the color bar. Measurements below LOD were taken as one half of the LOD. The LOD range (on elements of the axis) are marked within the grey fields. In each graph an attempt was made to model a best fit function. a) Co vs. Ni in dependence of As; b) Co vs. Ni in dependence of Pb; c) Co vs. Ni in dependence of Au; d) Ag vs. Sb in dependence of Cu; e) Ag vs. Sb in dependence of As; f) Ag vs. Sb in dependence of Pb; g) Au vs. Sb in dependence of As; h) Au vs. Sb in dependence of Pb.

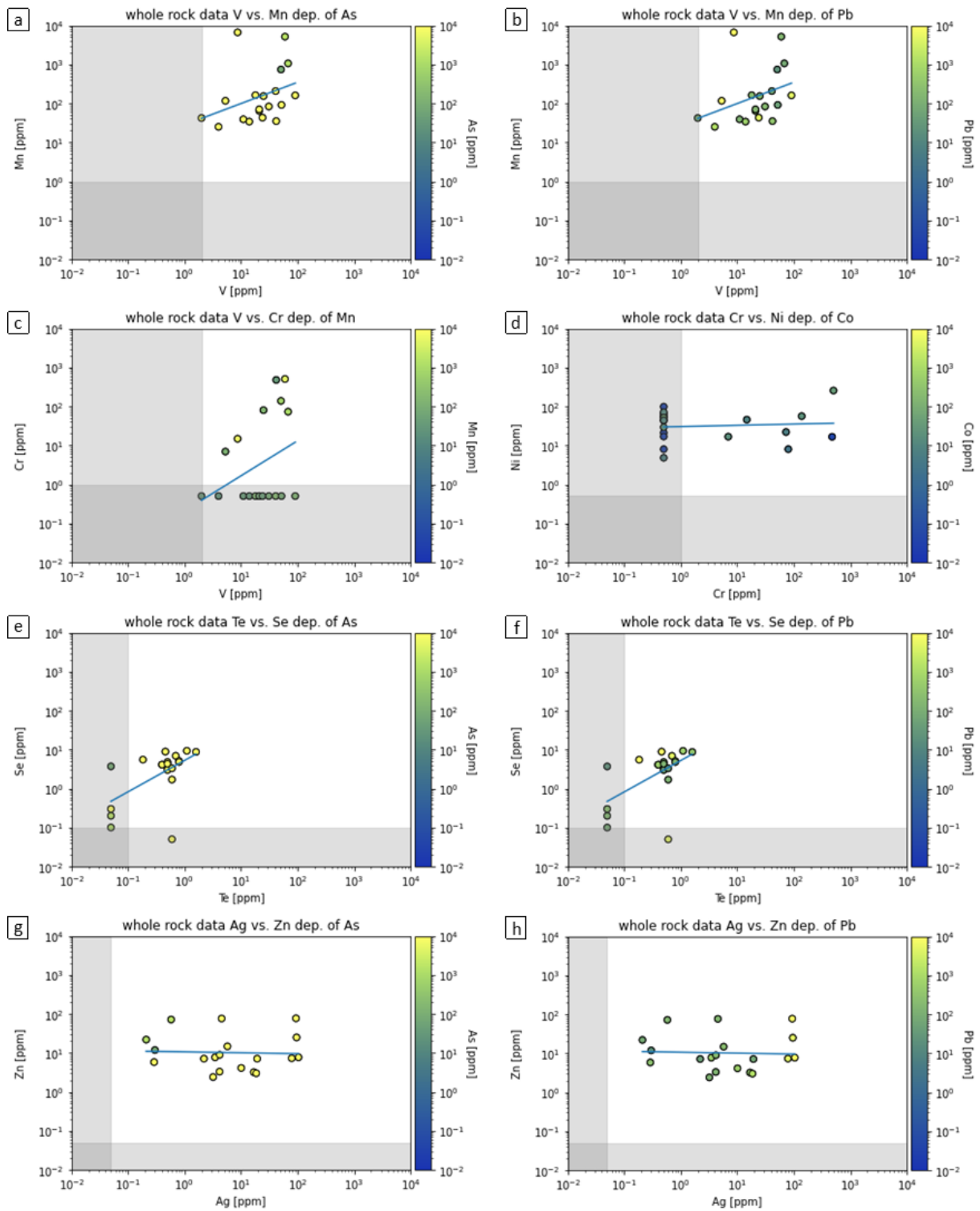


Figure 11: Whole rock geochemistry element correlation. Each graph shows three elements compared to each other. Two elements are on the axis, the third is depicted by the color bar. Measurements below LOD were taken as one half of the LOD. The LOD range (on elements of the axis) are marked within the grey fields. In each graph an attempt was made to model a best fit function. a) V vs. Mn in dependence of As; b) V vs. Mn in dependence of Pb; c) V vs. Cr in dependence of Mn; d) Cr vs. Ni in dependence of Co; e) Te vs. Se in dependence of As; f) Te vs. Se in dependence of Pb; g) Ag vs. Zn in dependence of As; h) Ag vs. Zn in dependence of Pb.

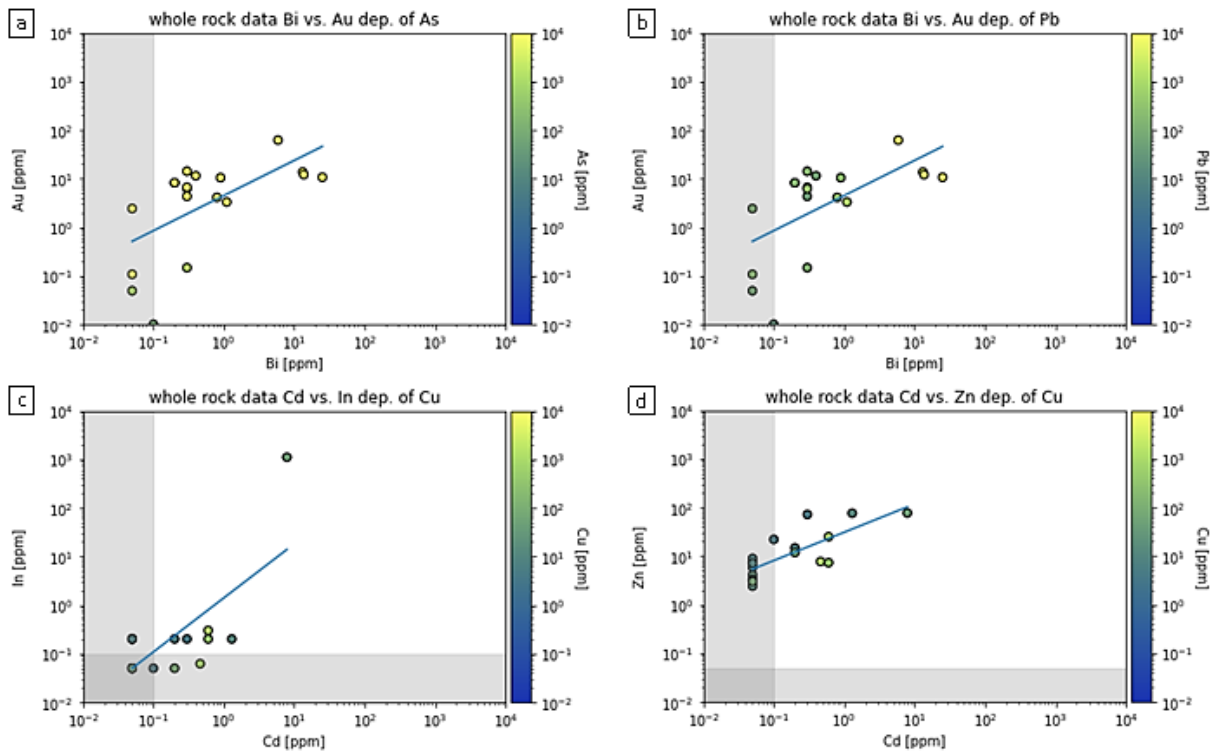


Figure 12: Whole rock geochemistry element correlation. Each graph shows three elements compared to each other. Two elements are on the axis, the third is depicted by the color bar. Measurements below LOD were taken as one half of the LOD. The LOD range (on elements of the axis) are marked within the grey fields. In each graph an attempt was made to model a best fit function. a) Bi vs. Au in dependence of As; b) Bi vs. Au in dependence of Pb; c) Cd vs. In in dependence of Cu; d) Cd vs. Zn in dependence of Cu.

### 4.3 Petrography

The samples collected during this study show features similar to those reported in previous work (Antes, 1998; Bojar *et al.*, 2001). The samples which have been collected (22JHXX; a letter suffix is added to distinguish between different hand specimens) have as mostly as dominant sulfide mineral arsenopyrite and pyrite. Several samples eg. 22JH07a, 22JH07b, 22JH08a show only one ore mineral, arsenopyrite. For example, 22JH07a indicates a massive ore veinlet mineralization, which only contains arsenopyrite.

The samples of the Paar-Collection (A0976-A0982) exhibit notably more sulfosalts and Pb-rich phases (Table 7). Galena is clearly distinguishable by the diagnostic triangular patterns caused by polishing and occurs in anhedral masses, partly overgrown by anhedral boulangerite. In general, there is no distinct boundary between these minerals in the optical microscope. Arsenopyrite and pyrite are often at the outer boundaries or accumulated in the middle of these masses.

Identified minerals include arsenopyrite, pyrite, chalcopyrite, galena, boulangerite and bournonite (Table 7). Pb-inclusions found in the samples exhibit a wide variation in their elemental composition. In most cases, the majority is dominated by Pb, Sb and S, with minor representation of Cu and Fe in these phases. In the samples, visible Au-Ag inclusions occur, but they are less abundant compared to the Pb-phase inclusions.

Table 7: Most abundant minerals in the different epoxide mounts; (XXX) high abundance of the mineral; (xx) moderate abundance; (x) low abundance.

	Arsenopyrite	Boulangerite	Bournonite	Chalcopyrite	Galena	Pyrite
22JH07a	xxx					
22JH07b	xxx					
22JH08a	xxx					
22JH09a	xxx	xx				xxx
22JH09b	xxx					
22JH10	xxx					x
22JH14a	xxx					
22JH14b	xxx				x	xxx
22JH14c	xxx					
22JH29b	xxx					
22JH31a	x			x	x	x
22JH34b	xxx					xxx
A0976	x				xxx	
A0977	x	xx				xxx
A0978	x	xxx				x
A0979	xxx					xxx
A0980	xxx				x	
A0981	xxx					
A0982	x	x	x		x	x

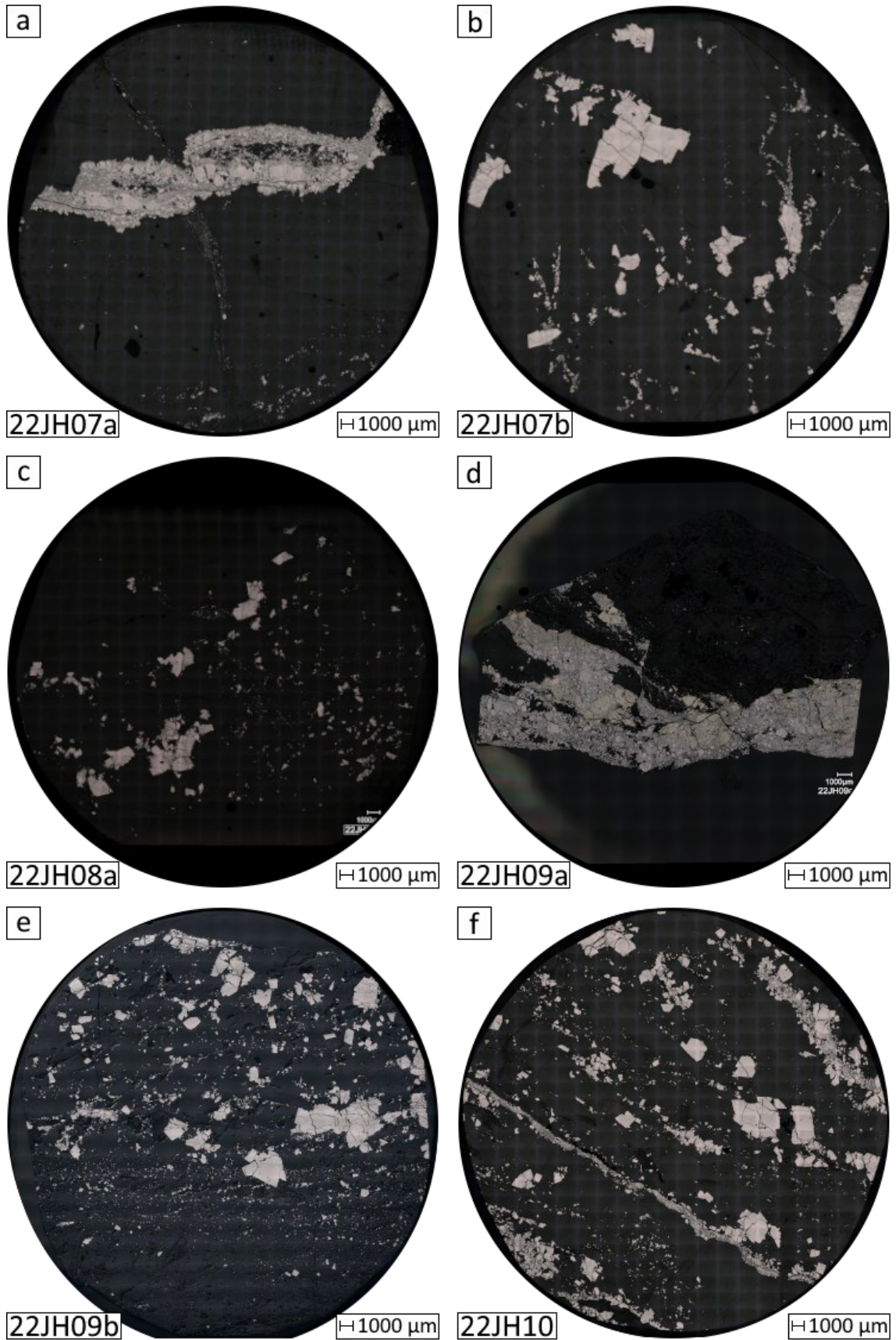


Figure 13: Overview pictures of the polished round mounts; a) Sample 22JH07a - major components massive arsenopyrite vein, with smaller vein, which consist of disseminated arsenopyrite cross-cutting it; b) sample 22JH07b - disseminated arsenopyrite; c) sample 22JH08a - disseminated arsenopyrite; d) sample 22JH09a major components are arsenopyrite, pyrite and boulangerite; e) sample 22JH09b - containing mostly disseminated arsenopyrite; f) sample 22JH10 - major component veins and disseminated arsenopyrite, minor occurs pyrite and electrum as well as Pb-inclusions.



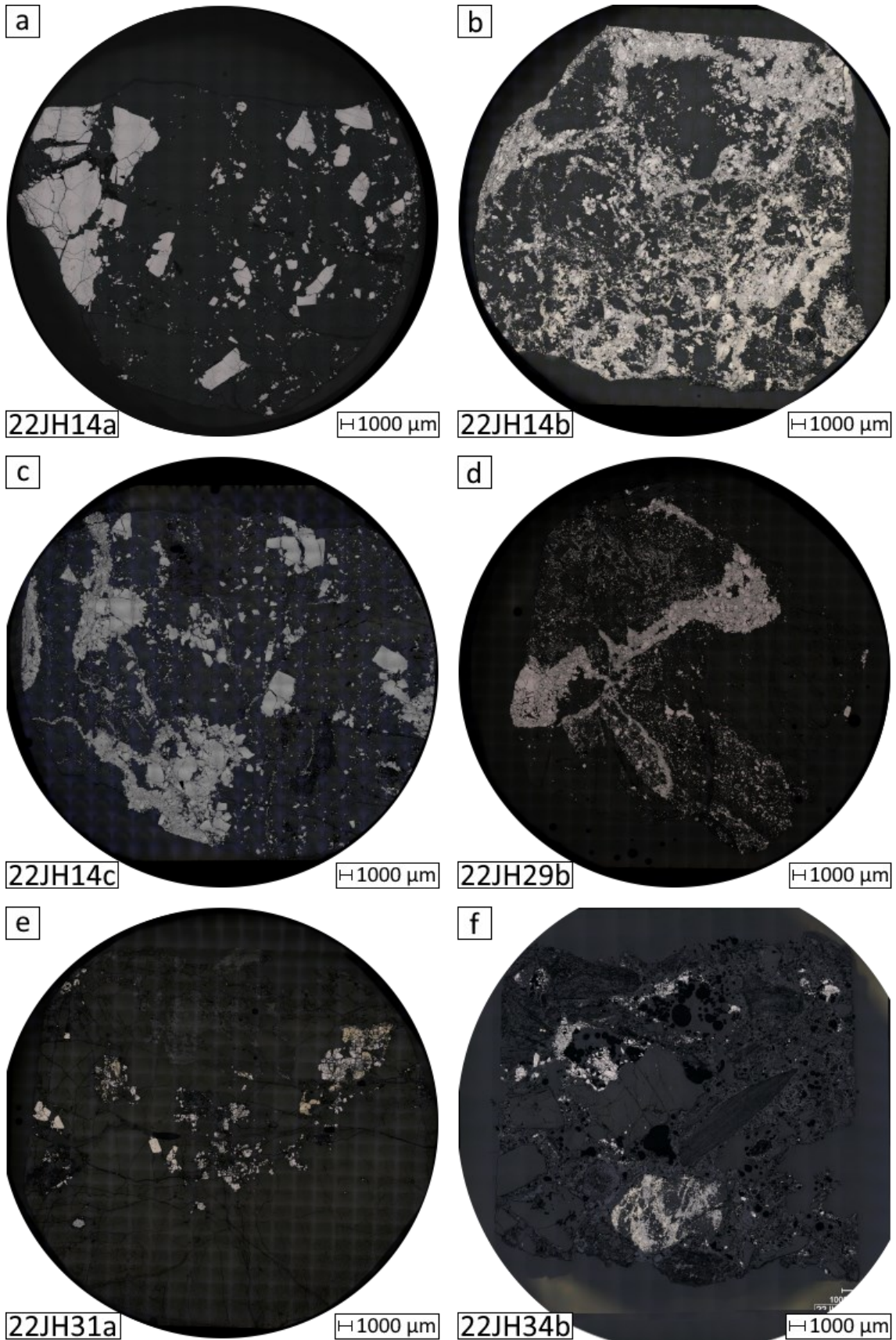


Figure 14: Overview pictures of the polished round mounts; a) Sample 22JH14a - major component is disseminated arsenopyrite; b) sample 22JH14b - arsenopyrite and pyrite are disseminated, galena occurs as minor component; c) sample 22JH014c - major component disseminated arsenopyrite; d) sample 22JH29a - veinlets of arsenopyrite, relatively abundant inclusions of especially electrum but as well Pb-phases; e) sample 22JH31a - consist mainly of arsenopyrite, chalcopyrite and pyrite, partly altered; f) sample 22JH34b - arsenopyrite and pyrite surrounded not just of quartz but as well of feldspars and mica.

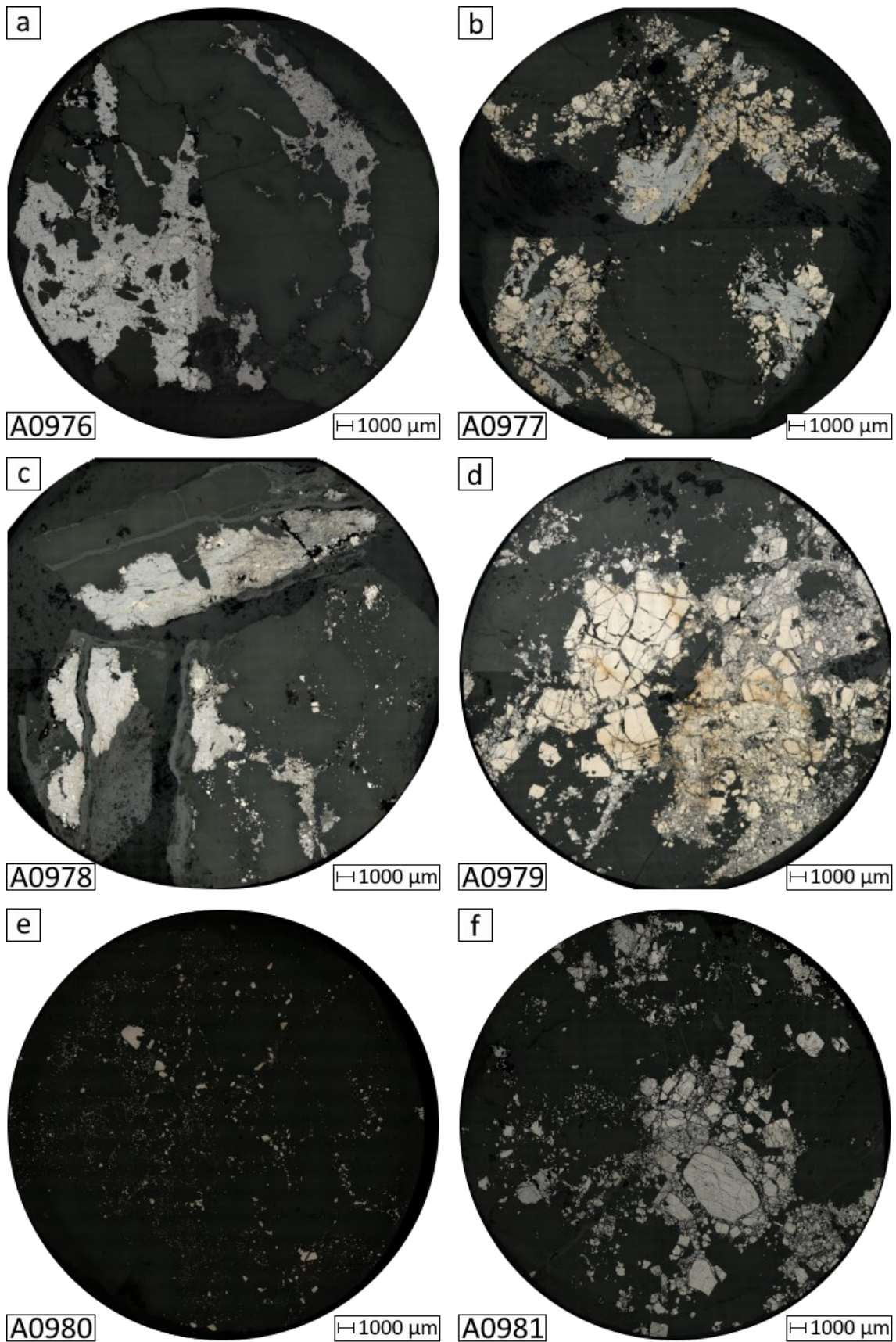


Figure 15: Overview pictures of the polished round mounts; a) sample A0976 - most abundant is galena, minor arsenopyrite; b) sample A0977 - pyrite together with boulangerite and minor arsenopyrite; c) sample A0978 - most abundant is boulangerite, minor arsenopyrite and pyrite; d) sample A0979 - arsenopyrite (mostly the smaller crystals) surrounding pyrite (bigger crystals) disseminated; e) sample A0980 - major component disseminated arsenopyrite; f) sample A0981 - most abundant are arsenopyrite and pyrite.



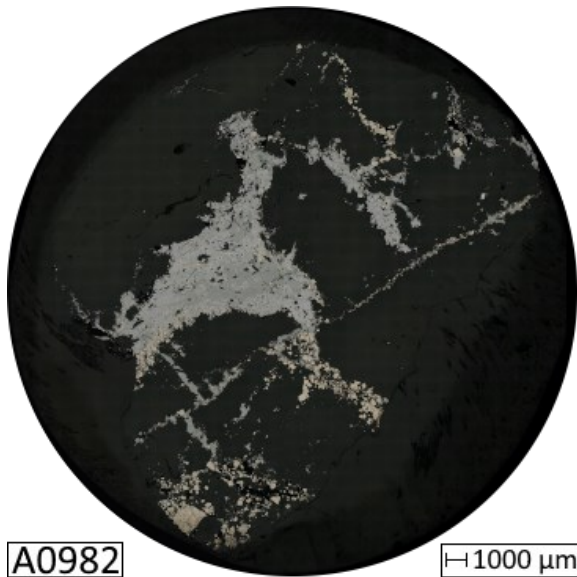


Figure 16: Overview picture sample A0982 - arsenopyrite, pyrite, bournonite, boulangerite and galena occur together as massive mineralization or in form of veinlets.

The combination of SEM/EDS was used to confirm the identity of mineral phases and detect heterogeneities/zonation's within the arsenopyrite and pyrite in the backscatter electron image (BSE). High contrast in the back scatter images made it possible to see zoning patterns in the arsenopyrite and pyrite, but the age of the backscatter detector meant that faint zoning was not always immediately visible. Further processing with an editing program (ImageJ; Schneider *et al.*, 2012) was necessary to increase the visibility. These images were used to determine zoning styles, and to select representative crystals from each zoning style to be further investigated with EPMA and LA-ICP-MS mapping.

#### 4.3.1 Petrographic descriptions of samples

##### *22JH07a*

Sample 22JH07a contains a massive arsenopyrite veinlet in the quartz with subhedral to euhedral crystals (Figure 13a). The massive arsenopyrite veinlet is crosscut by a smaller quartz veinlet with disseminated arsenopyrite. The crystals generally have a fractured appearance, while a minor component retains a euhedral to subhedral shape. The crystals, up to hundreds of micrometers separated from each other, are surrounded by small, rounded, and granular arsenopyrite, with the larger crystals showing undulating or brittle crystal boundaries. Noticeable are secondary veinlets that crosscut the massive arsenopyrite and alter it to an oxyhydroxide. The composition of these veins is As-Fe-O (Figure 17b) and often exhibited in other samples as well. Some of the arsenopyrite indicates several inclusions of sulfosalts (Figure 17a). The examination with the SEM shows that the composition is mostly of Pb-Sb-As-S and with minor Cu and Fe. Minor inclusions of electrum are also exhibited within the arsenopyrite in the sample.

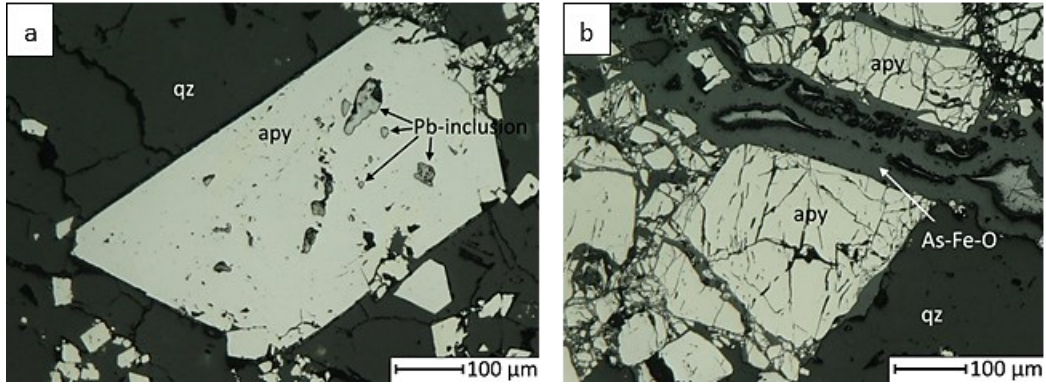


Figure 17: Microscopy pictures of sample 22JH07a; a) Arsenopyrite (apy) with Pb-Sb-As-(Cu)-(Fe) inclusions, gangue mineral is quartz (qz); b) Arsenopyrite (apy) is dissected by an As-Fe-O phase (arrow), gangue mineral is quartz (qz).

### 22JH07b

22JH07b (Figure 13b) shows abundant arsenopyrite like 22JH07a (Figure 13a) and 22JH08a (Figure 13c). In the quartz, the sulfide crystals are mostly subhedral and disseminated. The intensity of deformation is less, compared to sample 22JH07a. Nonetheless, it should be mentioned that these crystals are fractured, likely also along former quartz crystal boundaries. In this sample inclusions are less abundant and smaller than in 22JH07a. Around the arsenopyrite there often is an alteration halo containing As-Fe-O and in <0.5 wt% S. This alteration is often found on the boundary between the sulfide and the quartz distributed. Zonation is generally concentric (Figure 18a) and spotty. An arsenopyrite in this section was used for EPMA mapping (Figure 18a; see Chapter 4.4.2 EPMA element map 22JH07b).

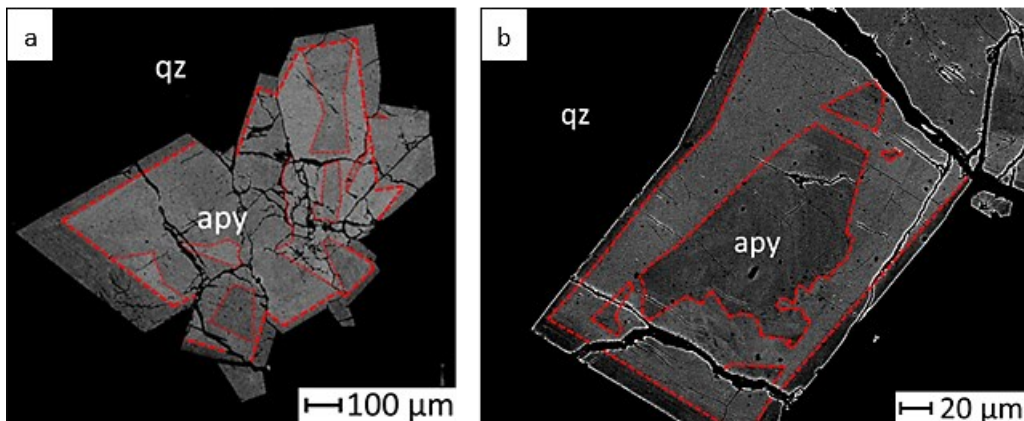


Figure 18: Zonation styles in sample 22JH07b and 22JH08; a) shows a concentric zoning in sample 22JH07b with a thickness size partly >100 µm. This crystal was also analyzed during the EPMA session (see Chapter 4.4.2 EPMA element map 22JH07b); b) Shows a Sb-bearing arsenopyrite concentric zoning in sample 22JH08a.

### 22JH08a

Sample 22JH08a (Figure 13c) has euhedral and subhedral arsenopyrite partly with minor, contents of Sb, detectable by EDS. The Sb content is between 0.36 to 0.50 wt%. Arsenopyrite crystals vary, like in for example sample 22JH07b in their size, the largest have a diameter up to 1000 µm. Smaller crystals occur often together with a size of few µm thick disseminated in the quartz vein. The arsenopyrite crystals are mostly fractured. Some of crystal boundaries or fractures contain As-Fe-O rich alteration

that nearly totally lack of any S (similar to sample 22JH07a; b). A few inclusions were spotted which are either Pb-As-Fe-S phases or a Pb-Sb-Cu-As-S phases, and are probably related as sulfosalts.

The arsenopyrites of the sample often shows a concentric zonation, which is several  $\mu\text{m}$  thick (Figure 18b). Generally, the brightness of the core varies from the rim in the BSE image. The larger crystals, which have a length above several hundred  $\mu\text{m}$ , indicate the same type of concentric zoning. One of them was further investigated with the EPMA session.

#### 22JH09a

The sample 22JH09a (Figure 13d) shows a partly 4,000  $\mu\text{m}$  thick ore veinlet in the quartz, dominated by three sulfides, in the order of highest content: pyrite, arsenopyrite and boulangerite. Most of the pyrite and arsenopyrite are fractured in several orientations and therefore partially rounded at the edges. However, some still show signs of idiomorphic growth. EDS shows that some arsenopyrite contains minor Sb (<1 wt%) (see appendix). Boulangerite acts as a gap-filling mineral. It is not present everywhere in the vein but has sometimes "dragged along" smaller pieces of arsenopyrite and pyrite (Figure 19c; d). With the help of the SEM it became apparent that smaller veinlets also intersect the three main minerals in a later phase (Figure 19a; b). This is again a Pb oxide phase, but without Sb and with approx. 5 wt% As. Arsenopyrite and pyrite often contain Pb-rich phases as inclusions.

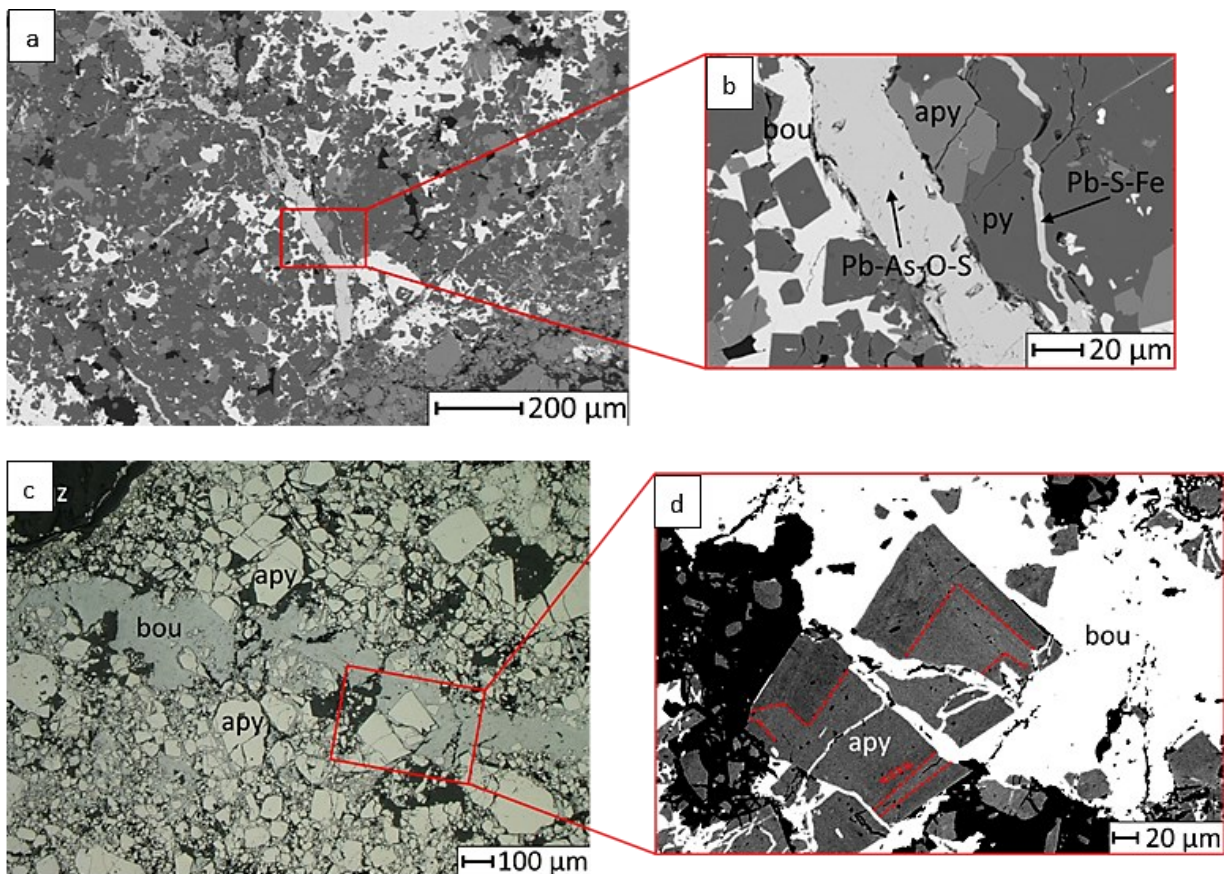


Figure 19: Sample 22JH09a; a) shows an BSE image of several veinlet generations in the sample; b) is an enlarged picture showing arsenopyrite (apy) and pyrite (py), which have been overgrowth by boulangerite (bou), cross-cut by different Pb-veinlets; c) microscopy photo of arsenopyrite (apy) crosscut by boulangerite (bou); d) shows the BSE image of a zoned and fractured arsenopyrite(apy) in boulangerite (bou).



### 22JH09b

22JH09b (Figure 13e) is from the same mine waste facility as 22JH09a (Figure 13d) but shows a clearly different petrography in the thin section. As with samples 22JH07a, -07b or -08a, arsenopyrite dominates the mineralogy in 22JH09b. Arsenopyrite is disseminated as euhedral to subhedral crystals, partly larger than 1000  $\mu\text{m}$ , showing several fractures. Smaller pyrites (Figure 20c) are also present, and can contain up to 0.94 wt% As. The large arsenopyrite crystals (> 2000  $\mu\text{m}$  diameter) often contain Pb-rich inclusions and show a rectangular zonation in the BSE image (Figure 20a; b). An oxide alteration, like in other samples, is not present in this sample. The gangue minerals in the vein are mostly quartz with minor feldspar.

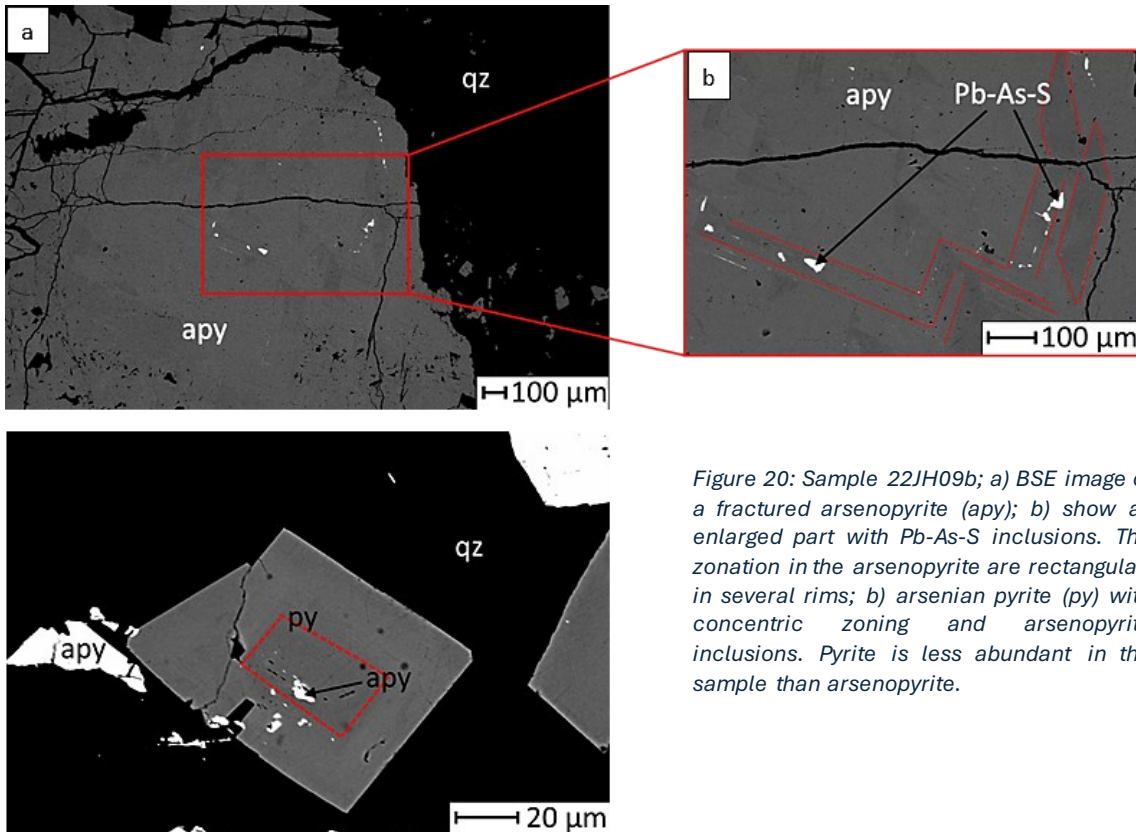


Figure 20: Sample 22JH09b; a) BSE image of a fractured arsenopyrite (apy); b) show an enlarged part with Pb-As-S inclusions. The zonation in the arsenopyrite are rectangular, in several rims; b) arsenian pyrite (py) with concentric zoning and arsenopyrite inclusions. Pyrite is less abundant in the sample than arsenopyrite.

### 22JH10

In sample 22JH10 (Figure 13f) the most abundant sulfide mineral is arsenopyrite, with minor arsenian pyrite. The sulfide minerals are mostly disseminated and show veinlet-like structures. The middle of the sample is crosscut by a feldspar vein containing fractured and randomly distributed crystals of arsenopyrites.

Table 8: Examples measurements of the zonation in arsenopyrite in Figure 21; a) 22JH10 20-21 refer to the dark zonation; 22JH10 22-23 to the brighter zone.

	wt% S	wt% Fe	wt% As	wt% Sb
22JH10 20	22.24	37.66	39.38	0.51
22JH10 21	22.3	39.06	38.02	0.44
22JH10 22	21.02	38.25	40.3	0.42
22JH10 23	21.65	38.38	39.3	0.46

Arsenopyrites often contain a low Sb content (~0.47 wt%) (Figure 21d). Figure 21a shows a single euhedral arsenopyrite with a triangle-shaped bright part on the left side of the crystal. The difference



in composition, as determined by EDS, is shown in Table 8. The values vary in each measurement, still the S content is clearly lower in the brighter parts.

The zonation of arsenopyrite occurs often oscillatory (Figure 21c). One of these arsenopyrites was used for EPMA element mapping (Figure 21c). Within this arsenopyrite there are inclusions of electrum and Pb-phases which also occur filling cracks. These inclusions can be also seen in arsenian pyrite of the sample (Figure 21a; b).

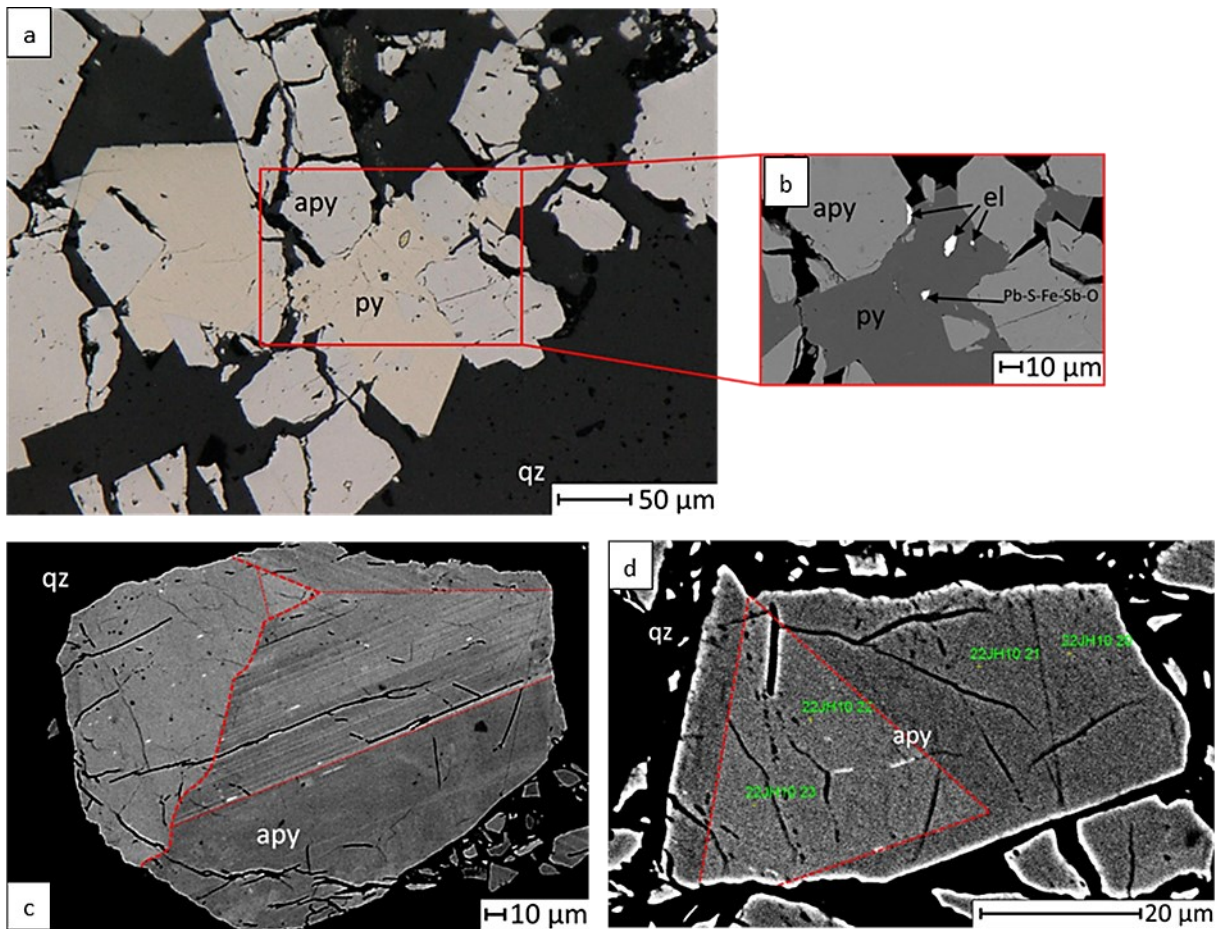


Figure 21: Sample 22Jh10; a) microscope photo of pyrite(py) overgrowing arsenopyrite (apy); b) BSE image of the pyrite which contains several inclusion of Pb-phases or electrum(el); c) BSE image of the arsenopyrite with oscillatory zoning. This crystal was used during EPMA mapping BSE; d) image of a triangle zonation in a arsenopyrite(apy); the brighter parts contain less S compared to the darker parts.

#### 22JH14a

Sample 22JH14a (Figure 14a) shows an arsenopyrite dominated sample with subhedral and disseminated crystals, the gangue mineral is quartz. There are numerous arsenopyrites larger than 1 mm in size. A few crystals are altered at the rim and show alteration products from As-Fe-O rich phases at their crystal boundaries. Zonation in the arsenopyrites is often spotty (Figure 22) or oscillatory. Inclusions in the arsenopyrite are Pb-rich sulfidic phases. These are often built into the zonation and appear as parallel stripes, in a similar fashion as might be expected from exsolution lamellae.

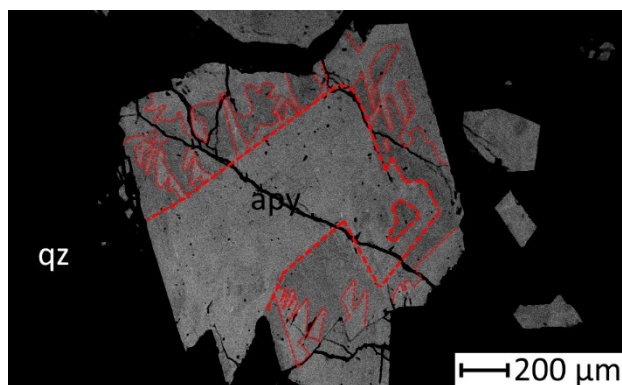


Figure 22: Sample 22JH14a; BSE image of a diffused and spotty zoned arsenopyrite (apy). The core seems totally unaffected by the zonation.

### 22JH14b

Sample 22JH14b (Figure 14b) contains abundant arsenopyrite and pyrite with fabrics of rounded, granular, and scattered crystals in quartz. Several crystals are euhedral, while anhedral are dominate. Both main sulfide minerals are dispersed and surrounded by each other. In other parts of the sample, there is a distinct segregation with the dominance of either arsenopyrites or pyrites. Galena is frequently present in the background and partly fills fractures. The textural pattern of arsenopyrites and pyrites indicates Pb-dominant inclusions, which have been identified by the SEM (Figure 23b).

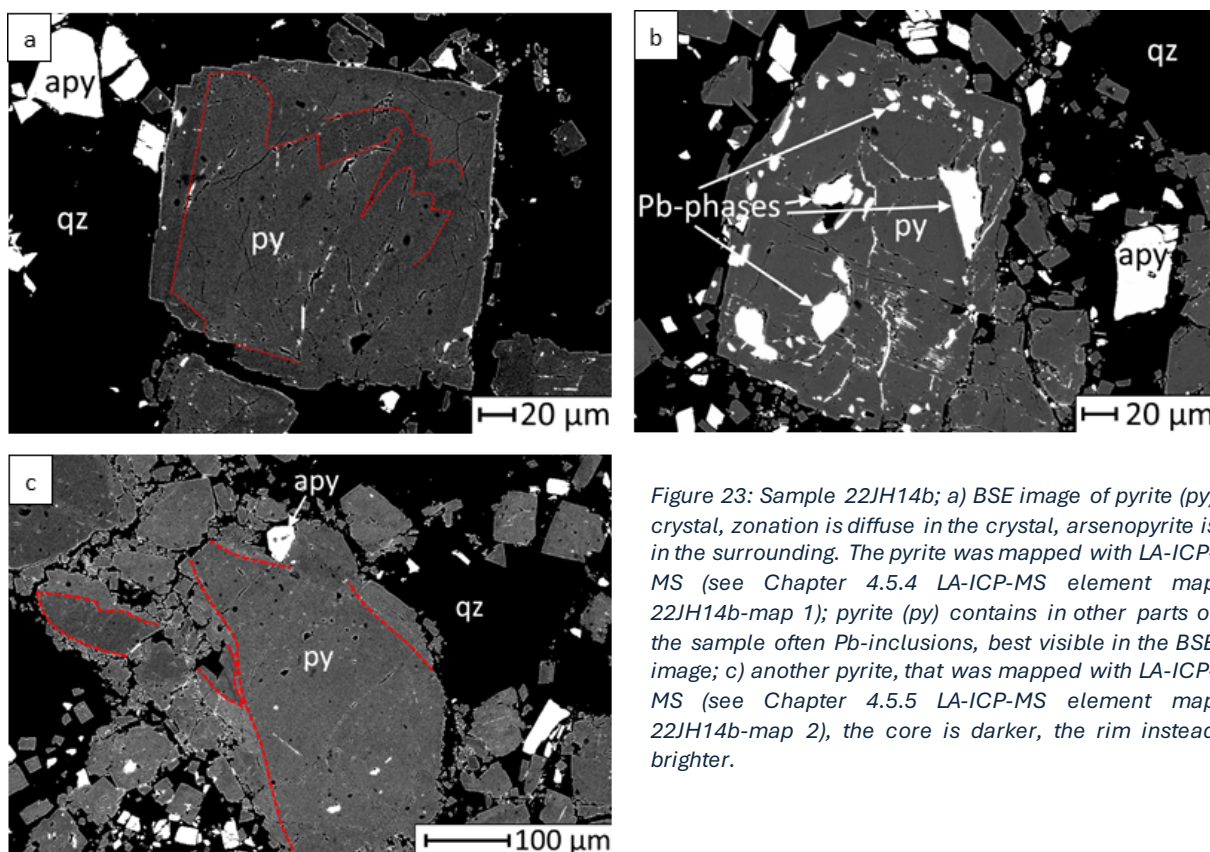


Figure 23: Sample 22JH14b; a) BSE image of pyrite (py) crystal, zonation is diffuse in the crystal, arsenopyrite is in the surrounding. The pyrite was mapped with LA-ICP-MS (see Chapter 4.5.4 LA-ICP-MS element map 22JH14b-map 1); pyrite (py) contains in other parts of the sample often Pb-inclusions, best visible in the BSE image; c) another pyrite, that was mapped with LA-ICP-MS (see Chapter 4.5.5 LA-ICP-MS element map 22JH14b-map 2), the core is darker, the rim instead brighter.

Pyrite and arsenopyrite in this sample were used for LA-ICP-MS and EPMA element mapping (see Chapters 4.4.3 EPMA element map 22JH14b-map 1; 4.4.4 EPMA element map 22JH14b-map 2; 4.5.4 LA-ICP-MS element map 22JH14b-map 1; 4.5.5 LA-ICP-MS element map 22JH14b-map 2). Zonation in



pyrite often has a visibly darker core and a brighter rim. In general, the zonation style varies between oscillatory and spotty (Figure 23a; c).

#### 22JH14c

Sample 22JH14c (Figure 14c) contains predominantly arsenopyrite in a quartz matrix, similar to the previous samples. The sulfide crystals are also generally disseminated, but in some places accumulate as massive mineralization. Beside this, small veinlets containing arsenopyrites (Figure 24a) crosscut the sample. Around 1 mm fractured crystals often occur in a rim of cataclastic arsenopyrite, often have rounded edges. Many arsenopyrite, mainly those larger than 0.5 mm, still show an idiomorphic shape, while the fraction of the smaller arsenopyrite is deformed. In this sample occurs electrum as well (Figure 24b).

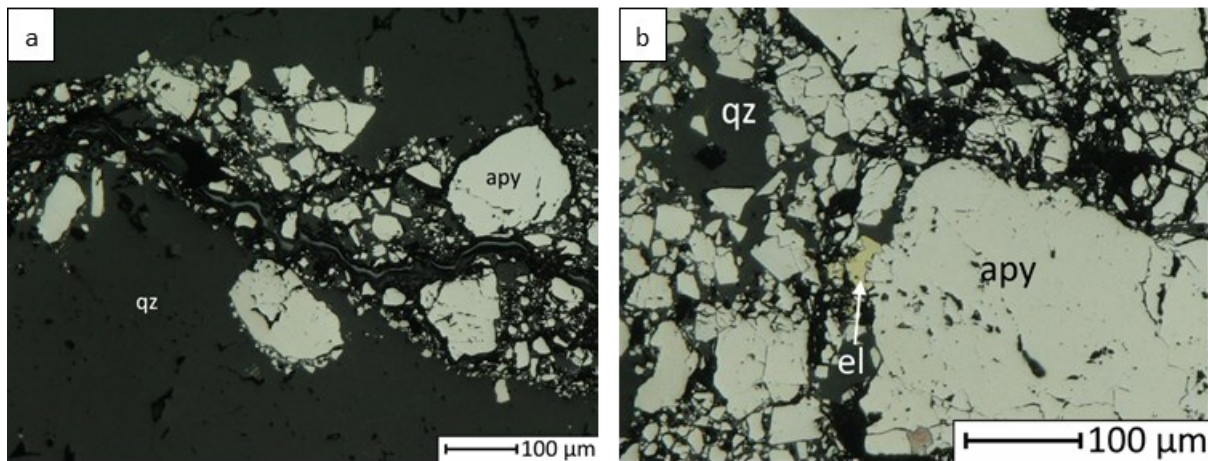


Figure 24: Sample 22JH14c; microscope photos of a) arsenopyrite (apy) veinlet and b) electrum (el) between disseminated arsenopyrite (apy).

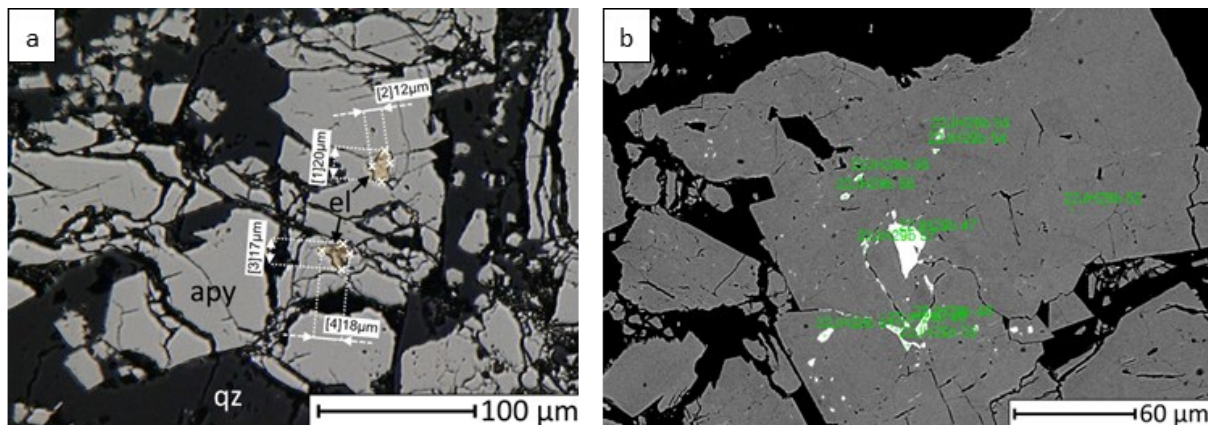


Figure 25: Sample 22JH29b; a) microscope photo of electrum (el) inclusions in arsenopyrite (apy); b) the BSE image shows the location of the inclusion in an arsenopyrite (apy), SEM results in Table 9.

#### 22JH29b

The main ore mineral in 22JH29b (Figure 14d) is arsenopyrite. Several different massive sulfide veinlets, some with a thickness of several millimeters, cut the main gangue mineral quartz in the sample. Many arsenopyrites are also disseminated within the quartz over large areas. The individual crystals are often subhedral, smaller ones are often crushed. This sample contains the greatest number of inclusions of electrum in arsenopyrite (Figure 25a; b). Table 9 shows an example of the composition of these, where Au in general is predominant. However, inclusions in arsenopyrite consist as well of Pb-rich phases.

Within the massive arsenopyrite veinlets, some smaller ones are visible in the backscatter images, which are mostly an As-Fe-O phase. These also often fill the fractures of the crystals. The zonation visible in the BSE image of the SEM is oscillatory or spotty.

Table 9: SEM results of the inclusions in an arsenopyrite in sample 22JH29b (location can be found in Figure 25).

	wt% S	wt% Fe	wt% As	wt% Ag	wt% Sb	wt% Au	wt% Pb
<b>22JH29b 47</b>		1.07	2.41	34.86		61.66	
<b>22JH29b 48</b>		1.38	2.83	41.68		54.11	
<b>22JH29b 49</b>		1.69	4.01	44.18		50.13	
<b>22JH29b 50</b>		3.65	5.98	35.99		54.38	
<b>22JH29b 51</b>	13.4	2.7	10.81				73.08
<b>22JH29b 52</b>	20.92	37.65	40.97		0.46		
<b>22JH29b 53</b>	13.69	5.51	13.6				67.2
<b>22JH29b 54</b>	17.92	31.66	32.5	1.52		16.39	
<b>22JH29b 55</b>	12.85	17.68	19.07	19.43		30.97	
<b>22JH29b 56</b>		2.82	4.88	29.68		61.74	

### 22JH31a

Sample 22JH31a (Figure 14e) is the only one that contains chalcopyrite (Figure 26a; b). It also contains abundant arsenopyrite, pyrite and galena. This sample is strongly affected by secondary fluids, that altered a larger portion of the ore minerals, while leaving others intact. A lot of the crystals that have fluid alteration features and appear anhedral (Figure 26a; b). In this sample the sulfides are disseminated and less abundant than in other samples. Figure 26c shows a subhedral pyrite crystal surrounded by a Pb-rich oxidic phase. Also, the fractures are filled with this Pb-oxide and some inclusion, both recognizable by a much higher reflectance in the BSE image, in contrast to pyrite. Inside the crystal, the zoning tends to be darker and lighter towards the rim. The boundary between the two zonings seems rather uneven and blotchy. It seems as if inclusion has no influence on it. This pyrite was mapped during the LA-ICP-MS session (see Chapter 4.5.1 LA-ICP-MS element map 22JH31a). Chalcopyrite was used for LA-ICP-MS spot analysis (see Chapter 4.6 Chalcopyrite in-situ spot analyses).

### 22JH34b

Sample 22JH34b (Figure 14f) shows a brecciated rock with different minerals in it. The gangue minerals are feldspars, quartz and micas as well as alteration products, that are not identifiable. Arsenopyrite occurs next to pyrite in small crystals, mostly smaller than 100 µm. Fractures and/or alteration on the crystals vary. A lot of pyrite crystals are euhedral and not fractured at all, while others are anhedral and intergrowing. Intergrowing mostly occurs at boundaries between pyrites and arsenopyrites. Alteration occurs at the rims of minerals. Pb-oxide phases are filling cracks.

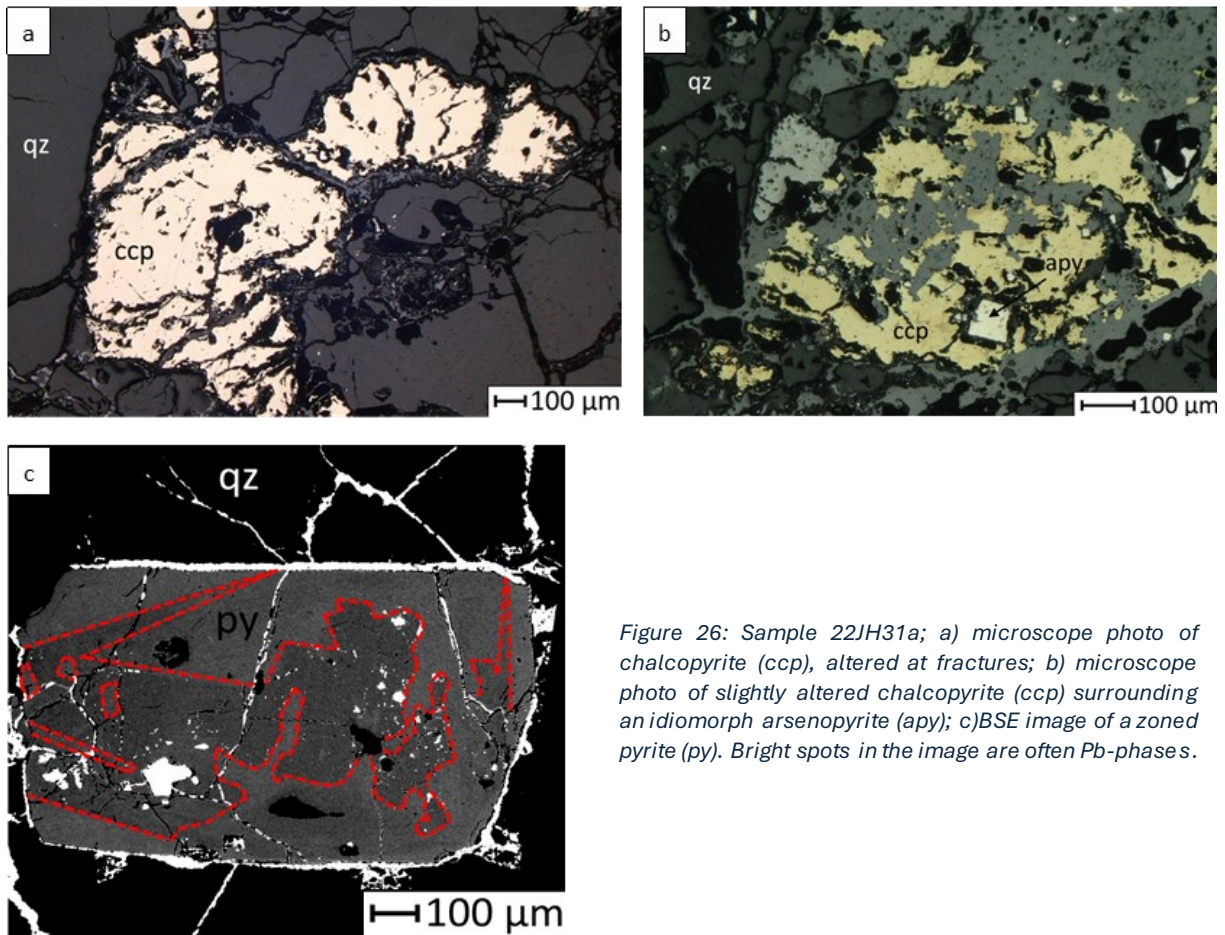


Figure 26: Sample 22JH31a; a) microscope photo of chalcopyrite (ccp), altered at fractures; b) microscope photo of slightly altered chalcopyrite (ccp) surrounding an idiomorph arsenopyrite (apy); c) BSE image of a zoned pyrite (py). Bright spots in the image are often Pb-phases.

#### A0976

Sample A0976 (Figure 15a) contains abundant arsenopyrite within galena masses in the gangue mineral quartz. Secondary phases seem to be more severely affected by oxidic phases arsenopyrite compared to the galena. Alteration is visible on cracks of the anhedral arsenopyrite. Galena often occurs as a fracture filler between quartz crystal boundaries (Figure 27b).

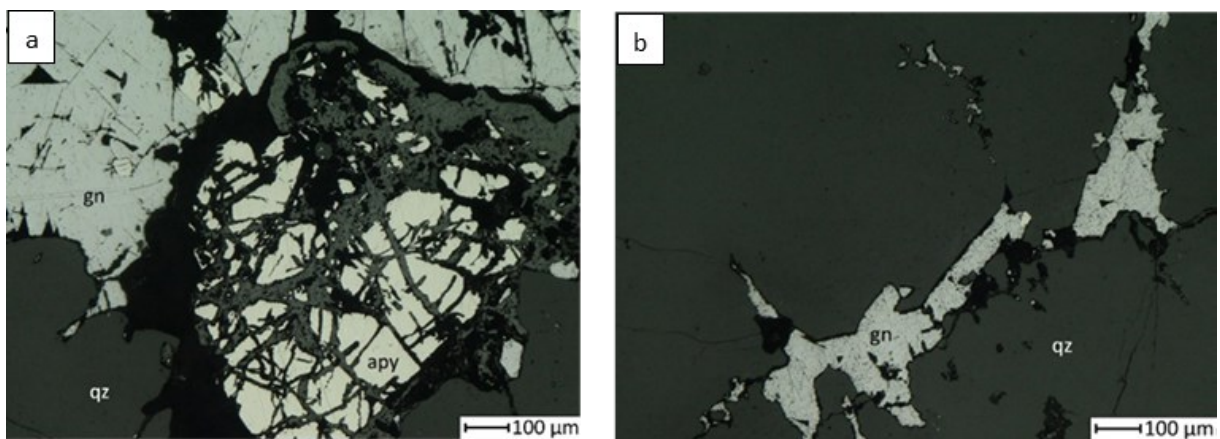


Figure 27: Sample A0976; a) fractured arsenopyrite (apy) in the vicinity of galena (gn). The arsenopyrite is more affected by alterations; b) shows galena (gn) as fracture filling element in the gangue mineral quartz (qz).



### A0977

The main sulfide minerals in sample A0977 (Figure 15b) are pyrite and boulangerite. Euhedral, but altered, pyrites occur in massive accumulations and veinlets. The alteration is often exhibited as As-Fe-Sb-O phases at the boundaries of the pyrite or in fractures of the gangue mineral quartz. Within the fractures of the pyrite, boulangerite has re-crystallized and often healed the fractures, so that it can also be found as inclusions within the crystals. In other places, boulangerite occurs as massive mineralization, within which inclusions of <10  $\mu\text{m}$  large euhedral arsenopyrite are often trapped. These rarely appear to have been fluid altered.

### A0978

Sample A0978 (Figure 15c) is characterized by massive boulangerite mineralization, with veinlets several millimeters thick. It is noticeable that (sub-) euhedral pyrite of a size of up to several hundred  $\mu\text{m}$  are within the boulangerite mineralization. Some of these are also fractured and healed with the Sb-Pb phase and some inclusions are also visible. Together with the mostly much smaller (sub-) euhedral arsenopyrite, which reach a maximum size of a few tens of  $\mu\text{m}$ , pyrite and arsenopyrite appear as "veins" within the boulangerite mineralization. However, pyrite and arsenopyrite can also be found at the edge of the Pb-Sb phase. In these cases, they are often right at the boundary to the quartz. Much less common in the sample are disseminated arsenopyrite and pyrite. These occur often in a paragenetic relationship with arsenopyrite intergrown into pyrite.

### A0979

A0979 (Figure 15d) contains predominantly arsenopyrite and pyrite, which occur disseminated, as veins or as massive mineralization. The pyrite mostly consists of millimeter-sized subhedral crystals, some of which are fractured. They are often surrounded by a rim of crushed arsenopyrite, but there are also some larger crystals of the mineral. The arsenopyrites are more often broken. The fractures often contain alteration products, which consist of As-Fe-O phases (Figure 28a). The edges of the minerals are often rounded. However, the fractures are often healed with a Pb-(Sb)-rich oxide phases (Figure 28a). In this phase, the Pb content predominates. The zonation of pyrite is mostly spotty without any geometric figures. Fractures in quartz are often healed with Pb-oxide phase (Figure 28b).

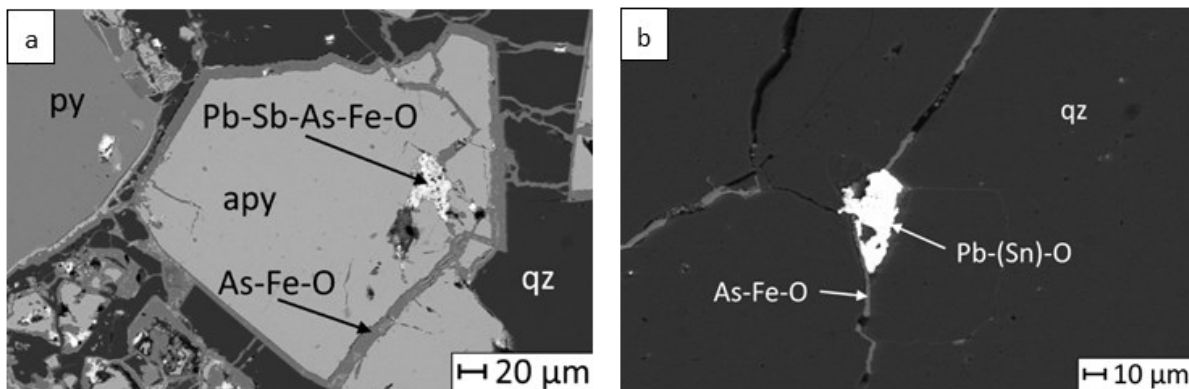


Figure 28: Sample A0979; a) BSE image of pyrite (py) and arsenopyrite (apy) in quartz (qz). Arsenopyrite is altered on the edges of the crystal, inclusions are enriched mainly in Pb and Sb; b) BSE image of fracture in quartz (qz); in the junction is Pb-oxide enriched, As-Fe-O is filling the fractures.

### A0980

Arsenopyrite is the dominant sulfide mineral in A0980 (Figure 15e) which occurs as massive mineralization in the gangue mineral quartz. In some places there is galena, but this only plays a less important role. The once larger arsenopyrite has undergone multiple fragmentation and alteration by



secondary fluids, which leaves an As-Fe-O (Figure 29a) alteration product. This alteration is widespread in the fractures in this polished mount. Antimony free Pb oxide phases have accumulated within these alteration zones (Figure 29c). Electrum inclusions can also be found in the sample (Figure 29b).

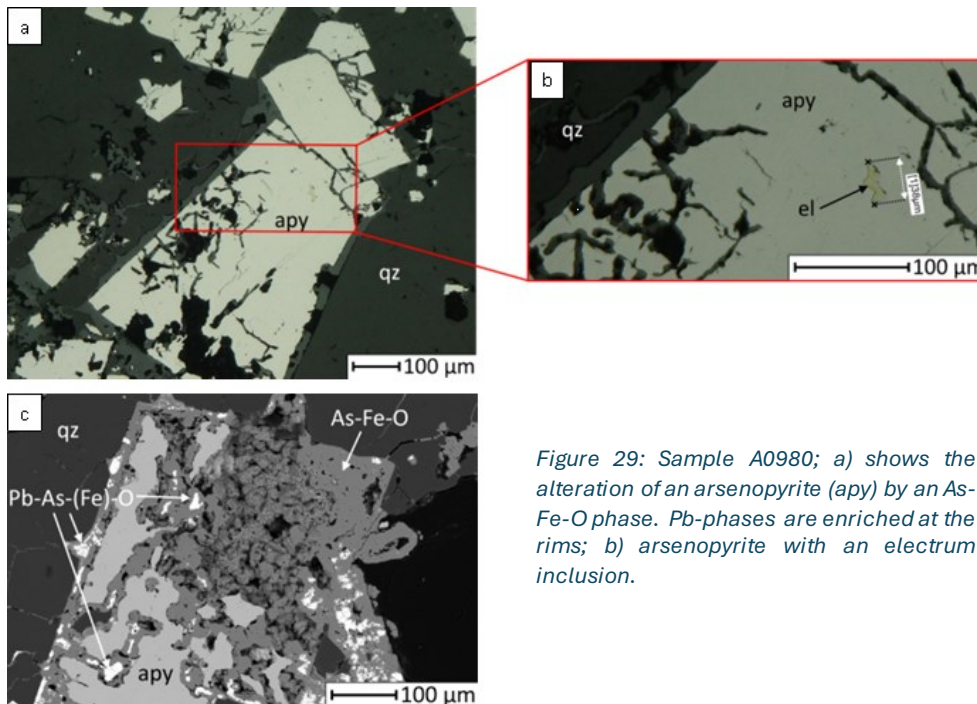


Figure 29: Sample A0980; a) shows the alteration of an arsenopyrite (apy) by an As-Fe-O phase. Pb-phases are enriched at the rims; b) arsenopyrite with an electrum inclusion.

### A0981

Sample A0981 (Figure 15f) contains many disseminated arsenopyrite crystals and often not more than a few µm in size. Some larger subhedral crystals are also present in the section and some of them have altered boundaries. There is some small pyrite disseminated as well.

### A0982

A0982 shows the most variety of ore minerals. Besides arsenopyrite and pyrite, the variety of Pb sulfide-phases is the greatest (Figure 16). Galena, boulangerite and bournonite occur in anhedral masses surrounding arsenopyrite and pyrite. Partly the Pb-phases occur as crack filling or as inclusions in quartz, arsenopyrite and pyrite. Figure 30 shows bournonite overgrown by boulangerite and galena.

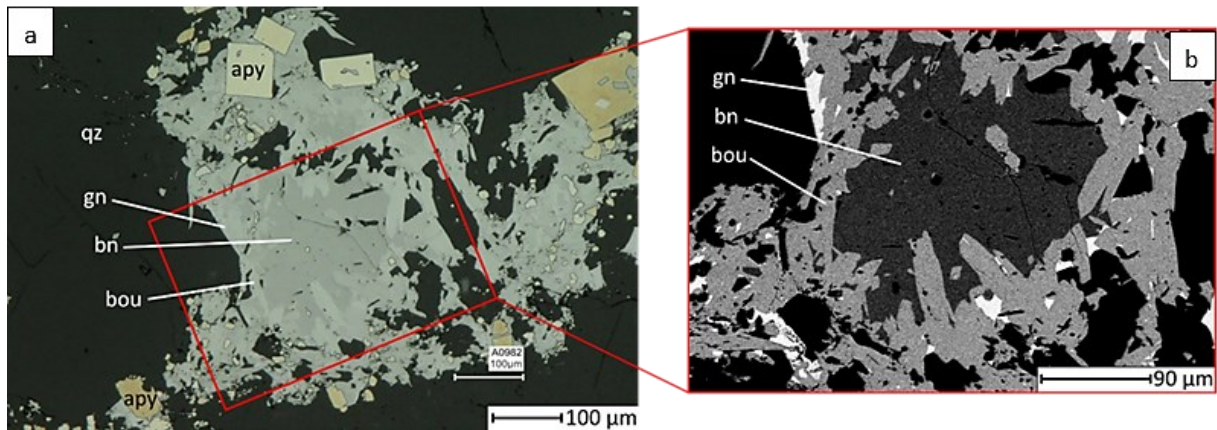


Figure 30: Sample A0982; a) microscopic photo of bournonite (bn), boulangerite (bou) and galena (gn) overgrowing arsenopyrite (apy); b) shows an insight of the minerals in the backscatter image.

EDS measurement points (Table 10), show the element distribution. The trend goes from galena as Pb-rich sulfide to boulangerite, which contains Pb and Sb to bournonite, which contains Cu. In most cases is boulangerite intermediate position (Figure 30a; b), even when it is the smallest phase.

Table 10: Example of gradually element distribution in mass% in sample A0982. From measurement A0982 48 to A0982 50 the element distribution of Cu and Sb increases, while the Pb content decreases.

	wt% S	wt% Cu	wt% Sb	wt% Pb
<b>A0982 48</b>	11.92			88.08
<b>A0982 49</b>	18.35		30	51.65
<b>A0982 50</b>	20.21	14.04	27.03	38.72

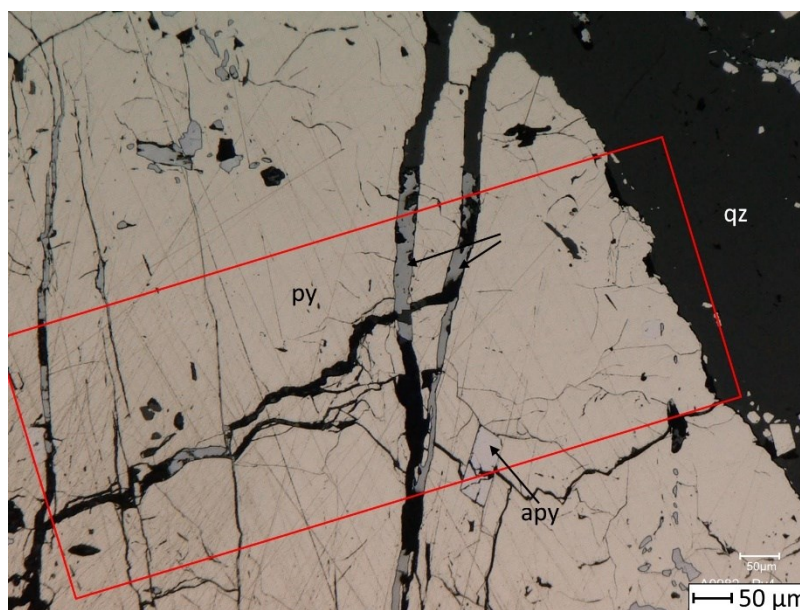


Figure 31: Sample A0982; microscope picture of an fractured pyrite (py). The filling in the fracture consist of an Ag-Pb-phase. The pyrite includes as well arsenopyrite (apy). This pyrite was partly mapped during the LA-ICP-MS mapping sessions (red box) (see Chapter 4.5.3).

## 4.4 EPMA maps element maps of arsenopyrite

In total, five element maps of arsenopyrite have been created with the EPMA from four different samples. In the case of multiple maps of/for the same sample the maps are individually labeled.

The maps show either parts of arsenopyrite or the whole crystal, depending on the size of the respective mineral. The EPMA maps provide only qualitative and not quantitative results. Still, higher element contents are indicated by brighter colors on the color scale, while darker shades indicate lower element content.

In general, for all maps the elements Ag (EDS), As (WDS), Au (WDS), Co (EDS), Cu (EDS), Fe (EDS), Ni (WDS), Pb (EDS), S(EDS) and Sb (WDS) are shown. Other maps, like As (EDS) can be found in the appendix.

### 4.4.1 EPMA element map 22JH08a

The BSE image of the map (22JH08a - Figure 32a) indicates a clear zonation in the arsenopyrite crystal. The brighter core of the crystal is surrounded by darker rim with a thickness of up to 100  $\mu\text{m}$ , which varies partly in the BSE brightness. Within the core, multiple stripes are apparent, exhibiting diverse orientations and a varying thickness. Some of these zonations are diffuse and chaotic, particularly the top left part, which appears unclear. A distinct feature is a triangular shape within the core of the crystal. On the right side of the map, the edge displays a gradual zonation, with a lighter upper section and a darker lower section. The darkest portion of the entire crystal is found at the bottom of the rim. Several different fractures can be located within the crystal, with no linkage to the zonation of the arsenopyrite visible in the BSE image.

The zonation of As (Figure 32c) in the crystal is highly visible and generally follows the zoning in BSE image. The brighter zones in the BSE image are congruent with those with a higher As content. One exception is the darker rim at the bottom of the BSE image which is not visible in the map of the As. Gradually increasing As concentrations are displayed in the right rim and in the right part of the inner core as well. The dominant triangular shape within the core is clearly visible.

Gold (Figure 32d) and Pb (Figure 32i) show similar zoning patterns in the EPMA map. The triangular shape in the middle of the crystal, which can be already seen in the BSE image, is distinguished by elevated Au and Pb contents. A smaller triangular shape at the upper-left corner of the Pb map shows a higher content, which mirrors the features seen in both the BSE image and the As map. The zonation looks much like the one vivid in the BSE image and As map, however, the details are less visible in the Au and the Pb map. Sulfur (Figure 32j) exhibits a zonation pattern contrary to that of As, Au and Pb. The map of S shows clearly that the content is higher where the content of As, Au or Pb is low.

The map of Sb (Figure 32k) depicts a distinct and sharp zonation with several details, which surpasses the zonation of the BSE image. These zonation features are not visible in the other element maps, but still show some comparable characteristics. The triangular shape which partly corresponds to that of As, Au, Pb and S is exhibited. The right side of the Sb map, in contrast, diverges from that of As, Au, Pb and S. The rim on the right side remains visible, while on the top the zonation looks like a fan and has stripes with less Sb content in it.



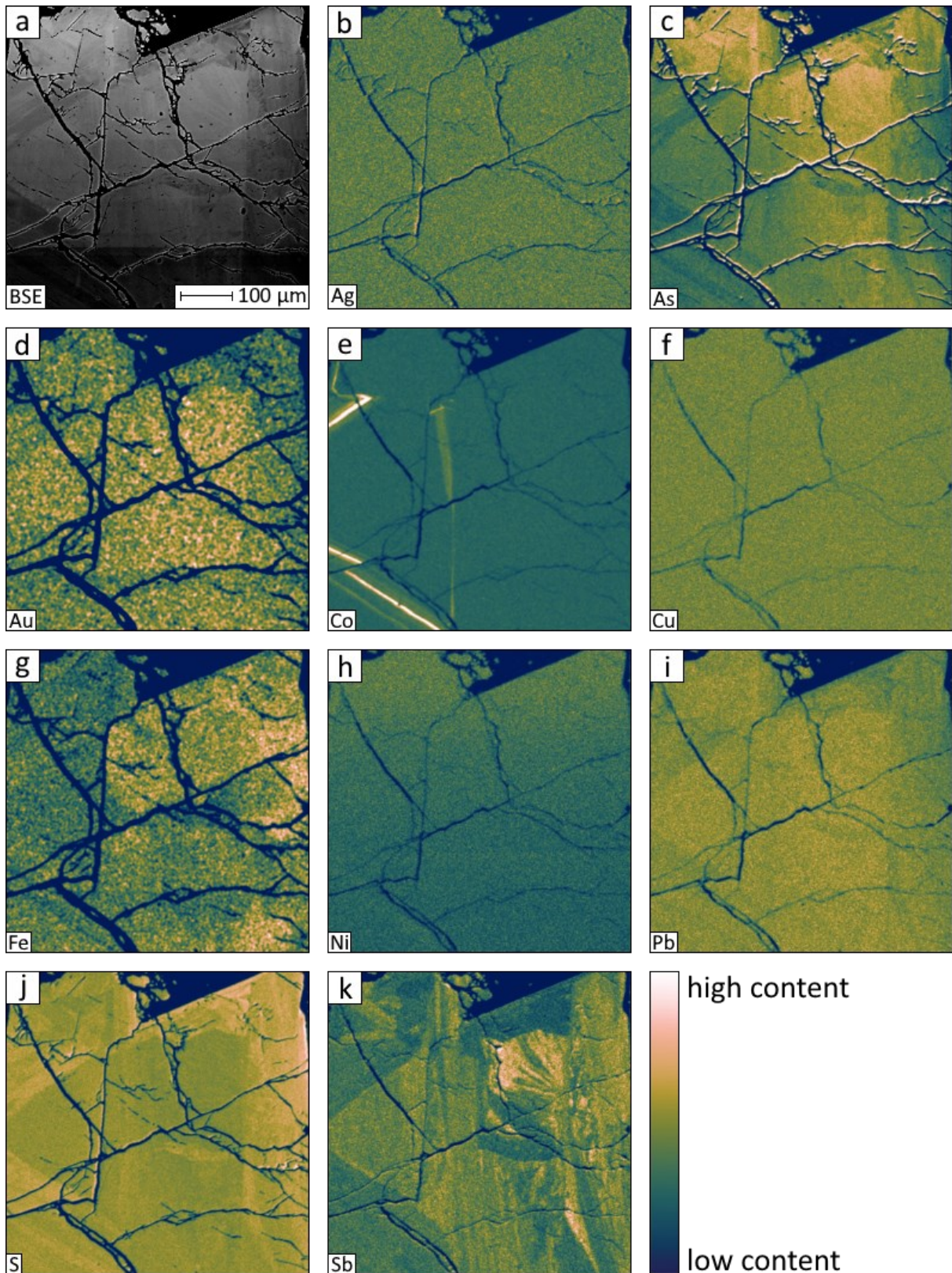


Figure 32: Arsenopyrite element maps in sample 22JH08a; a) BSE image; b) Ag EDS spectrometer; c) As WDS spectrometer; d) Au WDS spectrometer; e) Co EDS spectrometer; f) Cu EDS spectrometer; g) Fe EDS spectrometer; h) Ni WDS spectrometer; i) Pb EDS spectrometer; j) S EDS spectrometer; k) Sb WDS spectrometer.

This part can be seen as well in the As map, as part with a higher element distribution but with less details.

The Co map (Figure 32e) reveals a triangular shape, showcasing a significant contrast in Co content. Nickel (Figure 32h) exhibits a gradual change from a higher to a lower content from the bottom to the top of the image, which doesn't correspond to any of the other maps. It is likely due to beam drift over the course of the analysis. Copper (Figure 32f), Ag (Figure 32b) and Fe (Figure 32g) do not show any zonation at all.

#### 4.4.2 EPMA element map 22JH07b

The location of this map was selected due to the clear rim zonation that was evident in the in the BSE image (Figure 33a). Several intergrown crystals are apparent in the map and are all fractured to different degrees. The sizes of the crystals vary, and the map has a total diameter above 700  $\mu\text{m}$ . The largest crystal on the left side of the image distinctly displays darker rims on each side. Notably, there is a clear variation in thickness among the rim, each featuring a sharp boundary with the core of the crystal. The crystals on the bottom and right side also exhibit core-rim structures, although they are less dominant or in some cases non-existent.

The bottom crystal shows a significantly darker, partly rectangular, core surrounded by a brighter zone. The left core displays a diffuse zonation. The features include sporadic sections of brightness or darkness, with some exhibiting a sharper contrast compared to others. The smaller and fractured parts of the accumulated crystals in the left part of the image show diffuse relatively random features.

The As map (Figure 33c) shows comparable structures to the BSE image. Brighter segments correlate with the brighter portions of As. The rim structure of all crystals, described above in the BSE image, are clearly exhibited. The core structure in the crystal is also diffuse, following the zonation in the BSE image. At the top of the image is a brighter zone, which is part of the dark shape in the BSE image.

Lead (Figure 33i) exhibits similar zonation pattern as those exhibited in As map and the BSE image. Rim and core structures mimic the As distribution. One exception is the darker zone on the top of the BSE image, here the Pb content does not show the same effect.

Silver (Figure 33b), Au (Figure 33d), Co(Figure 33e) and Cu (Figure 33f) maps indicate weak zonation. Only at the rim zonation of the left crystal is a different distribution with less Ag visible. Thus, the core of the crystal exhibits a slightly higher content of the elements Ag, Au, Co and Cu.

Iron (Figure 33g) and S (Figure 33j) have As (and Ag, Au, Co and Cu respectively to the mentioned rim zonation of the biggest crystal) as the contrary element in times of content. The Fe element map is most comparable to the Ag, Au, Co and Cu maps, as fewer zonation structures are visible. The rim of the left crystal exhibits a higher Fe content. The S map shows the inverse of the As map.

The Sb map (Figure 33k) indicates less visible rims, which can be clearly seen in the As and S maps. Other, more detailed zonation is visible in the map; the smaller crystal in the bottom shows an "arch"-like structure. It slightly varies at the edges from zonation of As and S as well. In general, the Sb map shows zones that are not visible in As or the S maps, nor the BSE image.



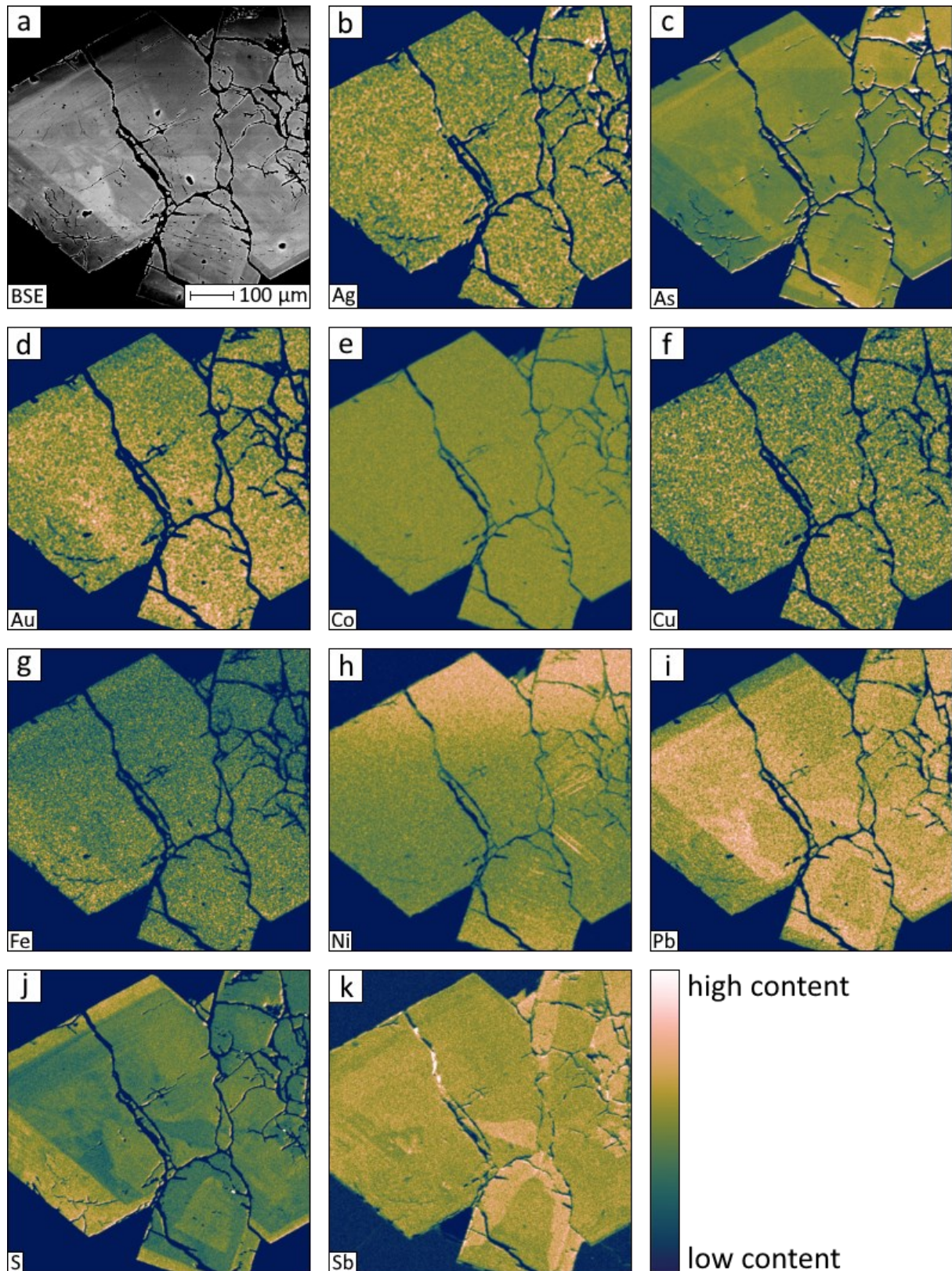


Figure 33: Arsenopyrite element maps in sample 22JH07b; a) BSE image; b) Ag EDS spectrometer; c) As WDS spectrometer; d) Au WDS spectrometer; e) Co EDS spectrometer; f) Cu EDS spectrometer; g) Fe EDS spectrometer; h) Ni WDS spectrometer; i) Pb EDS spectrometer; j) S EDS spectrometer; k) Sb WDS spectrometer.

Nickel (Figure 33h) shows a gradual decrease in the concentration over the maps, which again is likely related to beam drift. Still, in the right side of the image, smaller stripes of higher contents of Ni are exhibited.



#### 4.4.3 EPMA element map 22JH14b-map 1

In sample 22JH14b-map 1 a nearly euhedral crystal of arsenopyrite with a size of ~100  $\mu\text{m}$  was mapped. The lower right corner appears to be disconnected from the main crystal, with smaller rounded arsenopyrite pieces exhibited at the bottom of the image. In the BSE image (Figure 34a), a dark rim is visible on both the left and right side, partially streaked by smaller and brighter stripes. A slightly brighter rim is also noticeable at the top of the crystal. The core is in general brighter. A main fracture is present in the core, almost dividing the crystal into two pieces. By far the brightest part of the whole image is visible within this fracture. Several holes are also visible in the crystal.

The As element map (Figure 34c) mimics the pattern if the zonation of the BSE image. Darker rims on the left and right side of the crystal, a brighter in the upper part of the arsenopyrite/crystal. In general, the core has a higher As content. Wherever smaller fractures are visible in the BSE image, the content of As is increased. The element distribution of Pb (Figure 34i) is comparable with the As map. The rim as well as the smaller fractures in the arsenopyrite is visible. The inverse pattern is shown by the S map (Figure 34j), also the fracture zones were brighter in this map. Iron shows no clear zonation (Figure 34g).

The Ag (Figure 34b) and Au maps (Figure 34d) show a vaguely similar zonation than the ones visible in the As map and the BSE image. The left and right rims are faintly visible and show darker structures, thus indicating lower Ag and Au contents. The main fracture within the crystal reveals an elevated content of Au and there is a noticeable along its entire length.

The element distribution of Co (Figure 34e) differs from the already mentioned elemental maps and shows increased contents of Co especially in the core of the crystal. While in the map of As, Pb, S and Sb is clearly a variation between the horizontal and vertical rims of the crystal, Co content is at all four edges (rims) the same. The Ni (Figure 34h) map exhibits similar rim and core features as the ones in the Co map, including the bright streak at the top and bottom and the blob at the left bottom.

Antimony (Figure 34k) shows a markedly different zoning compared to the other elements. Still, some similarities are present. The rims on the left and right sides, which are also noticeable in the majority of the other maps, are also visible. However, the rim zonation at the top and bottom of the crystal is more pronounced. A zone composed of stripes in the middle of the arsenopyrite is exhibited. The main fracture, intersecting from top-left through bottom-right, is also elevated in Sb. The smaller pieces of arsenopyrite in the right bottom part are also elevated in Sb, mainly at the rims and edges of the smaller crystal parts connecting them with the main crystal. The Cu map (Figure 34f) is the only one that exhibits no visible zoning.

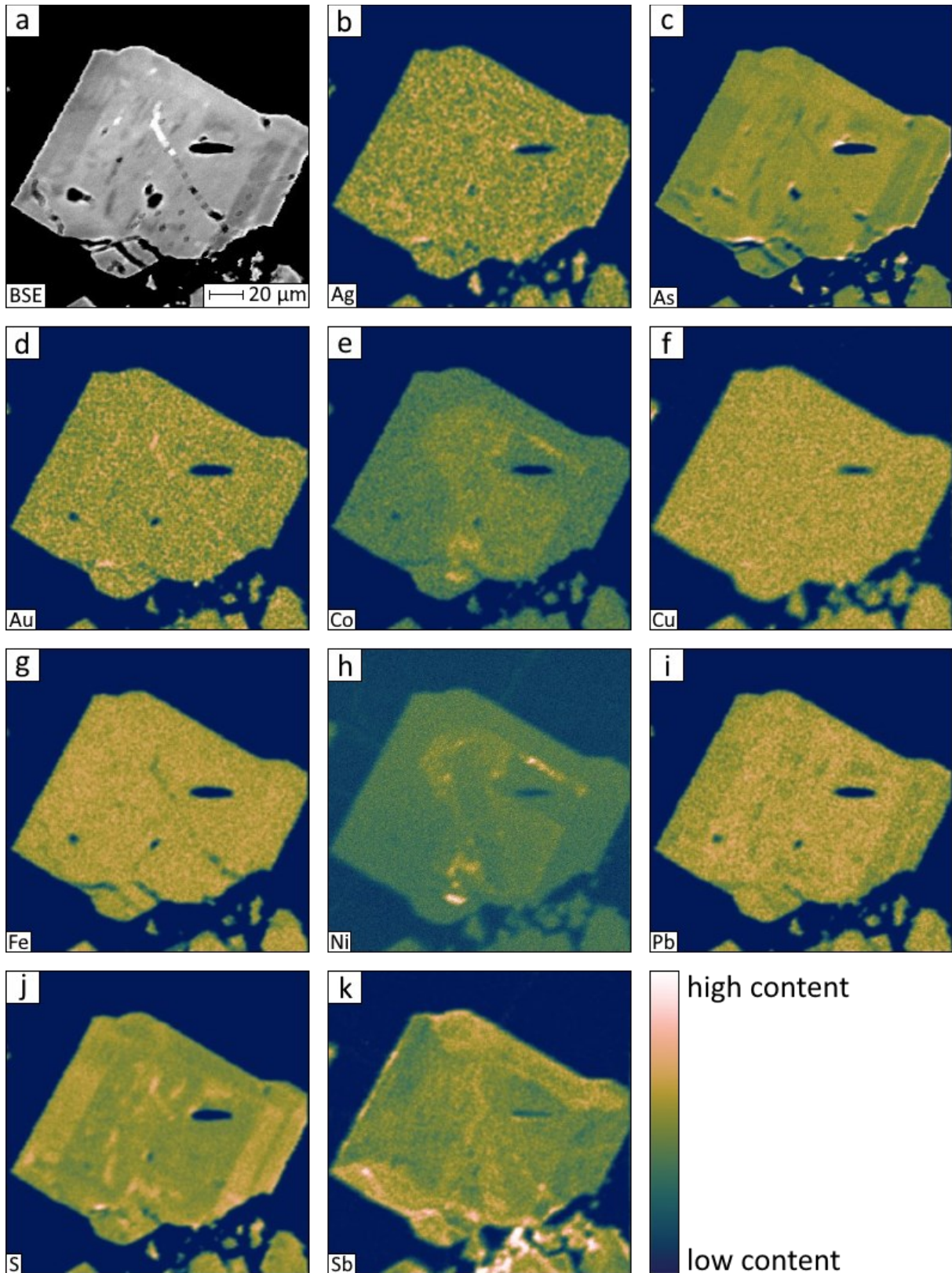


Figure 34: Arsenopyrite element maps in sample 22JH14b-1; a) BSE image; b) Ag EDS spectrometer; c) As WDS spectrometer; d) Au WDS spectrometer; e) Co EDS spectrometer; f) Cu EDS spectrometer; g) Fe EDS spectrometer; h) Ni WDS spectrometer; i) Pb EDS spectrometer; j) S EDS spectrometer; k) Sb WDS spectrometer.



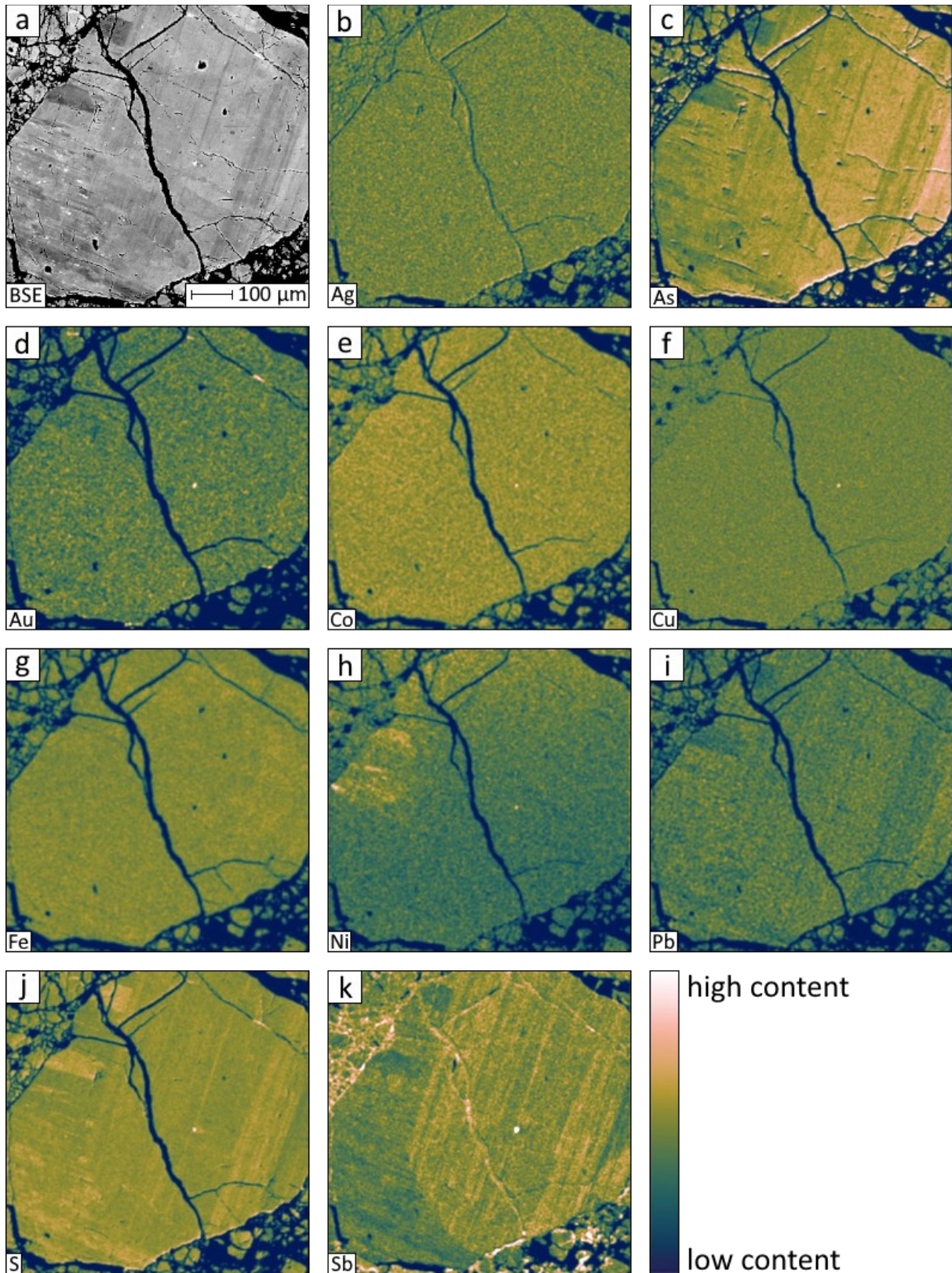


Figure 35: Arsenopyrite element maps in sample 22JH14b-map 2; a) BSE image; b) Ag EDS spectrometer; c) As WDS spectrometer; d) Au WDS spectrometer; e) Co EDS spectrometer; f) Cu EDS spectrometer; g) Fe EDS spectrometer; h) Ni WDS spectrometer; i) Pb EDS spectrometer; j) S EDS spectrometer; k) Sb WDS spectrometer.

#### 4.4.4 EPMA element map 22JH14b-map 2

The map 22JH14b-map 2 shows an arsenopyrite (diameter  $\sim 600 \mu\text{m}$ ) which is bisected by a large fracture visible in the BSE image (Figure 35a). Finer zonation occurs near the edges of the crystal. The crystal boundaries exhibit rounding. Smaller arsenopyrites and remnants of pieces of the main one are found in the immediate vicinity of the main crystal. The BSE image displays oscillatory zoning with varying orientations. On the left side of the arsenopyrite, the stripes dip towards the right side at the bottom, while on the right side of the arsenopyrite the opposite occurs. The size of the stripes varies from only a few  $\mu\text{m}$  to a few tens of  $\mu\text{m}$ . Higher differences in brightness are visible at the top left, indicating a sector zoning. Partly, the fractures intersect the observed zoning on the right-hand side. On the left side of the crystal, several inclusions, visualized as bright spots, are visible.

Zoning displayed in the As element map (Figure 35c) correlates with the BSE image, oscillatory and sector zoning can be identified here. The number of individual stripes is less than of those visible in the BSE image. Holes and fractures on the surface of the crystal are observable. The Pb distribution (Figure 35i) exhibits a similar pattern to the As element map. However, the zoning is less visible compared to the As map and BSE image, but it corresponds to the same brighter spots. The opposite elemental distribution is visible in the S map (Figure 35j). Similar zoning to that in the BSE image, As and Pb maps are exhibited, but with the opposite distribution of elements. Oscillatory zoning is visible on both sides of the crystal and reveals a rounded boundary between both sides. The content of Sb (Figure 35k) is elevated and more dominant on the right side, with visible oscillatory zoning. Inclusions and fractures show an enrichment in Sb. Smaller arsenopyrite pieces surrounding the main crystal exhibit an elevated content of Sb. Overall, the increasing contents correlate with the elevated values of As and Pb.

The maps of S, Au, Cu, Co, Ni and Sb indicate that an inclusion is located on the right half of the crystal.

Silver (Figure 35b), Au (Figure 35d) and Cu (Figure 35f) exhibit no noticeable zonation in the EPMA element map, except for an increased content in the inclusion of Cu and Au, which was previously mentioned. However, for Au changes in the sector zonation sections at the top of the crystal are visible. Furthermore, a fracture at the top is enriched in Au as well.

Iron (Figure 35g) displays a diffuse segregation in the distribution of elements. It is only partially comparable to the As or S zoning. Zoning in Co (Figure 35e) is not evident. The inclusion already mentioned in the description of Au, Cu and S is also elevated in Co. Parts of the sector zoning are slightly enriched in Co, while the distribution of Au and As is lesser. Nickel (Figure 35h) is elevated in the upper left part of the crystal, correlating with the BSE, As, and Pb zoning. The top appears to be dominated by a gradual zonation of elements, a characteristic that is not consistent across the entire element map. In contrast, the remaining part of the crystal exhibits no zoning.

#### 4.4.5 EPMA element map 22JH10

Map 22JH10 shows a single rounded arsenopyrite crystal with a few smaller crystals of arsenopyrites on the top right part of the map. The BSE image (Figure 36a) shows sector as well as oscillatory zonation. The upper left part displays several smaller streaks that gradually increase towards the right side until none are visible anymore. Some cracks and inclusions run parallel to the oscillatory zonation. The bottom part shows one nearly homogenous zone.



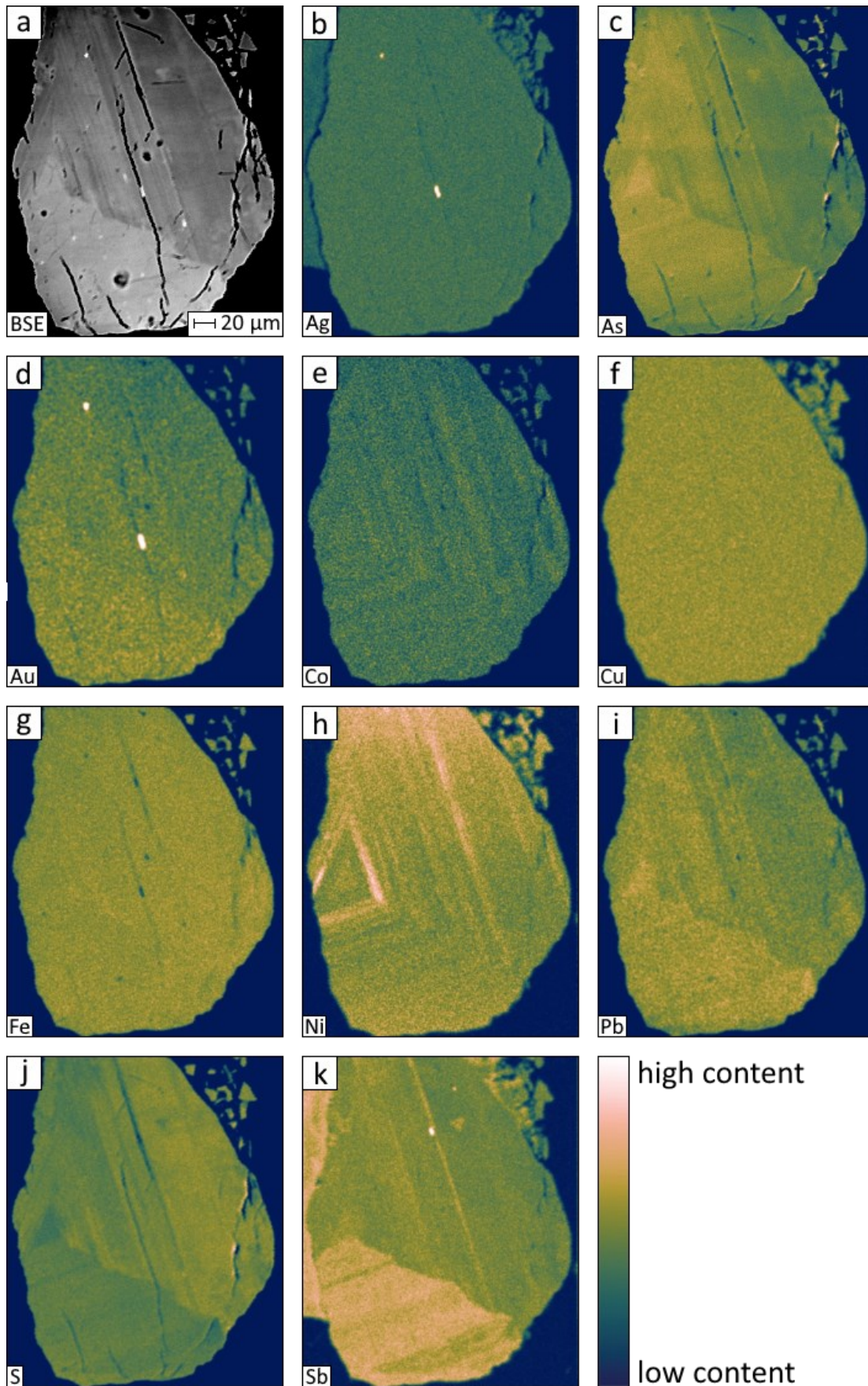


Figure 36: Arsenopyrite element maps in sample 22JH10; a) BSE image; b) Ag EDS spectrometer; c) As WDS spectrometer; d) Au WDS spectrometer; e) Co EDS spectrometer; f) Cu EDS spectrometer; g) Fe EDS spectrometer; h) Ni WDS spectrometer; i) EDS spectrometer; j) S EDS spectrometer; k) Sb WDS spectrometer.



Arsenic (Figure 36c) demonstrates similar characteristics to the BSE image, revealing even more details of zoning. It becomes apparent that the zonation is triangular shaped and covers the entire crystal. A similar pattern is evident in the Pb map (Figure 36i), while the S map (Figure 36j) shows the inverse pattern.

Gold (Figure 36d) displays two main zones within the crystal. The upper part of the crystal exhibits a gradual decrease in content from the left to the right side. The bottom part of the arsenopyrite is generally higher in Au. Two inclusions in a hole and a fracture in the crystal show a higher content of Au. Silver (Figure 36b) only exhibits enrichment in the same inclusions as observed in the Au map and has no zonation in its map.

Nickel (Figure 36e) and Co (Figure 36h) show a similar triangular shaped oscillatory zonation over the whole crystal. The element distribution is comparable to each other, with the contrast being more visible in the element map of Ni. Additionally, there is a gradual decrease in content from the top to the bottom of the crystal visible for Ni, with only the upper part being homogeneously affected.

The element zonation of Sb (Figure 36k) is visible in two main parts. The oscillatory zonation observed in other element maps, such as As or Ni, is not as prominent. Still, stripes of varying element content and thickness are exhibited. The upper and lower parts of the crystal vary from each other, with respect to the content of Sb. Some inclusions enriched in Sb are visible. The element maps of Fe and Cu show the fewest zonation. Iron (Figure 36g) exhibits a slight zonation akin to the triangular shape visible in other elements (ex. As, Co, Ni). In contrary, the Cu (Figure 36f) content does not exhibit any changes.

## 4.5 LA-ICP-MS element maps of pyrite

In the following the results of the LA-ICP-MS element maps are presented. Each will be described to emphasize the main structures of elemental distribution visible in pyrite. The elements which are presented vary between the different maps. In the case that more than one map was created per sample, the maps are labeled.

### 4.5.1 LA-ICP-MS element map 22JH31a

In laser element map 22JH31a, a cutout of the crystal which is surrounded by Pb-phases, was used to prevent the contamination of the laser by Pb phases. The crystal is cut by two major vertical veinlets on the left and right, which appear bright in the BSE image (Figure 37a). In between these veinlets several inclusions, ranging from  $\sim 1 \mu\text{m}$  to  $\sim 30 \mu\text{m}$ , are noticeable. Note the black spots in the image, which are attributed to holes in the pyrite and can show streaks during the LA-ICP-MS measurement. The largest hole on the bottom of the image is visible in almost every element map and is ignored for the subsequent descriptions. Over the whole surface the pyrite contains cloudy spots that vary slightly in brightness.

In the main text we are only showing the element maps (Figure 37b-n) for elements which show notable signals in the laser maps. These include the signals for Ag, As, Au, Bi, Cu, Ga, In, Ni, Mo, Sb, Sn, Pb and Zn. All other (Co, Ge, Hg, Fe, Te, Tl and Se) are only shown in the appendix.

Similar element patterns can be seen in As, Au, and Ni maps with differences in signal strength. Nickel in (Figure 37j) exhibits an overall diffuse impression, especially in the middle part of the crystal. Still, some signs of rectangular zonation can be seen on the right side of the image. Within the zonation, the content of Ni fluctuates showing minor zoning. The “diffuse” core in the Ni zonation matches in many places the zonation of As (Figure 37c). In general, the content on As decreases in the direction to the core, showing a sharp boundary. The veinlet on the right side of the map and several inclusions shows elevated As.

The zonation of Au (Figure 37d) is partly comparable to the As and Ni maps. Note, that around the diffuse core, the Au distribution matches with the distribution of As. The Ni signal shows additional zones that are not present in the Au nor As maps. The rectangular zonation of Ni on the right side can be partly seen in the image of Au.

Compared to the element maps of As, Au and Ni, the remaining elements do not play a major role in the general structure of the pyrite. The elements Ag (Figure 37b), Cu (Figure 37f), Sb (Figure 37l), Pb (Figure 37k) and Zn (Figure 37n) do show a similar pattern of element distribution. Ag is present in both veinlets, with the one on the right having even higher Ag contents. The largest inclusions visible in the BSE image tend to have an elevated content of Ag, which can be also found in smaller inclusions. The bright spot in the middle of the Ag map can be related to the black spots in the BSE image.

The Sb map shows a similar pattern to Ag. Both veinlets show elevated Sb, with the right veinlet containing more than the left one. The inclusions noted in the Ag map are also elevated in Sb. The Cu map shows similar features to the Ag and Sb maps. Both veins are visible, while the right one has an increased content of Cu. The Ag/Sb inclusions are also enriched in Cu. Nonetheless, the smaller inclusions ( $< 10 \mu\text{m}$ ) show an increased amount of Cu. Pb content is generally elevated in the veinlets and inclusions in the pyrite. Note that there is almost the same distribution of Pb in both veins. Both the large and small inclusions have high Pb contents.

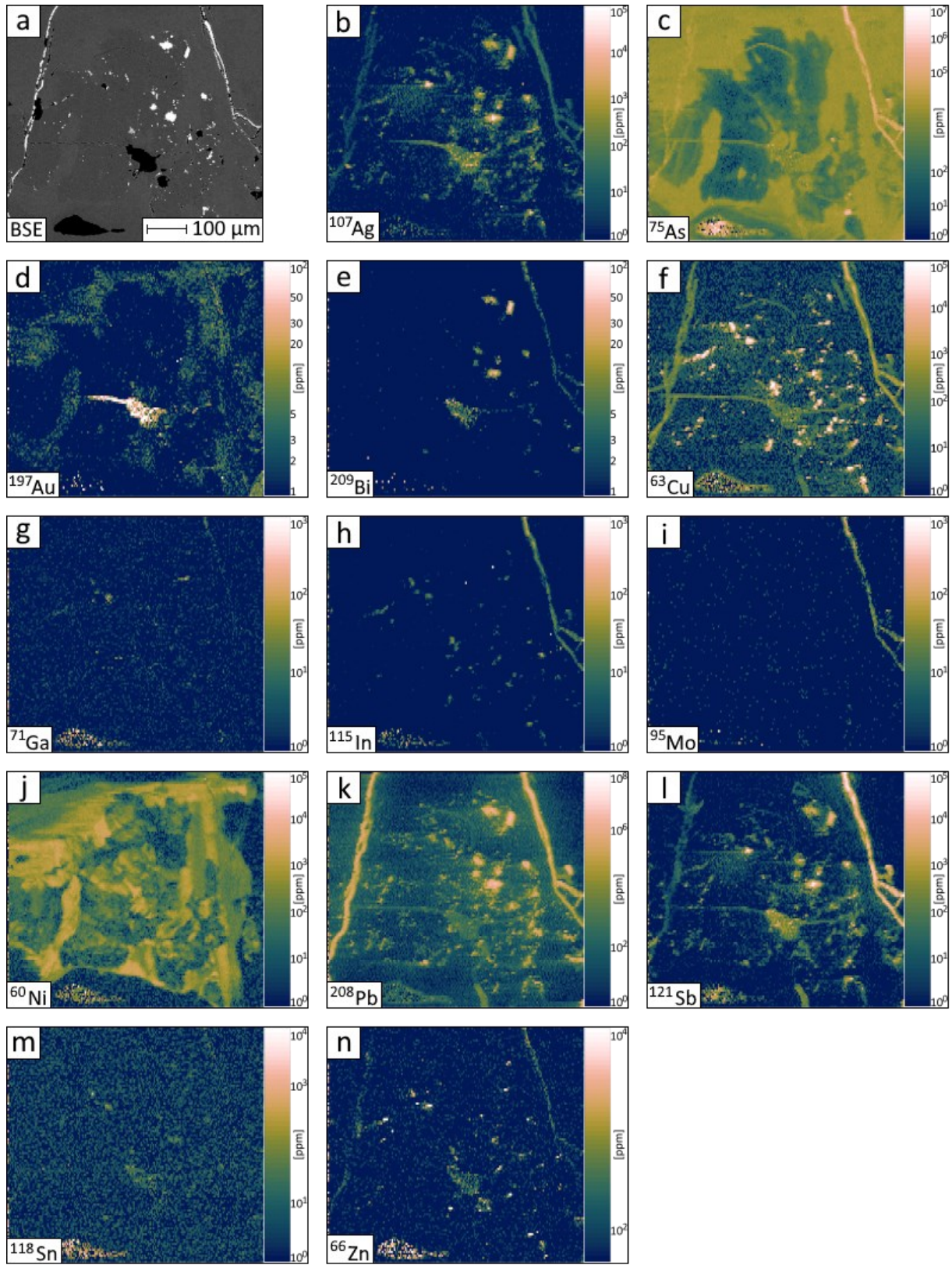


Figure 37: Pyrite LA-ICP-MS element map 22JH31a; a) BSE image; b)  $^{107}\text{Ag}$ ; c)  $^{75}\text{As}$ ; d)  $^{197}\text{Au}$ ; e)  $^{209}\text{Bi}$ ; f)  $^{63}\text{Cu}$ ; g)  $^{71}\text{Ga}$ ; h)  $^{115}\text{In}$ ; i)  $^{95}\text{Mo}$ ; j)  $^{60}\text{Ni}$ ; k)  $^{208}\text{Pb}$ ; l)  $^{121}\text{Sb}$ ; m)  $^{118}\text{Sn}$ ; n)  $^{66}\text{Zn}$ .

The Zn map resembles the Ag, Cu, Sb and Pb maps. Nonetheless, the Zn content is generally lower than of the Ag, Cu, Sb, and Pb, but still visible in the veins and inclusions. Cu, Pb and Zn display a low signal from the black spot of the BSE image.

Bismuth (Figure 37e), Ga (Figure 37g), In (Figure 37h) and Mo (Figure 37i) maps show generally similar features. The right veinlet of the pyrite displays a distribution of elements with varying contents. The inclusions exhibit distinct affinities for these elements. For instance, Bi is elevated in the largest inclusion, while In is predominantly present in the smaller ones. Molybdenum is entirely absent in the inclusions and Ga is generally low in them.

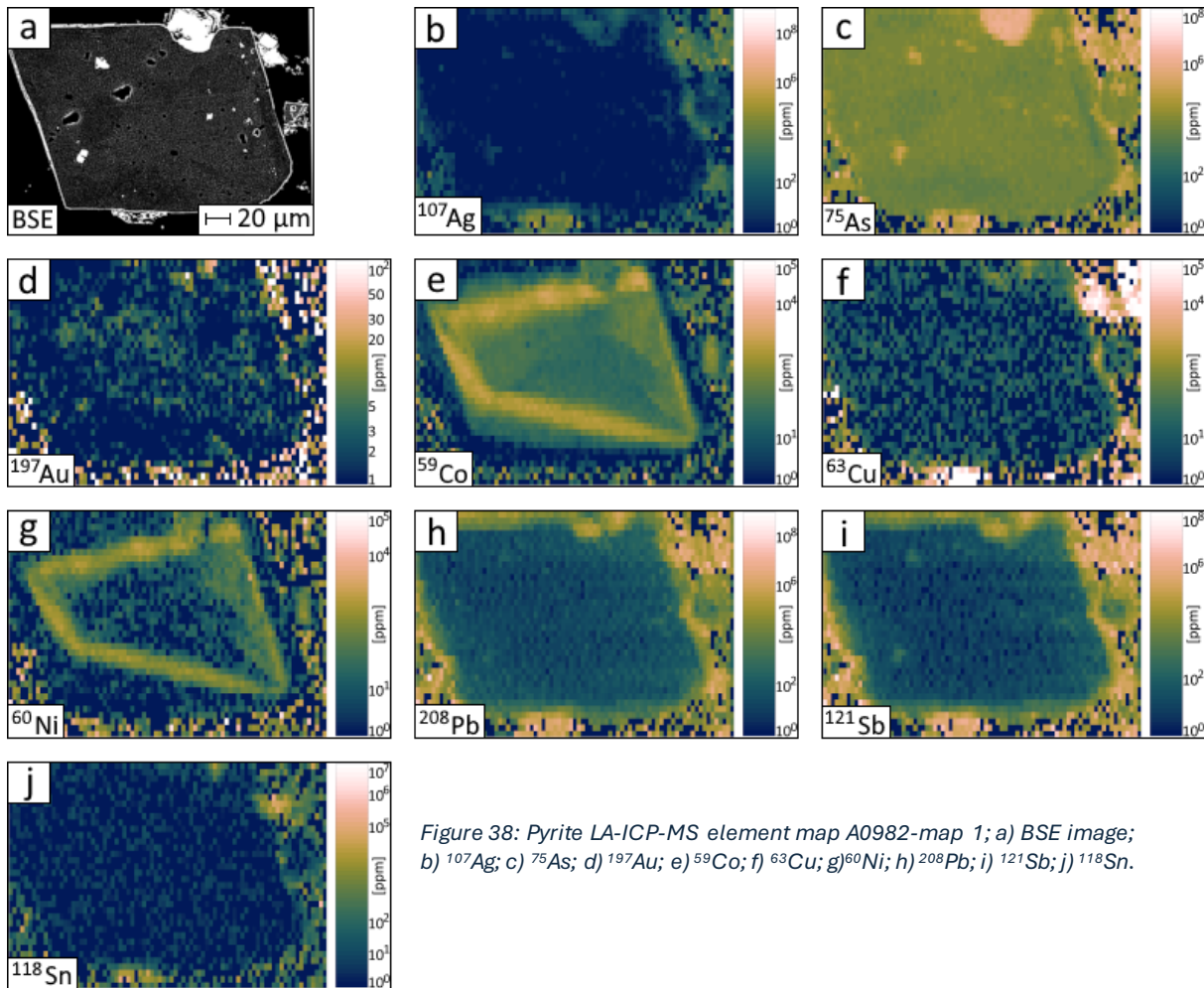


Figure 38: Pyrite LA-ICP-MS element map A0982-map 1; a) BSE image; b)  $^{107}\text{Ag}$ ; c)  $^{75}\text{As}$ ; d)  $^{197}\text{Au}$ ; e)  $^{59}\text{Co}$ ; f)  $^{63}\text{Cu}$ ; g)  $^{60}\text{Ni}$ ; h)  $^{208}\text{Pb}$ ; i)  $^{121}\text{Sb}$ ; j)  $^{118}\text{Sn}$ .

#### 4.5.2 LA-ICP-MS element map A0982-map 1

The BSE image (Figure 38a) shows a nearly euhedral pyrite crystal from sample A0982. Several smaller inclusions, with a maximal size of  $\sim 5 \mu\text{m}$ , of arsenopyrite are present in the crystal. A larger crystal is exhibited at the right side of the pyrite, while other smaller crystals are at the bottom of the pyrite. These smaller crystals, as well as the main crystal, have a small alteration selvage around them. Note that signals around the crystal are mostly analytical artefacts.

In general, the content of As (Figure 38c) is constant and only varies slightly in some parts. Inclusions and the arsenopyrite crystal, which is visible in the BSE image, are highly elevated in As. Gold shows a distribution in the whole crystal that varies frequently. The inclusion of arsenopyrite is enriched in Au



(Figure 38d). The same pattern of enriched inclusions is visible in the Ag map (Figure 38b). However, there is no visible zonation of Ag in the pyrite crystal itself.

Cobalt (Figure 38e) shows a rim as zonation in the pyrite, nearly following the rectangular structure of the crystal. In the middle of this structure, as well as the rim-zonation, there is elevated Co. The Ni map (Figure 38g) shows similar features to Co, but in lower concentrations. The rim-like feature is still visible, however, the contents in and around it are far less compared to Co.

The concentration of Pb (Figure 38h) and Sb (Figure 38i) in the arsenopyrite is low in comparison to As, Ni and Co. The content of Pb and Sb are concentrated along the rim, likely related to the selvage around the crystal visible in the BSE image. Copper (Figure 38f) and Sn (Figure 38j) contents are also elevated on the selvage. It is also notable that Sb, and to a lesser degree Pb, is enriched in the inclusions.

#### 4.5.3 LA-ICP-MS element map A0982-map 2

Laser element map A0982-map 2 (Figure 39) shows only a portion of a much larger crystal. The full optical microscopy image of the crystal can be seen Figure 31. The maps of Fe, Mo, and Te which show no significant zonation or distribution and can be seen in the appendix.

The BSE image (Figure 39a) shows a portion of the pyrite, which is crosscut by several veinlets, which can reach a thickness of 10  $\mu\text{m}$ . Two main veinlets which cut from the bottom to the top of the image, have the same source. Parallel to these veinlets are smaller veins to the left of them. A varied network of horizontal veins interconnects vertically with each other within the structure. Generally, no zonation is discernible within the crystal in the BSE image. Nonetheless, there are some inclusions of euhedral arsenopyrite within the pyrite.

Note that at the material shown outside of the targeted pyrite may show elevated contents of the shown element, this is an artifact from the data reduction stage which assumes a set content of the internal standard element ( $S = 53.45 \text{ wt\%}$  for pyrite). The areas outside of the target pyrite crystals should therefore be disregarded.

Arsenic (Figure 39c), Au (Figure 39d) and Co (Figure 39f) and Ni (Figure 39k) are all present in the pyrite. The map of As shows enrichment in nearly the whole crystal, with only some parts of the core being depleted. Inclusions of arsenopyrite are noticeable as being saturated on the color scheme. Many of the veinlets are also enriched in As.

Cobalt (Figure 39f) and Ni (Figure 39k) show a slightly different zoning pattern. The outer part of the crystal has an almost rectangular enrichment of Co, which decreases towards the middle. The core is rectangular in shape and contains almost no Co. Similar patterns are visible in the Ni map (Figure 39k). The vertical veins do not contain Co nor Ni, while the horizontal veins are slightly enriched in Co. Compared to the element maps of As, Ni and Co, the element map of Au (Figure 39d) shows similar zonation styles. The rectangular shape is visible in the Au maps and the vertical, and some horizontal veinlets, are enriched in Au.

The fractures within the pyrite are mostly filled with a Pb rich phase (Figure 39l). Different veins, that are not visible in the BSE image, are visible on the Pb map. Also, several inclusions are noticeable on the Pb map. The rim of the pyrite is surrounded by Pb. Notable are the varying contents Pb between both main vertical veinlets.

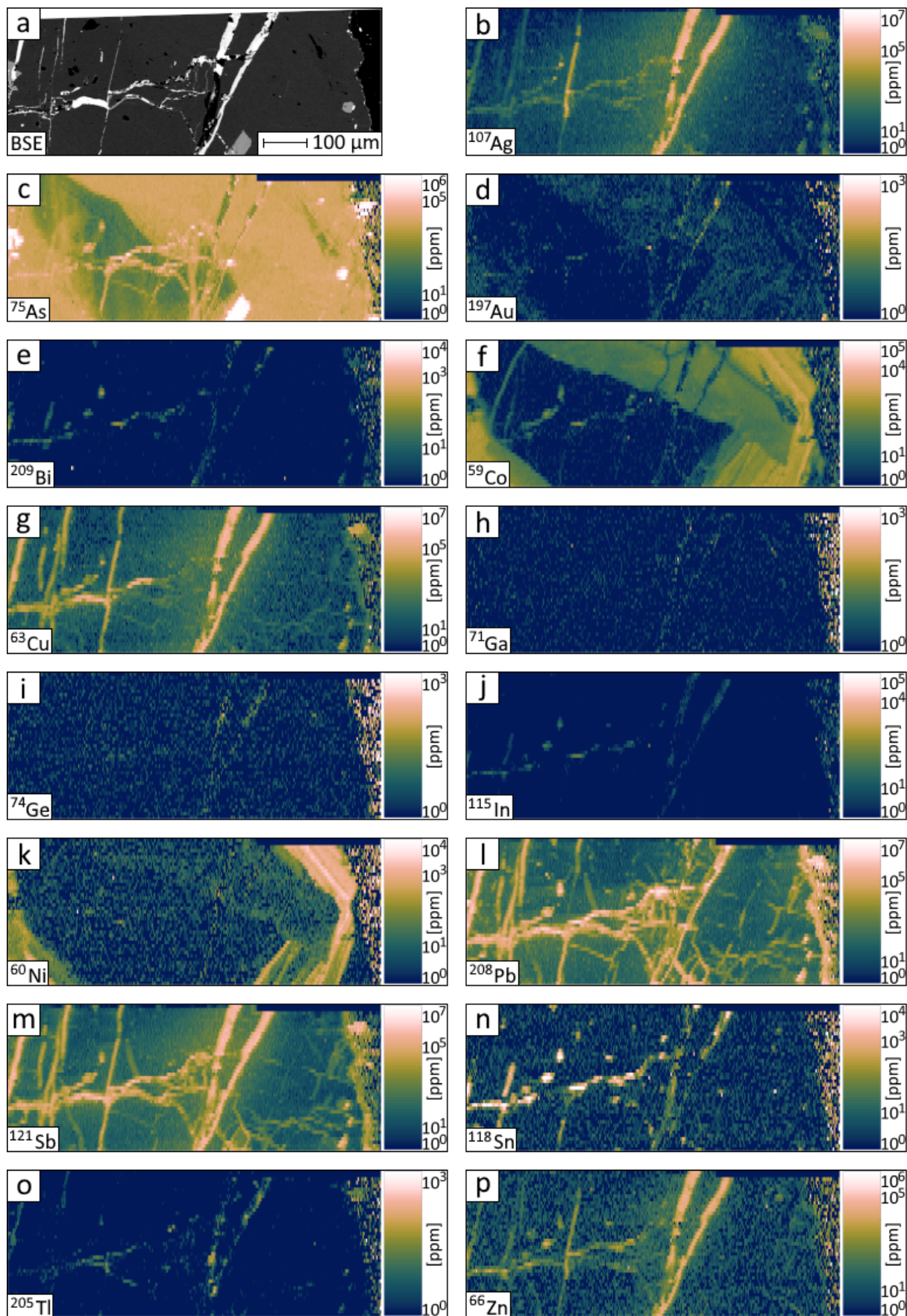


Figure 39: Pyrite LA-ICP-MS element map A0982-map 2; a) BSE image; b)  $^{107}\text{Ag}$ ; c)  $^{75}\text{As}$ ; d)  $^{197}\text{Au}$ ; e)  $^{209}\text{Bi}$ ; f)  $^{59}\text{Co}$ ; g)  $^{63}\text{Cu}$ ; h)  $^{71}\text{Ga}$ ; i)  $^{74}\text{Ge}$ ; j)  $^{115}\text{In}$ ; k)  $^{60}\text{Ni}$ ; l)  $^{208}\text{Pb}$ ; m)  $^{121}\text{Sb}$ ; n)  $^{118}\text{Sn}$ ; o)  $^{205}\text{Tl}$ ; p)  $^{66}\text{Zn}$ .

The Sb map (Figure 39m) shows increased Sb contents in the veinlets as well. However, the content is in the vertical veinlet the highest. In the selvage of the crystal, elevated Pb and Sb can be seen.

Copper (Figure 39g) is as well elevated in some veinlets, but in contrast to Pb and Sb, is generally only in the largest ones (with a few exceptions). The same is true for the distribution of Ag (Figure 39b) and Zn (Figure 39p), but Ag occurs as well in fewer smaller cracks. The vertical veinlets contain more Ag compared to the horizontal ones and Ag, Cu and Zn are found in higher concentrations in the selvage of the crystal.

Bismuth (Figure 39e), In (Figure 39j), Sn (Figure 39n) and Tl (Figure 39o) are present in the veinlets, mostly on the main ones. The content of those elements varies in the veinlets, and it appears that some of them are accumulated at some points. Gallium (Figure 39h) and Ge (Figure 39i) show the lowest contents. These elements are mainly found in the vertical main veinlets.

#### 4.5.4 LA-ICP-MS element map 22JH14b-map 1

Element map 22JH14b-map 1 exhibits a euhedral pyrite. Visible in the pyrite are diffuse and spotty zoning (Figure 40a). Several small holes and inclusions are also noticeable in the BSE image. Note that quartz surrounds the pyrite, which might lead to some artefacts. The element maps of the elements Bi, Fe, Ga, Ge, In, Mo, Te and Tl are not shown in the main text due to low concentrations but can be found in the appendix.

Arsenic is distributed in the whole crystal (Figure 40c), there are only slight changes in the content of the element. Gold (Figure 40d) is diffusely dispersed in the pyrite. In general, the rim region and as well the innermost core seem to be enriched in Au.

Cobalt (Figure 40e) and Ni (Figure 40g) exhibit an almost complete ring like zone, while Ni appears with a lower content. Lead (Figure 40h) is enriched in inclusions or in structures that resemble a veinlet system as well as in the surrounding of the pyrite. Silver (Figure 40b) appears to mimic the Pb content distribution. However, the rim areas of the pyrite crystals contain less Ag. A similar trend is observed for Sb (Figure 40i), where the Sb content is enriched on the edges of the crystal.

Copper (Figure 40f) displays a spotty distribution, with the rim exhibiting higher concentrations compared to the core, mirroring the patterns observed for Pb and Sb. Tin (Figure 40j) and Zn (Figure 40k) appear with no clear zonation pattern, but rather a spotty content distribution. Some “black spots” of the in the BSE image appear to be enriched by Sn and Zn.

#### 4.5.5 LA-ICP-MS element map 22JH14b-map 2

The BSE image shows a rounded appearance along the edges of the pyrite crystal (Figure 41a). Smaller fragments of pyrites and arsenopyrites are distributed in the surrounding area and appear to be linked through a selvage structure. Cracks and mineral inclusions are also observable in the BSE image. The central portion of the largest and, consequently, primary crystal appears darker, while the surrounding regions typically exhibit brighter hues. Note that quartz surrounds the pyrite which might lead to artefacts in the data. Some of the inclusions show halos in some of the maps.

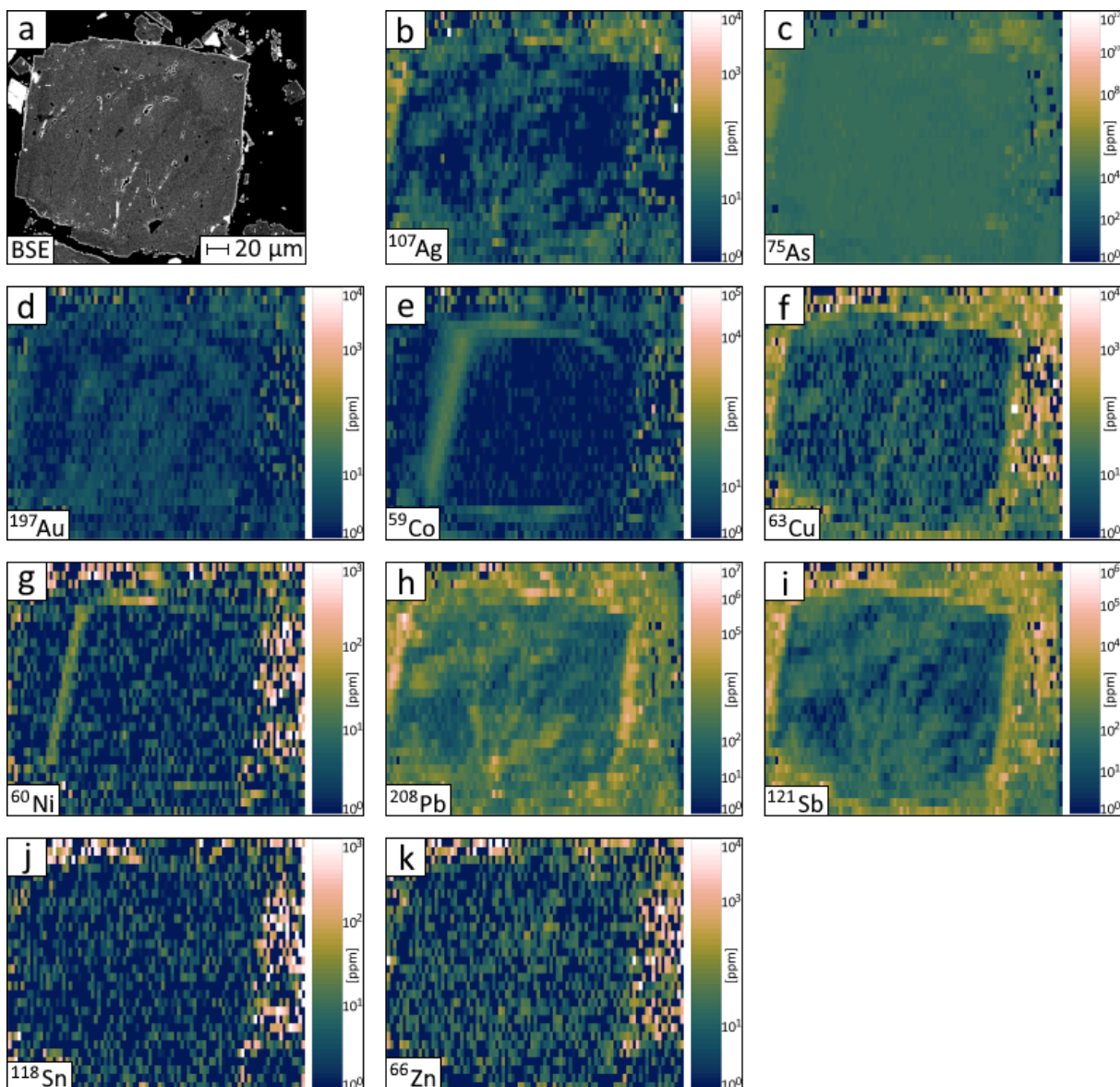


Figure 40: Pyrite LA-ICP-MS element map 22JH14-map 1; a) BSE image; b)  $^{107}\text{Ag}$ ; c)  $^{75}\text{As}$ ; d)  $^{197}\text{Au}$ ; e)  $^{59}\text{Co}$ ; f)  $^{63}\text{Cu}$ ; g)  $^{60}\text{Ni}$ ; h)  $^{208}\text{Pb}$ ; i)  $^{121}\text{Sb}$ ; j)  $^{118}\text{Sn}$ ; k)  $^{66}\text{Zn}$ .

Arsenic (Figure 41c) appears to be absent in the core of the pyrite. Instead, As is elevated in the rim, the selvage, fractures and some inclusions. Gold (Figure 41d) replicates the pattern observed for As, albeit in lower contents. It is generally enriched in the rim, and deficient in the core. Elevated Au is also found in the smaller arsenopyrites and the alteration selvage. In contrast, Pb (Figure 41i) and Sb (Figure 41j) are more widely dispersed within the alteration zones and fractures throughout the entire crystal. For both elements, it holds true that their contents are notably elevated in the selvage and in the cracks. Additionally, Sb is enriched in the small arsenopyrite.



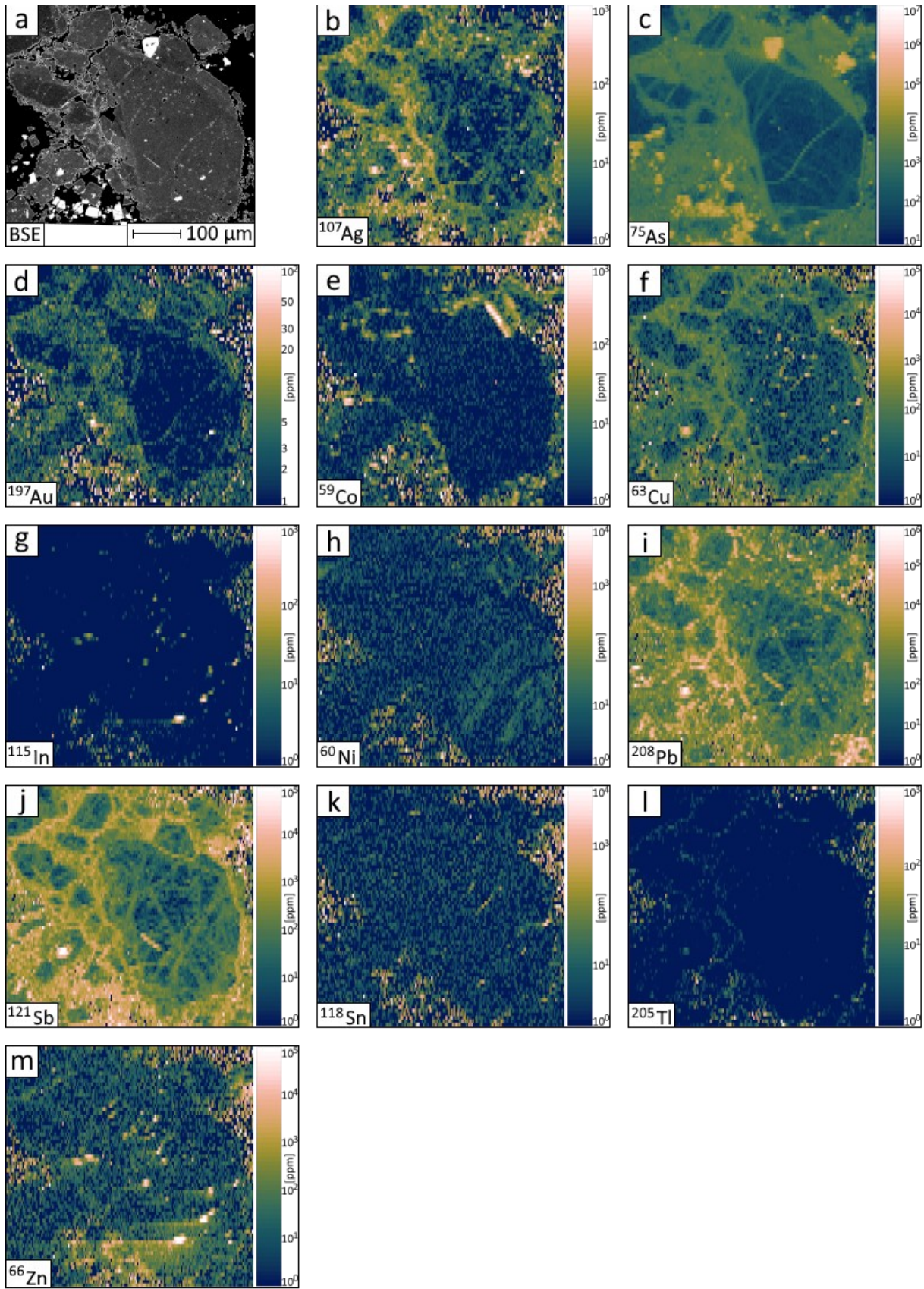


Figure 41: Pyrite LA-ICP-MS element map 22JH14-map 2; a) BSE image; b)  $^{107}\text{Ag}$ ; c)  $^{75}\text{As}$ ; d)  $^{197}\text{Au}$ ; e)  $^{59}\text{Co}$ ; f)  $^{63}\text{Cu}$ ; g)  $^{115}\text{In}$ ; h)  $^{60}\text{Ni}$ ; i)  $^{208}\text{Pb}$ ; j)  $^{121}\text{Sb}$ ; k)  $^{118}\text{Sn}$ ; n)  $^{66}\text{Zn}$ ; m)  $^{66}\text{Zn}$ .

Copper (Figure 41f) and Ag contents (Figure 41b) exhibit enrichment in the selvage and vein zones. Notably, Cu is enriched in smaller inclusions within the pyrite, while Ag dominates in the selvages and displays less dispersion in the inclusions. In (Figure 41g) and Zn (Figure 41m) are generally only elevated in inclusions. These differ from those elevated in Cu. Sn (Figure 41k) is also elevated in inclusions, veinlet, and the main crystal.

The distribution patterns of Co (Figure 41e) and Ni (Figure 41h) contrast with those previously described. Nickel is distributed in stripes within the core of the pyrite but is almost entirely excluded from the selvage. Cobalt appears to be enriched in certain selvage zones. Tl (Figure 41l) is dispersed within the selvages and conspicuously avoids the crystals altogether.

## 4.6 Chalcopyrite in-situ spot analyses

Sample 22JH31a is the only sample that contains chalcopyrite out of the investigated samples (Table 7). Therefore, spot analyses for trace elements of this mineral were conducted. A statistical summary has been prepared (Table 11). The mean value, P95 and P05 were used to prevent impact results of extreme outliers. Half of the LOD was used to calculate the median when values are below the LOD.

Analyses with LA-ICP-MS downhole spectra led to the assumption that inclusions in the chalcopyrite were hit. Therefore, in Table 12 suspected inclusions that might have been hit during the session, have been deleted.

*Table 11: Chalcopyrite in-situ spot analyses statistics with suspected inclusions. Mean value, P95, P05, N (number of individual analyses with the LA-ICP-MS) and n (number of analyses below the LOD) and the mean value of the LOD depicted. The mean value, P95 and P05 are in ppm.*

	Mean	P95	P05	N	n	LOD mean
<b>Ag</b>	269.78	785.83	67.49	29	17	0.19
<b>As</b>	5281.98	37596.26	4.46	29	19	4.40
<b>Au</b>	0.44	2.11	0.02	29	18	0.07
<b>Bi</b>	0.07	0.17	0.02	29	22	0.07
<b>Cd</b>	9.91	15.12	5.98	29	0	1.91
<b>Co</b>	0.14	0.43	0.05	29	23	0.17
<b>Cr</b>	1.34	3.04	0.34	29	22	1.12
<b>Ga</b>	0.36	1.04	0.10	29	5	0.16
<b>Ge</b>	0.37	0.62	0.17	29	14	0.35
<b>Hg</b>	3.05	6.94	0.66	29	8	1.64
<b>In</b>	32.14	44.75	16.52	29	0	0.07
<b>Mn</b>	1.48	6.81	0.16	29	21	0.55
<b>Mo</b>	0.99	1.52	0.06	29	28	1.95
<b>Ni</b>	0.69	1.60	0.27	29	24	0.78
<b>Pb</b>	12570.85	79427.66	5.77	29	0	0.50
<b>Sb</b>	165.10	521.56	3.28	29	0	0.12
<b>Se</b>	8.90	9.47	3.40	29	28	12.01
<b>Sn</b>	18.71	66.80	5.65	29	0	1.03
<b>Te</b>	<i>below LOD</i>	<i>below LOD</i>	<i>below LOD</i>	29	29	5.96
<b>Tl</b>	0.19	0.55	0.02	29	8	0.07
<b>V</b>	0.24	1.34	0.02	29	16	0.06
<b>Zn</b>	449.16	652.80	282.43	29	0	2.46

Table 11 shows clearly elevated content in Ag, As, Pb, Sb and Zn in the spot analyses. The content of Pb is reaching a mean value above 12,570 ppm. P95 shows an even higher content at 79,427.66 ppm. A similar behavior can be observed with As (mean = 5,281.98 ppm; P95 = 37,596.26 ppm). However, Table 12 points out that these high contents are related to inclusion that have been hit. Still, with mean values of 6.72 ppm for As and 14.43 ppm for Pb the contents are relatively elevated, but much lesser those of Pb or As. Silver shows a slightly different behavior. The mean content without inclusions (Table 12) is 139.03 ppm, almost the half of the value with hit inclusions (mean value = 269.78 ppm). Antimony content differs as well, with inclusions the mean value is 165.10 ppm and without 9.31 ppm. The high content of Zn in Table 11 (with inclusions) can still be observed in Table 12, with a mean value of 496.83 ppm.

Cadmium, Hg, In, Se and Sn were analyzed respectively and show moderate contents between 3.05 to 32.14 ppm as mean value (Table 11). Analyses without any inclusions show a similar range of content (Table 12).

Gold, Bi, Co, Cr, Mn, Mo and V contents within the chalcopyrite spot analyses with inclusions are relatively low (Table 11), excluding inclusion, the elements are not detected at all (Table 12). Gallium, Ge, Ni, and Tl contents are relatively low within the total analyses in Table 11 as well as in the analyses without inclusions and show mean values below 1 ppm. Tellurium was not detected in any analysis.

Table 12: Chalcopyrite in-situ spot analyses statistics with deleted suspected inclusions. Mean value, P95, P05, N (number of individual analyses with the LA-ICP-MS), n (number of analyses below the LOD) and the mean value of the LOD. The mean value, P95 and P05 are in ppm.

	Mean	P95	P05	N	n	LOD mean
Ag	139.03	246.87	79.80	9	0	0.22
As	6.72	10.87	4.44	9	1	2.05
Au	below LOD	below LOD	below LOD	9	9	0.07
Bi	below LOD	below LOD	below LOD	9	9	0.06
Cd	11.00	14.74	6.96	9	0	2.02
Co	below LOD	below LOD	below LOD	9	9	0.18
Cr	below LOD	below LOD	below LOD	9	9	1.12
Ga	0.26	0.40	0.16	9	4	0.17
Ge	0.43	0.53	0.30	9	3	0.31
Hg	3.66	5.91	2.29	9	2	1.88
In	28.09	37.62	17.19	9	0	0.05
Mn	below LOD	below LOD	below LOD	9	9	0.48
Mo	below LOD	below LOD	below LOD	9	9	1.89
Ni	0.70	0.70	0.70	9	8	0.79
Pb	14.43	39.26	4.37	9	0	0.19
Sb	9.31	18.57	2.54	9	0	0.11
Se	below LOD	below LOD	below LOD	9	9	11.97
Sn	9.90	16.88	5.23	9	0	0.94
Te	below LOD	below LOD	below LOD	9	9	7.48
Tl	0.20	0.47	0.07	9	2	0.07
V	below LOD	below LOD	below LOD	9	9	0.07
Zn	496.83	598.21	430.88	9	0	2.47



## 4.7 U/Pb age dating

During the U/Pb calcite age dating sessions several samples from the historic mining districts of Straßegg and Flatschach were examined (Table 13). Only a small number of samples were finally selected (in total 8), with the rest discarded due to lack of  $^{238}\text{U}$  or too high  $^{206}\text{Pb}$ .

Table 13: Final selected samples for U/Pb calcite dating and their location.

Sample ID	Latitude	Longitude	Mining district	Description
22JH11	4740095750	1553283900	Straßegg	Float sample
FL CA 1	4723515098	1473547303	Flatschach	Mine waste facility near adit Fuchs 1
F441	4723515098	1473547303	Flatschach	Mine waste facility near adit Fuchs 2
F562	4723515098	1473547303	Flatschach	Mine waste facility near adit Fuchs 3
FL AG 1	4724202912	1475404617	Flatschach	Urbani Unterbau
22GS52a	4723526114	1473511120	Flatschach	In-situ; adit Fuchs 1; approx. 10 meter inside; calcite vein 1
22GS52b	4723526114	1473511120	Flatschach	In-situ; adit Fuchs 1; approx. 10 meter inside; calcite vein 2
22GS52d	4723526114	1473511120	Flatschach	In-situ; adit Fuchs 1; approx. 10 meter inside; calcite vein 3

During the processing the laser spots with low contents of  $^{238}\text{U}$  or  $^{207}\text{Pb}$  were discarded. The laser ablation spots were checked after each run to make sure the phase targeted was hit. In case of failure, the measurement was excluded. Table 14 shows the overall data summarized.

### 4.7.1 U/Pb age dating Straßegg 22JH11a

Sample 22JH11a was the only sample from Straßegg, where U/Pb age dating was conducted. All other samples have been discarded, due to the high Pb content of the sample, most likely related to the second ore stage (Bojar *et al.*, 2001). In total 18 individual measurements were conducted in this sample (Figure 42a). Plotting the data in a Tera-Wasserburg plot results in an age of  $0.00011 \pm 0.56554$  Ma (Figure 42b). The sample 22JH11a contained still a lot of Pb, therefore, the age dating points have high uncertainties. The U/Pb ratio in this sample is very low.

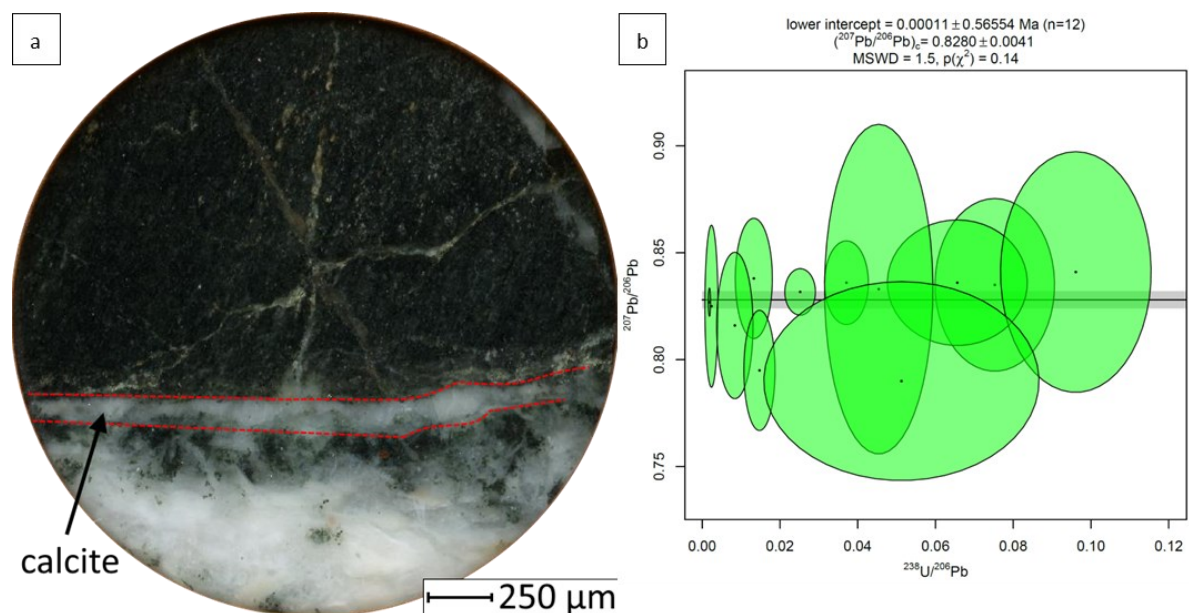


Figure 42: a) Overview picture of sample 22JH11a; b) Tera-Wasserburg plot for sample 22JH11a (Straßegg).

#### 4.7.2 U/Pb age dating Flatschach

##### 22GS52a

Sample 22GS52a (Figure 43a) can be assigned to the same location as sample 22GS52b and 22GS52d. The samples differ in different calcite veins, which have been observed. The laser spots of sample 22GS52a were generated in the calcite veins of the sample. The resulting age is  $3.90 \pm 0.39$  Ma with a relatively low Mean Square Weighted Deviation (MSWD) about 1.2 (Figure 43b).

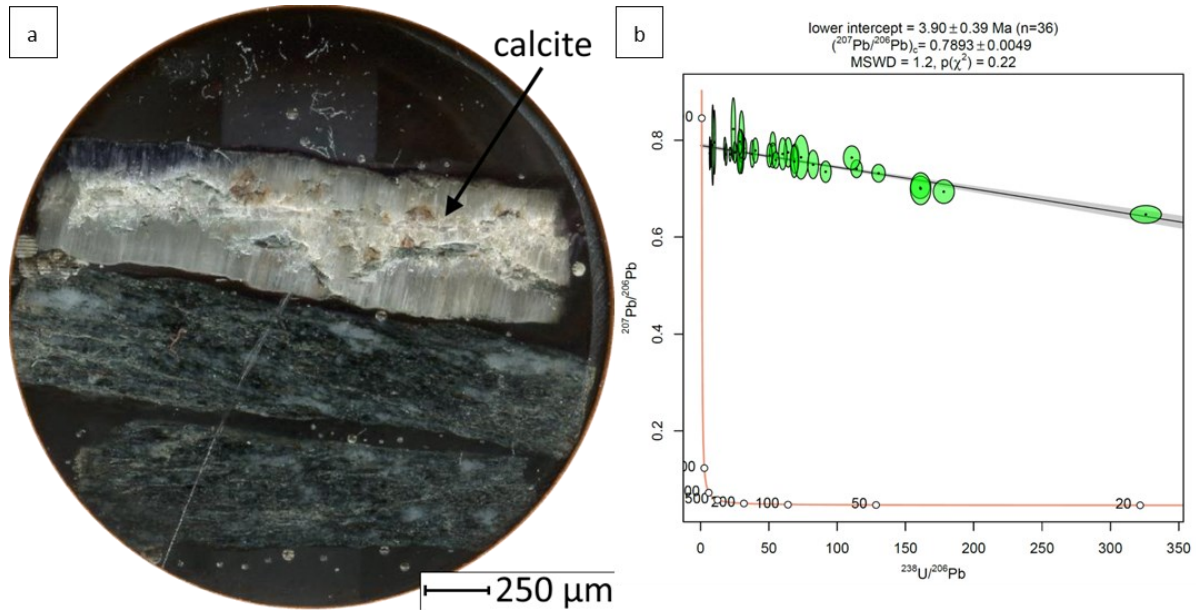


Figure 43: a) Overview picture of sample 22GS52a; b) Tera-Wasserburg plot for sample 22GS52a.

##### 22GS52b

Sample 22GS52b is related to the samples 22GS52a and 22GS52d, while each represents a different veinlet. Several pieces of the veinlet of sample 22GS52b have been taken together in one mount (Figure 44a). Laser spots have been made through all pieces with a result of  $4.2 \pm 1.2$  Ma (Figure 44b).

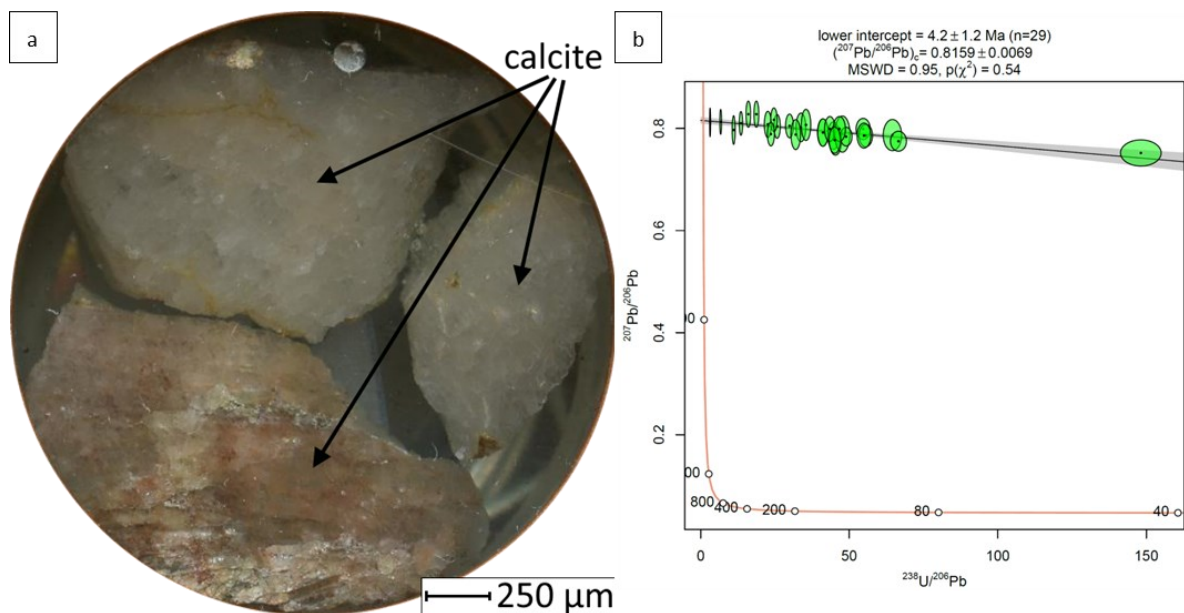


Figure 44: a) Overview picture of sample 22GS52b; b) Tera-Wasserburg plot for sample 22GS52b.

### 22GS52d

Sample 22GS52d (Figure 45a; b) shows several calcite generations. Main calcites are orange calcites and a white calcite. Both contain several veinlets, which have been tried to analyze but failed due to their size. A single veinlet in between the sample resulted in promising results (Figure 45c; d). The white calcite contained high Pb and low U contents and is therefore not presented here but can be seen in appendix.

The orange calcite resulted in an age of  $17.4 \pm 1.1$  Ma with a MSWD of 1.8, while the veinlet, which cuts through the orange calcite shows an age of  $5.08 \pm 0.47$  Ma.

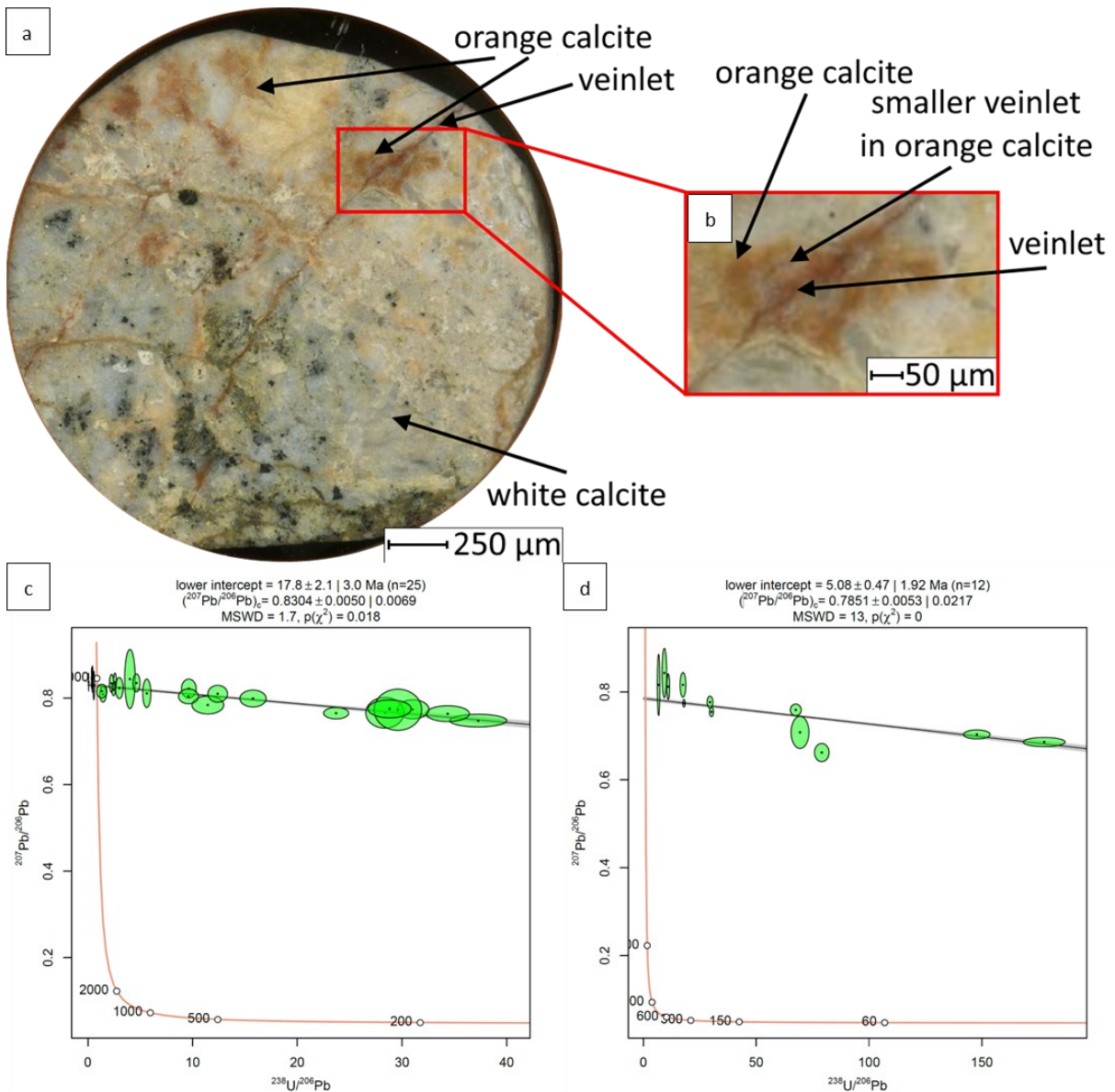


Figure 45: a) Overview picture of sample 22GS52d; b) Tera-Wasserburg plot for sample 22GS52d, orange calcite and c) veinlet.

### F562

The age determination for sample F562 indicates a relatively young age (3.5 Ma), with a considerable uncertainty  $\pm 12$  Ma (Figure 46a; b). Calcite is found alongside quartz in this sample, and sulfides are dispersed throughout the entire sample, situated in proximity to both calcite and quartz. MSWD is 0.61.



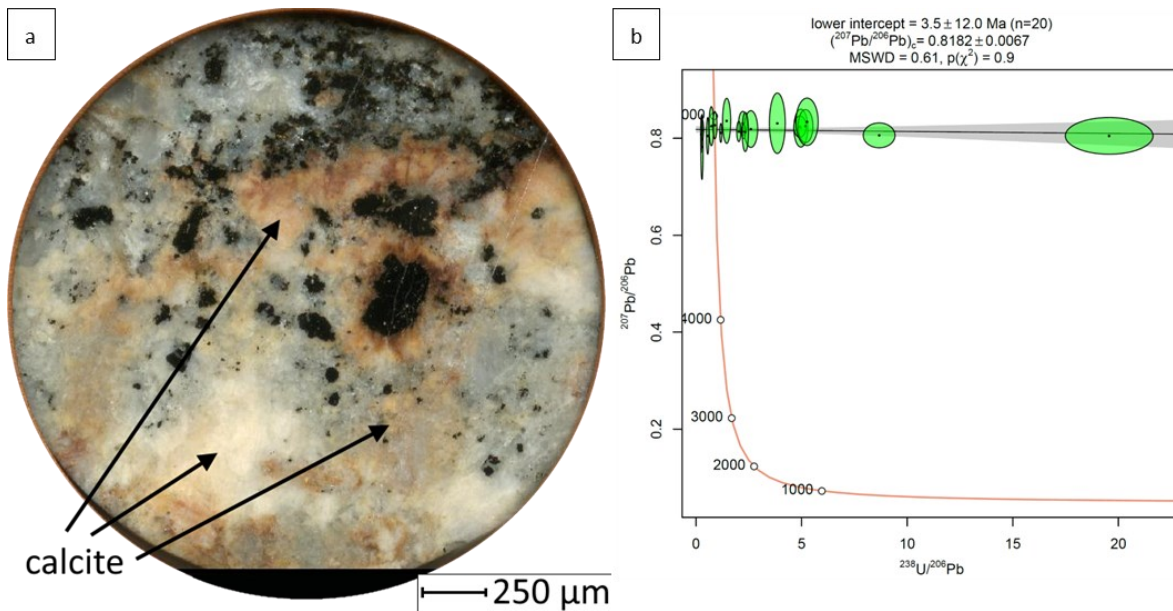


Figure 46: a) Overview picture of sample F562 with b) Tera-Wasserburg plot for the sample.

#### FL-CA-1

Sample FL-CA-1 exhibits numerous carbonate generations, which have been processed separately (Figure 47a; b; c). Most of the calcite in this sample is orange in color and is intergrown with a white calcite. Smaller veinlets are cut through the orange calcite (referred to as orange calcite veinlet). A clear vein cuts through orange calcite and is itself cut by a small red vein calcite vein. A reddish calcite is located at one spot in the clear vein but is texturally unrelated with the red vein calcite. The white calcite obtained high errors values and is therefore only presented in the appendix.

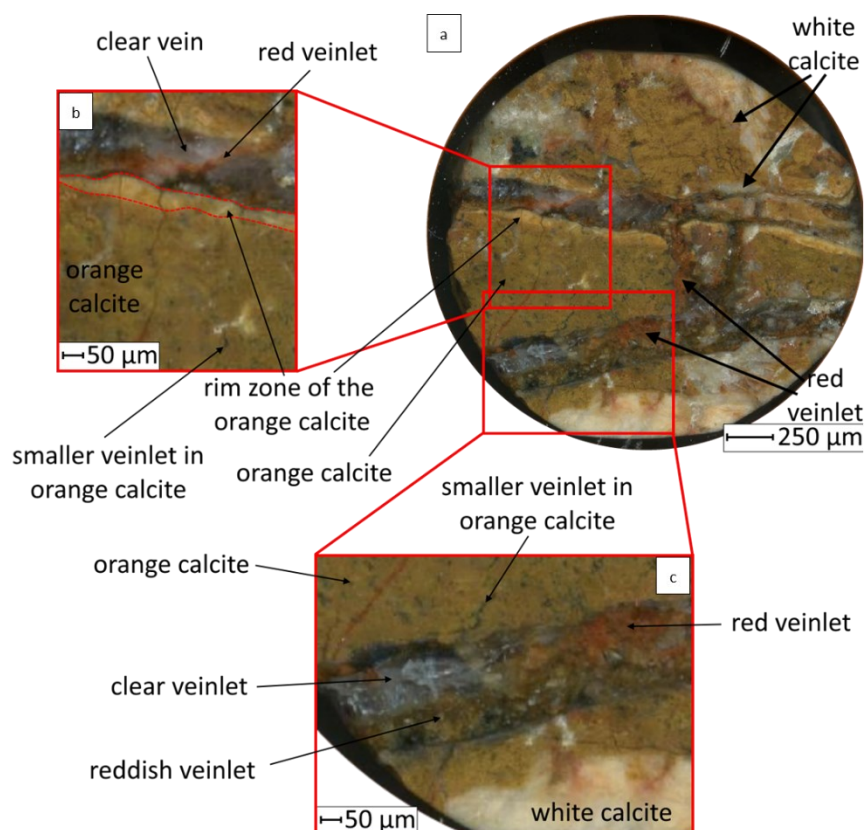


Figure 47: a) Overview of sample FL-CA-1; b) and c) are detailed photos of the different veins.



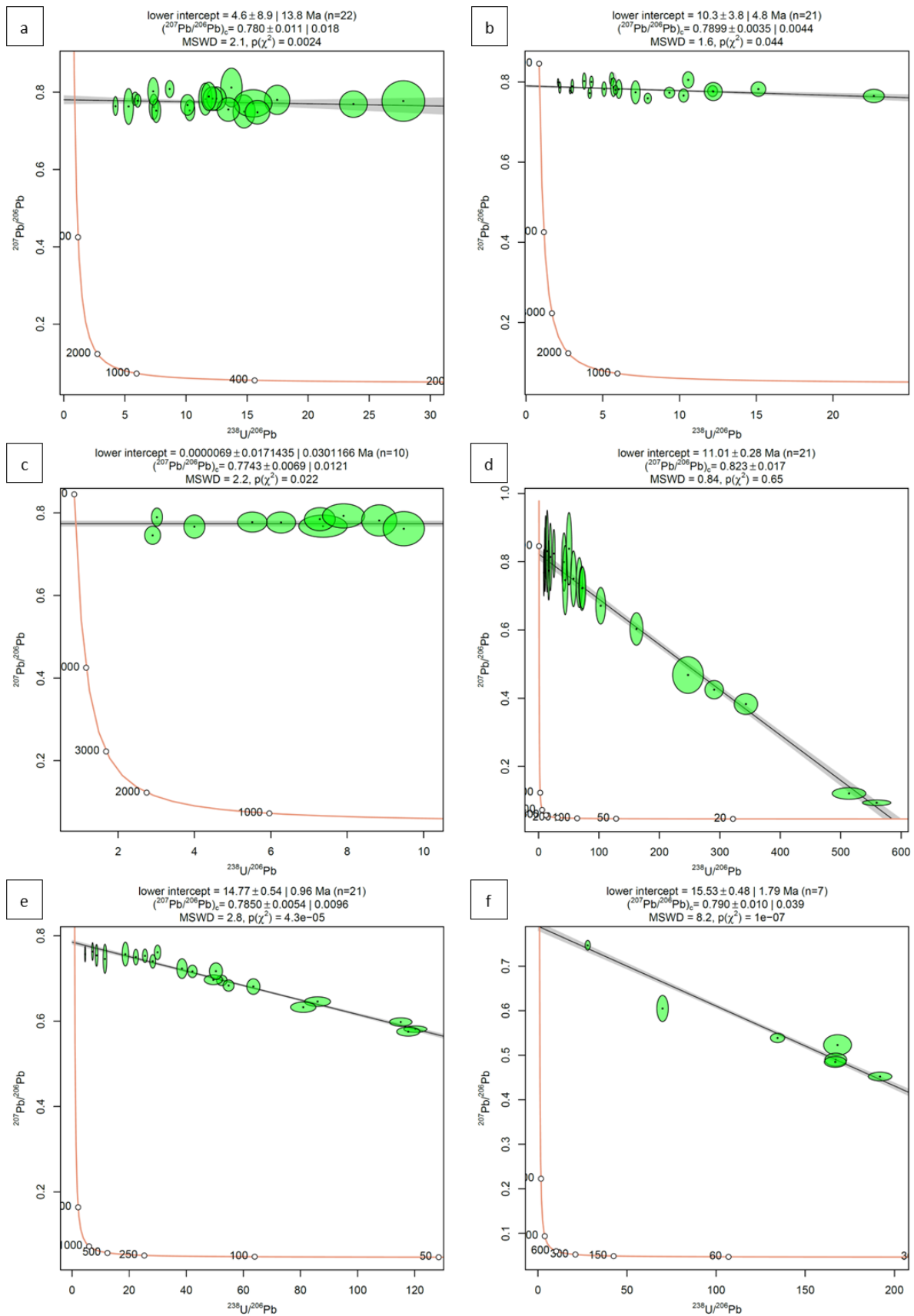


Figure 48: Tera-Wasserburg plots for FL-CA-1, a) shows the orange calcite; b) the rim of the orange calcite; c) shows the age of the small calcite veinlets in the orange calcite, d) is the age of the clear calcite veinlet; e) the red veinlet and f) the reddish veinlet. Compare with Figure 47.

The orange calcite was further sub-divided into a core and rim zone. The core indicates an age of  $4.6 \pm 8.9$  Ma, while the rim gives an age of  $10.3 \pm 7.4$  Ma (Figure 48a; b). Notably, both MSWD values are relatively low. The smaller veinlets in the orange calcite obtained the youngest age of the sample with  $0.000069 \pm 0.171435$  Ma with an MSWD of 2.2 (Figure 48c).

The clear carbonate veinlet suggests an age of  $11.01 \pm 0.28$  Ma, accompanied by an MSWD below. In contrast, the red veinlet situated between these transparent veinlets is dated at  $14.77 \pm 0.54$  Ma, with an MSWD of 2.8. Additionally, the reddish calcite displays an age of  $15.53 \pm 0.48$  Ma, and its MSWD is recorded at 8.2 (Figure 48d; e; f).

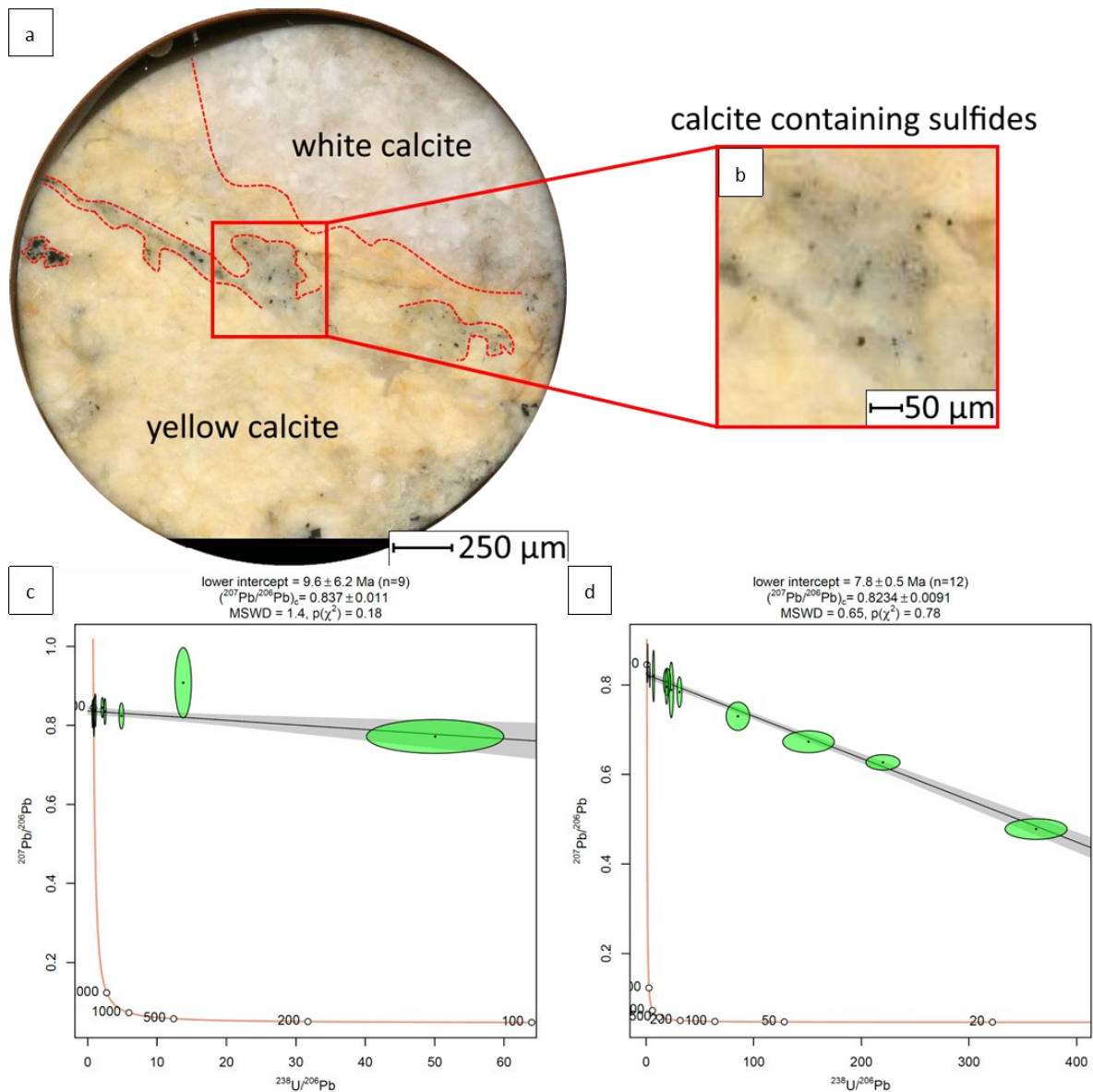


Figure 49: a) Overview picture of sample F441 with Tera-Wasserburg plots for the sample b) yellow calcite 1; c) calcite which contains sulfides. The Tera-Wasserburg plot for the white calcite can be found in the appendix.

### F441

Sample F441 displays three distinct carbonate phases: a whitish, yellowish and sulfidic calcite (Figure 49a; b). The sulfidic carbonate is integrated into the yellowish phase, appearing as a veinlet amidst precipitated sulfidic minerals. Dating the white phase gave insufficient data, due to no U content and can be found in the appendix. The yellow calcite yielded an age of  $9.6 \pm 6.2$  Ma, accompanied by a

relatively low MSWD of 1.4 (Figure 49c). Nevertheless, specific data points display increased uncertainties. The dating of the sulfidic veinlet is reported as  $7.8 \pm 0.5$  Ma, accompanied by a high MSWD of approximately 0.65 (Figure 49d).

#### *FL-AG-1*

Sample FL-AG-1 comprises five different calcite generations that were examined (Figure 50a). One whitish calcite was texturally split into three different sub generations. Co-existing within a yellow calcite and a cluster of red veinlets that intersect the sample and separate the calcite sections from each other.

Results for the white calcite are for phase one  $17.79 \pm 0.68$  Ma, with a high MSDW of 6.7 (Figure 50b). White calcite two of  $30.6 \pm 6.1$  Ma, with an even higher MSWD of 16 (Figure 50c). The third white calcite indicated an age of  $13.55 \pm 0.30$  Ma and a relatively low MSWD of 3.8 (Figure 50d). The MSWD of yellow carbonate phase is 2.7 and indicates an age of  $12.65 \pm 0.39$  Ma (Figure 50e). The red veinlet shows a very high MSWD about 100, with an age of  $52 \pm 1.6$  Ma. The plot can be found in the appendix.

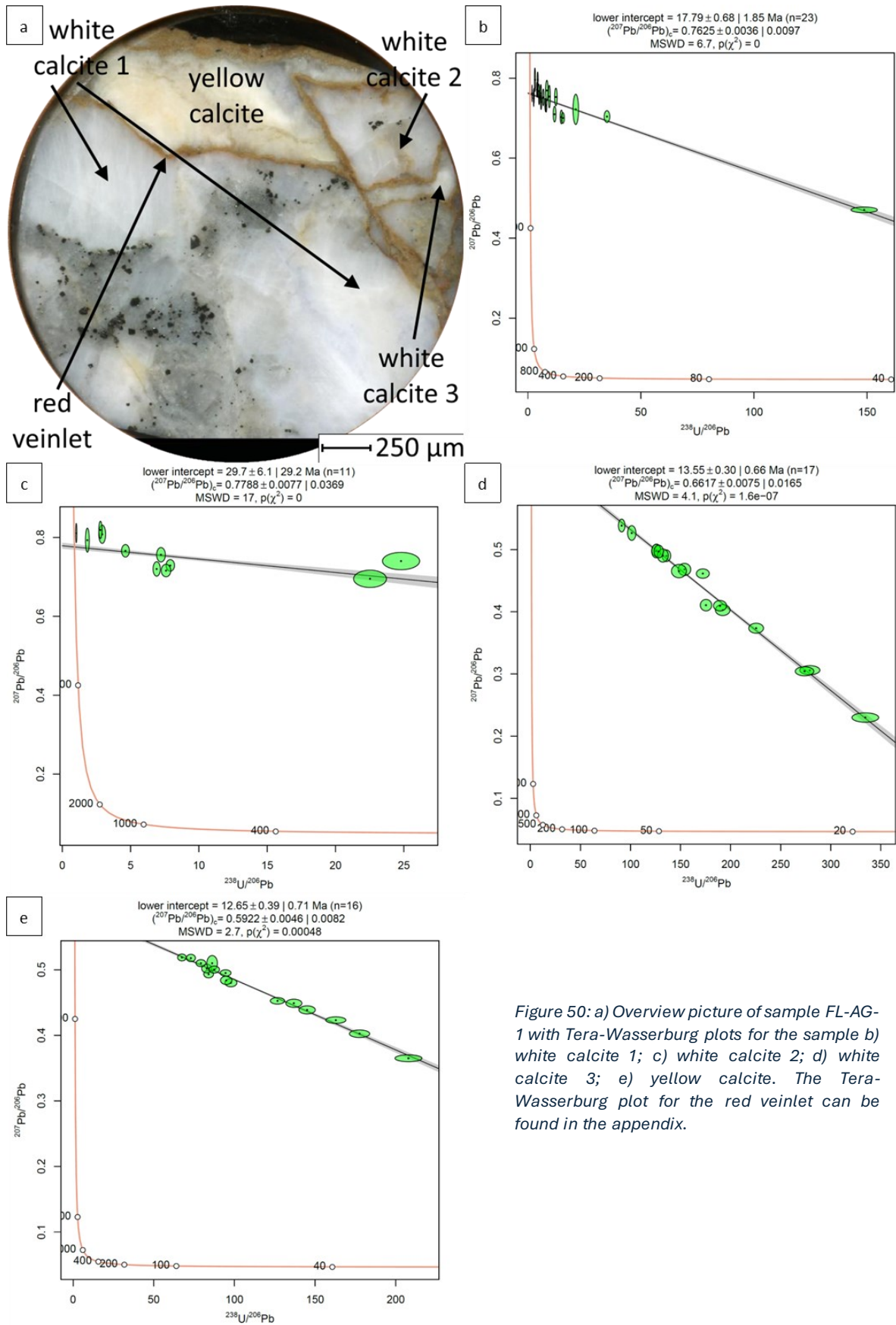


Figure 50: a) Overview picture of sample FL-AG-1 with Tera-Wasserburg plots for the sample b) white calcite 1; c) white calcite 2; d) white calcite 3; e) yellow calcite. The Tera-Wasserburg plot for the red veinlet can be found in the appendix.



Table 14: Summary of the age dates (Straßegg and Flatschach).

Sample ID	Sub category	U/Pb age
22JH11		0.00011±0.56554 Ma
22GS52a		3.90±0.39 Ma
22GS52b		4.2±1.2 Ma
22GS52d	orange calcite	17.4±1.1 Ma
	veinlet	5.08±0.47 Ma
F562		3.5±12 Ma
FL CA 1	orange calcite	4.6±8.9 Ma
	rim of the orange calcite	10.3±7.4 Ma
	smaller veinlets in orange calcite	0.0000069±0.171435 Ma
	clear calcite veinlet	11.01±0.28 Ma
	red veinlet	14.77±0.54
	reddish veinlet	15.53±0.48
F441	white calcite	not sufficient data
	yellow calcite	9.6±6.2 Ma
	calcite containing sulfides	7.8±0.5 Ma
FL AG 1	white calcite 1	17.79±0.68 Ma
	white calcite 2	29.7±6.1 Ma
	white calcite 3	13.55±0.30 Ma
	yellow calcite	12.65±0.39 Ma
	(red veinlet)	(52±1.6 Ma)

### 4.7.3 U/Pb reference material

#### 4.6.3.1 Primary reference material

As primary reference material was WC-1 carbonate ( $254.4 \pm 6.4$  Ma; Roberts et al. 2017) used.

Table 15: Primary reference material WC-1 carbonate in ALL sessions.

Date and run	Uncorrected WC-1 age (Ma)	WC-1 Correction factor
21.11.2022-1	253±3.4	1.01
21.11.2022-2	246.1±3.2	1.03
22.11.2022-1	254±4	1
22.11.2022-2	257±7	0.99
23.11.2022-1	251.8±4.6	1.01
23.11.2022-2	255.7±4.1	0.99
24.11.2022-1	262.4±5.3	0.97
24.11.2022-2	254±7	1

#### 4.6.3.2 Secondary reference material

To test the long-term reproducibility during the session Mudtank zircon ( $732 \pm 5$  Ma; Black, L. P., Gulson B.L., 1978; Jackson *et al.*, 2004) and Duff Brown Limestone ( $64 \pm 2$  Ma; Hill *et al.*, 2016) were used as a secondary reference material. The analyses of Mudtank yielded a concordia age of  $726 \pm 3.7$  Ma which varies 0.82 % from the reported age (Figure 51a). In case of Duffbrown, the age was about  $62.08 \pm 0.45$  Ma, deviating 3 % from the reported age (Figure 51b).

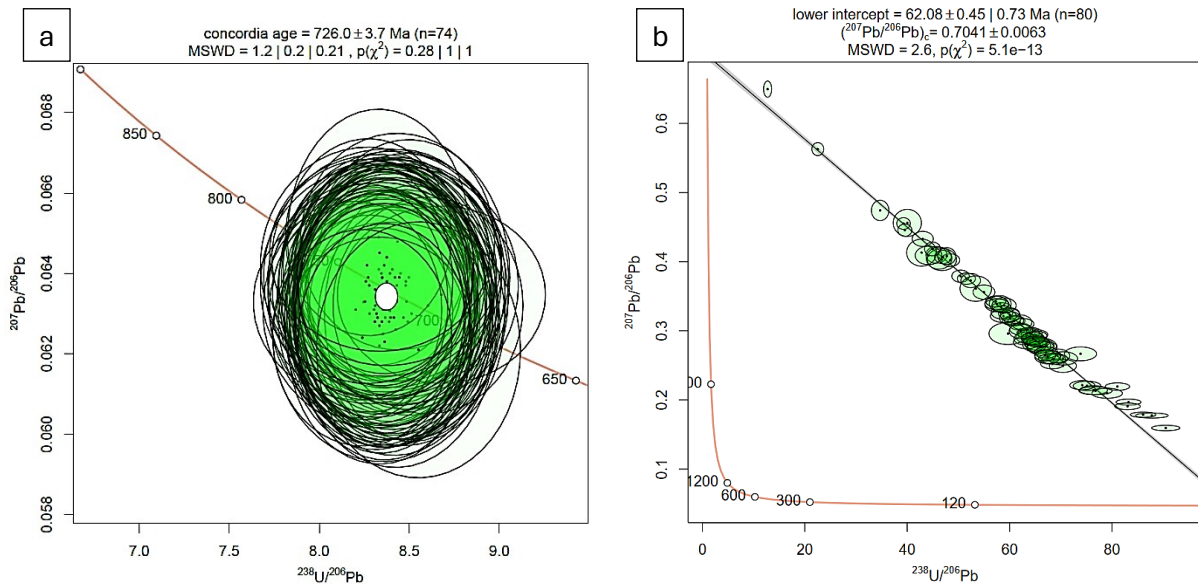


Figure 51: a) Mudtank analyses for ALL analytical sessions; b) Duffbrown analyses for ALL analytical sessions.

## 5 Discussion

### 5.1 Major and trace element geochemistry and microscopy

#### 5.1.1 Element distribution

The plotted ratios of the whole rock geochemistry show correlations between a variety of elements. The highest element content besides Fe and S, appear to be that of As, Sb and Pb (Table 6). Other elements including Ag, Au, Co, Cu, Mn Ni, Rb, V and Zn show comparatively intermediate contents. Variations in correlations of elements with As and Pb show similarities with the previously described evolution of the deposit (Bojar *et al.*, 2001). However, the wide variability in the elements suggests a polyphase evolution of the deposit formation extending beyond the two ore stages originally described.

Arsenic contents exceeded the upper detection limit (>10,000 ppm) of the whole rock analyses in 15 cases. As a result, the correlation of As with other elements is not always readily evident (Table 6). Gold, Ag, Bi, Cu, Pb, and Sb appear to correspond to an elevated As content and may be interpreted as belonging to the main ore mineralization stage. Lead contents show great variability across the samples. Silver and Cu concentrations correlate positively with increased Pb concentrations (Figure 9b; c; d). The appearance of these two elements are therefore more likely related to the later Pb mineralization rather than the gold mineralization, as was previously assumed (Bojar *et al.*, 2001).

Samples 21TB07, 21TB09 and to a lesser degree 22JH02 have significantly elevated transition metal concentrations compared to the other samples (Table 6). While the, for Straßegg, typically high in concentration elements like As and Pb are relatively low in these samples. In contrast, elements like Mn, Ni, Sr, V, W and Zn are elevated in these samples. Sample 21TB07 and 21TB09 have been provided by the AUREX Biomining AG (Table 5) and were sampled from the same locality as samples 21TB05 to 21TB10 (Figure 8) near an abandoned adit. Sample 22JH02 was taken in the vicinity of the other two samples and had come from outcrop in a creek bed (Figure 8). The trace elemental signature of these three samples is distinct to any others collected for this study and seem to contain a mineralization style which has not been previously described in the literature.

#### 5.1.2 Major element zoning in arsenopyrite and implications for substitution mechanisms

The number of elements mapped by EPMA in arsenopyrites were limited to 5 main elements due to the number of WDS spectrometers available. The five most diagnostic elements indicated by the bulk rock chemistry were thus chosen to be analyzed, and only these five will be discussed. The major elemental constituents of arsenopyrite: As, Fe, and S, show significant variations in their distribution. Arsenic and S show a marked anticorrelation in the maps. Small variations in Fe content are also visible and correlate with S. Gold and Pb generally occur in higher concentrations where As is elevated. Silver and Cu are not visibly zoned. These zonation patterns can be seen in the BSE images of the arsenopyrite as well. Arsenopyrite zonations appear to have more geometric patterns, whereas pyrite zonation is patchier (e.g. Figure 20b; Figure 21c;d).

Previous work shows that arsenopyrite is capable of incorporating trace elements in place of Fe, As, and/or S in the crystal lattice structure (Fleet & Mumin, 1997; Sung *et al.*, 2009; Cook *et al.*, 2013; Fougereuse *et al.*, 2016). The arsenopyrite mineral formula (FeAsS) might be more correctly written as

$\text{Fe}^{3+}(\text{AsS})^{3-}$ . In this notation it becomes clear, that  $\text{Fe}^{3+}$  can be substituted by other  $3^+$  cations (Cook & Chryssoulis, 1990). The mapped arsenopyrites from Straßegg show that As, Fe, and S contents are all highly variable, with As and S content varying the most. This suggests that the anion plays the dominant role in the incorporation of trace elements. Cook *et al.* (2013) suggests that multiple  $2^-$  anions (e.g.  $\text{Te}^{2-}$ ,  $\text{Se}^{2-}$ ), can substitute for  $\text{S}^{2-}$ . While there is no appreciable Te or Se present in the Straßegg arsenopyrites, the anticorrelation between As and S seems to suggest that in this case, “excess” As substitutes for  $\text{S}^{2-}$ . This process is directly connected to elevated contents of Au, Pb and Sb. Stepanov *et al.* (2021) describes arsenopyrite as likely to have variable contents of As and S, which results in the mineral formulas of  $\text{Fe}(\text{As,S})_2$  or  $\text{FeAs}(\text{As,S})$ . This does not, however, explain the partly diffuse distribution of Sb in the arsenopyrites. Sample 22JH08a shows, on the right side of the Figure 32, that as the content of S increases, As content decreases and Sb is elevated. In this case, as predicted by the model, it appears that As is substituting for S in the presence of elevated concentrations of antimony, while Fe concentrations remain unchanged. However, this pattern was only observed in approximately half the samples. Equally prevalent was a complete lack of correlation of antimony concentrations with either As or S zonation. Perhaps this diversion from the model is the result of a later more localized overprinting fluid with high antimony concentrations. In any case, it appears that the substitution mechanism in Straßegg arsenopyrites is highly complex and cannot be ascribed to a single process.

The zonation of Ni and Co, which occurs occasionally as oscillatory zoning (Figure 36), anticorrelates with Fe. A similar behavior is described by Tang *et al.* (2019) for Au-bearing arsenopyrite in an orogenic gold deposit, while coeval As and S substitute.

### 5.1.3 Major element zoning in pyrite and implication for substitution mechanisms

Zonation in Straßegg pyrites is highly variable. Larger pyrite crystals occur with a trace element barren core (Figure 26c, Figure 23c), surrounded by a more As rich rim zone. This As rich zone can be subdivided into two subzones, with the first generally lacking Au and the second enriched in Au (Figure 39). The incorporation of Co and Ni forms rim structures, often near the crystal boundaries. In smaller pyrites, As and Au are often distributed throughout the whole crystal. Cobalt and Ni once again form rim structures. This observation is consistent with the literature, wherein the As facilitates the incorporation of Au gold in pyrites (Reich *et al.*, 2005; Deditius *et al.*, 2014; Gopon *et al.*, 2019). These papers suggest that sulfur is substituted by  $\text{As}^{1-}$ , which breaks pair-bonded S atoms and results in a Lewis base (partial charge imbalance) as well as a point defect in the lattice. At the point where  $\sim 200$  As atoms replace S, a full charge ( $1^-$ ) imbalance is created which  $\text{Au}^{1+}$  can balance (Gopon *et al.*, 2019). The more As that replaces sulfur, the more Au can be incorporated into the pyrite crystal structure. This also means that the amount of Au is constrained by As, which can also act to attract Au to the pyrite growth surface (Xie *et al.*, 2024). The mineral formula for gold bearing arsenian pyrite would be  $\text{Fe}(\text{S,As})_2$ , however it should be pointed out that in oxidizing conditions  $\text{As}^{2+}$  substitution for  $\text{Fe}^{2+}$  has been noted (Deditius *et al.*, 2008; Stepanov *et al.*, 2021).

While arsenian pyrite has been shown to be capable of including Ag, Bi, Co, Cu, Hg, Ni, Pb, Se, Sb, Te, Tl, U, W and Zn (Cook & Chryssoulis, 1990; Reich *et al.*, 2005), the Straßegg pyrites exhibit a much more limited number of elements and these emerge during different stages of the deposit formation. For this reason the Cu, Pb or Sb that occurs at Straßegg does not occur as trace elements within pyrite but are rather incorporated in arsenopyrite, Pb-sulfosalts or Pb-sulfide inclusions.



#### 5.1.4 Evolution of the mineralization and genetic model

Combining previous work on Straßegg with the results of this thesis, the evolution of the ore deposit can be explained in greater detail. The identification of several ore stages, which correspond to the addition of specific elements, expands the existing genetic model (Table 2).

Table 16 shows an updated genetic model of the mineralization in Straßegg. The emergence of different elements is depicted, with emphasis on major and minor elements. Figure 54 is divided into the elements that are being added to the system, and the later remobilization of those same elements during late stages and/or metamorphic overprinting. In the following sections the different ore stages are discussed. A paragenetic model regarding the sulfide minerals is shown in Figure 55.

##### 5.1.4.1 Pre-ore stage and ore stage 1

The pre-ore stage is rich in Fe. The pyrite contains in general no trace elements or occasionally a small amount of Ni. In larger pyrite crystals this stage often forms a trace element barren core. This is followed by ore stage 1, which is dominated by As, both in the form of several generations of arsenian pyrite (Py-1, Py-2) as well as arsenopyrite (Apy-1, Apy-2). The emergence of As forms an As and Au rich rim (Py-1) with occasional Ni. This rim contains no evidence of oscillatory zoning. Although it should be mentioned that the large size of the laser spot (5 µm) might be hiding micrometer to sub-micrometer growth zones, as is the case in other deposits that contain a barren pyrite core with arsenic and gold rich overgrowths (Cline *et al.*, 2005; Gopon *et al.*, 2019). In A0982-map 2 the As content has a marked increase and is similarly linked to a delayed increase in Au (Py-1). The Au content fluctuates, but in general it can be said that higher As is linked with higher Au. Such core/rim structures of As/Au (Py-0/Py-1) are not observed in smaller pyrites. These consist mainly of Py-1, with distributed As and Au in the entire core. The content of Au varies in smaller pyrite and is less evenly distributed than As.

After Py-1 grew, the following pyrite generation (Py-2) shows a Co and Ni distribution. In Py-2, Co and Ni form rim like structures, often with Co as the dominant element followed by Ni. The zoning of Py-2 is often geometric and concentric. The supply of the elements seems to have been short lived in the mineralizing fluid, because of the abrupt end of the zonation (Figure 43, Figure 45). In Apy-1, Co and Ni are incorporated in oscillatory growth zones, with a slightly anticorrelation to Fe (see Chapter 5.1.2 *Major element zoning in arsenopyrite and implications for substitution mechanisms*). Some of this submicron zonation are bigger than others, which could be interpreted as short-lived pulse that formed Apy-1. Due to the incorporation of Co and Ni in its structure, arsenopyrite generation Apy-1 emerged in the transition between Py-1 and Py-2.

In general, Apy-1 seems to be often enriched in As, Au, Pb, and partly Sb (Figure 32). The second arsenopyrite generation Apy-2 forms a rim, with a higher content of S and Fe. The Sb zoning is highly variable, partially enriched in Apy-1 (core), and partially forming distinct zones unassociated with other mapped elements. These zones do not fit any of the previously observed zoning patterns and are often spotty or crosscut the other zones. This points to an initial mineralizing fluid that was enriched in Au, Pb and partly Sb (Apy-1). Antimony is suggested to be both part of the fluid that formed Apy-1 as well as an additional fluid and/or was remobilized more readily than other elements. The supply of As, Au and Pb (and Sb) decreased in the second generation of sulfide growth which formed the arsenopyrite (Apy-2), while the contents of S (and Fe) were increased.

The substitution of As for S in the pyrite/arsenopyrite (Py-1, Apy-1) structure leads to the notions of a depleted S-supply during the beginning of ore stage 1 or an over-supply of As. With all methods that were used, an extremely high amount of As in minerals, especially arsenopyrite, was observed. Therefore, an As oversaturated fluid seems more likely since the supply of S is persistent, as is evidenced in the late base metal ore mineralization. The assemblage of arsenopyrite and pyrite is not surprising, in fact it is typical of orogenic and epithermal deposits (Cook *et al.*, 2013). Due to the substitution of Co/Ni for Fe in arsenopyrite a fluctuation in the concentration of Fe can be assumed. The fluctuation of elements in the minerals growing during ore stage 1, suggest a variable conditions of the ore forming fluid, which influences the incorporation of trace elements. Steadman *et al.* (2021) describes temperature and fluid composition as major factors that control trace elements in pyrite. Different elements that are incorporated in the mineral structure indicate different temperatures at which the pyrite was formed. Elements are not restricted to the assigned temperature range; therefore, an element overlap between different temperature ranges is possible. In general, the incorporation of As in pyrite is assigned to an intermediate temperature range of 200 to 300°C (Steadman *et al.*, 2021). In the case of Straßegg, Py-1 and Py-2 might have grown at these temperatures. Bojar *et al.* (2001) determined an arsenopyrite formation temperature between 350 to 400°C, higher than is estimated in this thesis from Py1/2. If we assume that Apy-1 is assigned to this ore stage, the temperature increases during the change in mineralization from pyrite to arsenopyrite. This means that the elevated temperature could enable the incorporation of first As and Au in Py-1, later the formation of Co and Ni in the generation Py-2, which in general is related to temperatures above 300°C (Steadman *et al.*, 2021).

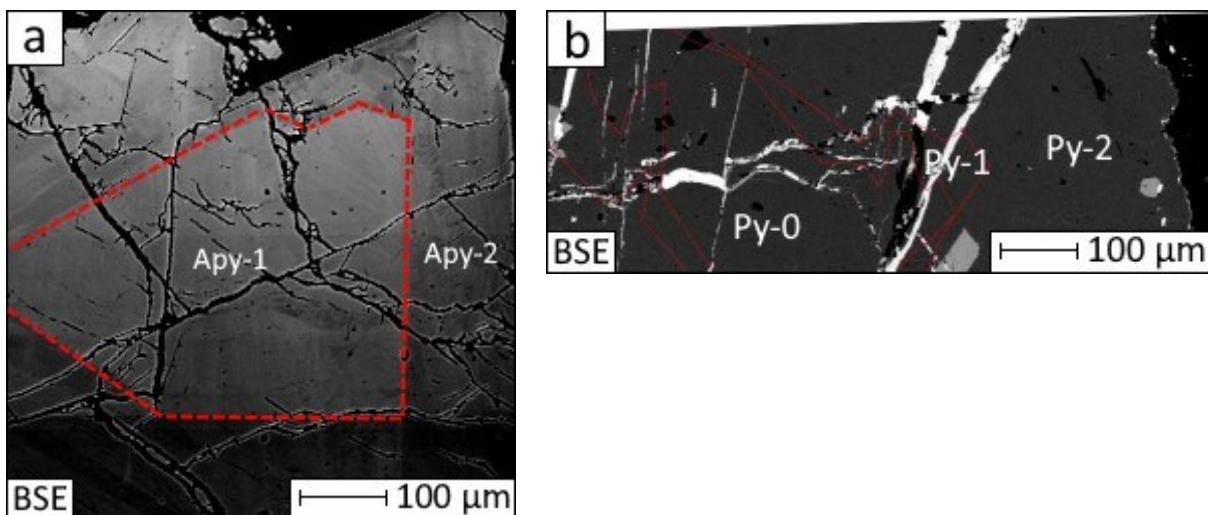


Figure 52: Ore stage generations in arsenopyrite and pyrite; a) BSE image of map 22JH08a (arsenopyrite), indicating the primary Apy-1 and the later stage Apy-2. b) BSE image of map A0982-map 2 (pyrite) shows Py-0 to Py-2.

Ore stage 1 is divided into two sub ore stages (a; b) due to the geochemical and temperature change evidenced by the trace elements in pyrite/arsenopyrite. Py-1 and Apy-1 can be assigned to the ore stage 1a, even if Apy-1 plays more of an intermediate role between the stages. Within increasing temperature first Py-2 and later trace element poorer Apy-2 occurred (Table 16). The ore stages in the minerals can be seen in Figure 52.

Table 16: Suggested ore stages of the mineralization in Straßegg. Beginning with a pre-ore stage which mainly consists of the pyrite generation Py-0. Followed by ore stage 1 which comprises the pyrite generations Py-1, Py-2, and arsenopyrite generation Apy-1 to Apy-2. Ore stage 1 can be subdivided into a and b. Ore stage 2 consists mainly of the occurrence of Cu in three different element assemblages. The first generation of ore stage 2 is Ag-Cu-Zn-1, where the occurrence of chalcopyrite is assigned to, to a probably intermediate stage of Bi-Ga-In-1 and finally Bn-1 with the occurrence of bournonite. This element assemblages marks the beginning transition to ore stage 3, which is dominated by Bou-1, with the main mineral boulangerite, and later Gn-1, which consists of galena. Post-ore mineralization can be assumed El-1, due to the formation of gold nanoparticles in form of electrum. Other remobilizations of elements occur due to the oxidation of arsenopyrite or Pb-phases.

ore stage	sub ore stage	Mineral generation	Main mineral	Mineral formula	Emerging elements
pre-ore stage		Py-0	pyrite	FeS <sub>2</sub>	±Ni
ore stage 1	a	Py-1	pyrite	FeS <sub>2</sub>	As, Au±Ni
	b	Py-2	pyrite	FeS <sub>2</sub>	As, Au, Co, Ni
	a (b)	Apy-1	arsenopyrite	FeAsS	As, Au, Pb ±Sb±Ni±Co = less S, (Fe)
	b	Apy-2	arsenopyrite	FeAsS	S, (Fe) = less As, Au, Pb ±Sb±Ni±Co
ore stage 2		Ag-Cu-Zn-1	chalcopyrite	CuFeS <sub>2</sub>	Ag, Cu, Zn
		Bi-Ga-In-1	?	?	Bi, Ga, In ±Ge ± Mo ±Tl
		Bn-1	bournonite	PbCuSbS <sub>3</sub>	Cu, Pb, Sb
ore stage 3		Bou-1	boulangerite	Pb <sub>5</sub> Sb <sub>4</sub> S <sub>11</sub>	Pb, Sb
		Gn-1	galena	PbS	Pb
post-ore stage remobilization		El-1	electrum	(Au,Ag)	
		As-Fe-O/Pb-O	?	(As-Fe-O) / (Pb-O)	

#### 5.1.4.2 Ore stage 2

After ore stage 1, it appears that Cu, Pb and Sb containing sulfides formed. Boulangerite, bournonite, chalcopyrite and galena do occur in different samples (Table 7) and have been assigned to ore stage 2. Petrographic observations show that bournonite, as a Cu and Sb carrying Pb-sulfide Bn-1 (bournonite = PbCuSbS<sub>3</sub>), is overgrown by boulangerite Bou-1 (boulangerite = Pb<sub>5</sub>Sb<sub>4</sub>S<sub>11</sub>) and finally Gn-1 (galena = PbS). It appears that the trend goes from Cu/Sb containing sulfides in ore stage 2 to Pb dominated sulfides in ore stage 3. Ore stage 2 marks mainly a short intermediate stage of the mineralization between Fe-rich ore stage 1 and Pb-rich ore stage 3. Due to the high concentration of Cu in larger fractures of pyrite and less Cu in smaller fractures, it seems that Cu occurred earlier than the dominating Pb supply. Still, the supply of Pb started slightly already in ore stage 1 as incorporation in Apy-1. In contrast, Cu is not incorporated in arsenopyrite and pyrites of ore stage 1. Instead, with the emergence of Cu in the form of chalcopyrite, with decreasing Fe but increasing Pb and Sb, bournonite formed.

Silver seems to appear coevally with the Cu sulfides. Silver is generally found in fracture filling Pb-sulfide phases or in electrum. Due to the lack of Ag in any zonation of arsenopyrite or pyrite of ore stage 1, it appears that Ag is separate from the As rich fluid / ore stage 1. Zinc correlates with Ag and Cu in the LA-ICP-MS maps, especially in A0982-map 2 (Figure 39). Here Zn is found in fractures within pyrite and must have therefore been part of the emergence of Ag and chalcopyrite (Ag-Cu-Zn-1). LA-ICP-MS spot analyses of chalcopyrite show elevated Ag and Zn, which appears to support the idea that Ag-Cu-Zn-1

belongs to ore stage 2. However, the formation of chalcopyrite seems to be at the beginning of ore stage 2, due to the lack of Fe in fractures, that have been filled with Ag, Cu, and Zn.

The oxidation state of incorporated elements in chalcopyrite ranges from 1+ to 4+ (George *et al.*, 2016). Torr o *et al.* (2022) proposed Ag, Cd, Ga, Ge, In, Se, Sn and Zn are latticed bound in chalcopyrite, while Au, Bi, Mo, Pb, Sb and Tl are suspected to be inclusions. After deleting suspected inclusions in the data of the chalcopyrite spot analyses, minor components that are remaining in the chalcopyrite are As, Cd, Ga, Ge, Ni, Hg, In, Pb, Sb, Sn and Tl. The emergence of As could be related to oxidizing As-Fe-O phases, which occur in several polished mounts.

Next to the chalcopyrite spot analyses LA-ICP-MS mapping revealed a large range of trace elements, which occur in the fractures or inclusions of pyrite. Bismuth, Ga and In and occasionally Ge, Mo and Tl (Bi-Ga-In-1) can be also found in the chalcopyrite and are related to the first occurrence of a Pb rich phase. This likely occurred before or at least during the occurrence of Ag-Cu-Zn-1 and is therefore part of ore stage 2. Support for this assumption is the distribution of elements in the fractures and inclusions in pyrites. In comparison to Ag-Cu-Zn-1, Bi-Ga-In-1 is in lesser amounts in fractures and inclusion, with minor variations.

By decreasing Cu content and increasing Pb and Sb, bournonite (Bn-1) formed, initiating the transition between ore stage 2 and 3. Bournonite is not very abundant and supports the assumption that the supply of Cu is not long-living. Lead and Sb content is already present in Apy-1 but reaches its highest concentration in the later ore stages, beginning with the end of ore stage 2.

#### 5.1.4.2.1 Cd:Zn ratio in chalcopyrite

The ratio of Cd:Zn in chalcopyrite and sphalerite can be used as a geothermometer (George *et al.*, 2018; Duran *et al.*, 2019). The whole rock geochemical analyses Cd, Cu and Zn (Table 6, Figure 12d) do not show any correlation, but Cd and Zn are found in appreciable concentrations in chalcopyrite to make use of this thermometer (Table 12).

The amount of Cd:Zn in minerals is controlled by temperature, sulfur activity and pH value of the ore forming fluid. In case of chalcopyrite the incorporation of elements is as well depending on the co-crystallization of sphalerite, which was not found in the samples of Stra egg (George *et al.*, 2018; Duran *et al.*, 2019). It can be assumed that the formation of chalcopyrite and therefore probably ore stage Ag-Cu-Zn-1 (Table 16) as well, occurred in still relatively hot conditions, unrelated to the formation temperature obtained from arsenopyrite.

Table 17: Chalcopyrite spot analysis results of the elements Cd and Zn. Measurements suspected as inclusions have been avoided. The ratio between both elements can be found on the right side.

Cd [ppm]	Zn [ppm]	Cd:Zn
15.23	649.67	0.023
14.02	503.38	0.028
13.39	504.59	0.027
8.46	465.3	0.018
9.03	500.18	0.018
11.56	521.02	0.022
12.53	442.43	0.028
5.95	461.73	0.013
8.82	423.18	0.021



The amount of Cd is relatively low compared to Zn and implies a low formation temperature for the deposit in Straßegg (<400°C). However, entering the Cd:Zn ratios of Table 17 into a plot after Duran *et al.* (2019), the result fit with skarn or metamorphosed low temperature deposits (Figure 53). Bojar *et al.* (2001), in contrast places the formation temperature between 450 to 350°C. The temperature of crystallization is not the single factor that influences the incorporation of Cd and Zn in chalcopyrite, and the metamorphic overprinting has a large effect. This leads to a seemingly contradictory interpretation of our data, which on the one hand shows low Cd/Zn ratios which implies low temperature if the deposit is metamorphosed but high temperatures if not.

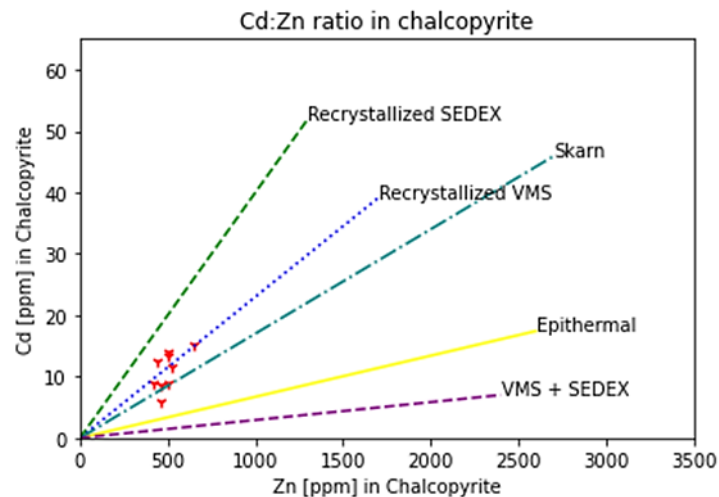


Figure 53: Cd:Zn ratio ( $n=9$ ) of the results of the chalcopyrite in-situ spot analyses, correlated to the Cd:Zn ratios assigned to different types of deposits (after Duran *et al.*, 2019, George *et al.*, 2016).

#### 5.1.4.3 Ore stage 3

Lead appears to be long lived in the mineralization at Straßegg, but with fluctuating intensity. The first example of Pb occurs as a trace element Apy-1 (Figure 32), and the last occurrence in chalcopyrite (Table 12). Maximum Pb concentrations are likely reached during the formation of bournonite (Bn-1), boulangerite (Bou-1) and galena (Gn-1). Lead containing mineral inclusions are ubiquitous in all samples and most sulfide minerals and are found in fractures and as alteration rims of Pb-oxide.

Ore stage 3 begins with the formation of Boulangerite (Bou-1) and with the decreasing Sb content galena (Gn-1) was formed at last. This description fits with the determined mineralization sequence by Bojar *et al.* (2001).

#### 5.1.4.4 Post-ore stage remobilization

After the main mineralization in Straßegg occurred, a remobilization of the elements can be observed (example Figure 26a; b; Figure 27a). This includes inclusions or alteration zones which are formed at a time after ore stage 3. Gold often occurs, together with Ag, in the form of electrum in the Straßegg arsenopyrite and pyrite in inclusions and fractures. The question that this thesis seeks to answer is whether these inclusions are primary mineralization features or secondary enrichment processes during metamorphic overprinting and/or deformation (Dubosq *et al.*, 2019; Fougrouse *et al.*, 2024). Such enrichment processes have been described in orogenic gold deposits overprinted at greenschist

facies conditions (Cook *et al.*, 2013). In comparison to the literature, arsenopyrite in Straßegg shows less enrichment of Au and Ag in the rims of crystals, and instead it is the cores that are enriched in Au (Cook *et al.*, 2013). Silver was not detected as a trace element in arsenopyrite (nor pyrite) and was therefore assigned to ore stage 2 (Ag-Cu-Zn-1) rather than ore stage 1.

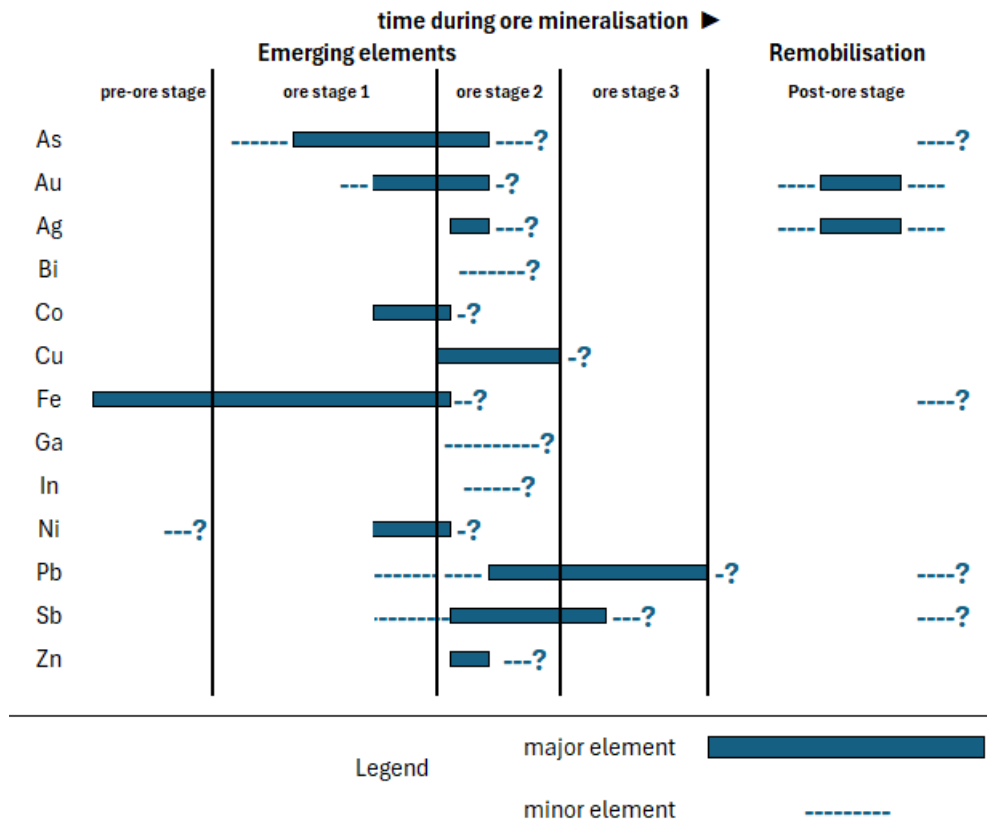


Figure 54: Genetic table of the elements that have been observed. Suggestions are following the occurrence of elements in the EPMA and LA-ICP-MS.

Lattice-bound elements, like As and Au, could be mobilized during orogenic deformation. Fougereuse *et al.* (2024) describes nano-scale structures in pyrite, which vary between trace-element rich and poor structures as possible feature for redistribution of elements. Regarding the map of sample 22JH31a, the pyrite pure core likely consists of an ordered mineral structure, while the rim crystal lattice is likely distorted crystal lattice by the incorporation of As. Dislocations might mediate interfacial re-equilibration can remobilize Au (Fougereuse *et al.*, 2024). Remobilization of Pb with followed accumulation can be observed in the As-Fe-O of arsenopyrite (Figure 29c), which make an post-ore stage remobilization plausible.

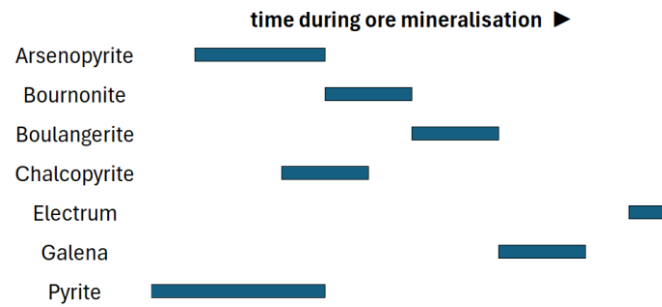


Figure 55: Genetic table of the minerals that have been observed in Straßegg (Table 7) with additional emergence of electrum which is probably related to remobilization processes.

Remobilization that was associated with oxide phases is likely related to meteoric water interacting with the samples once they are in the mine waste, as most of the samples have been exposed for centuries. Remobilized As and Sb, which both are recognized as toxic (Jamieson, 2014; Patel *et al.*, 2023), can be found in oxide phases or in fractures of the gangue mineral imply a problematic distribution of these elements that end up in the soil and ground water (Tessema *et al.*, 2011). The historic processing methods of the sulfide ore lead to a drastic release of As and Sb which contaminates the area to this day. Former Au-mining systems, especially when associated with arsenopyrite, causes a variety of issues in the ore processing and the later storage in tailing piles (Tessema *et al.*, 2011; Wen *et al.*, 2022). The roasting of arsenopyrite, which was the standard process at Straßegg, produces  $As_2O_3$  which is more bio accessible than in its sulfide form. Thus, As is found in significant concentrations in the groundwater and in the soil (Tessema *et al.*, 2011; Jamieson, 2014). In the case of Straßegg, the mine was already closed due to unsafe ore processing causing diseases and death (Bojar, 1989).

## 5.2 Age dating

U/Pb age dating of vein calcite at the University of Portsmouth showed several results. In the case of Straßegg, most samples showed high concentrations of common Pb and highly variable U contents to the point that no useful data was obtained. From Straßegg, sample 22JH11a is the only one that generated any result, but the age obtained ( $0.00011 \pm 0.56554$  Ma) is far from useful in constraining the mineralization. The age is much younger than the reported age of 145 Ma by Antes (1998), nor does it fit in the Late Cretaceous, where Bojar *et al.* (2001) assigned the ore mineralization to.  $Pb^{2+}$  and  $Ca^{2+}$  can be substituted in calcite for each other (Roberts *et al.*, 2020), so it is likely that within the vein formation in Straßegg, ore stage two affected the Pb incorporation in calcite. Additionally, the calcite veins dated were not directly connected with any ore mineralization. Therefore, it is likely that the age resulted from a much younger calcite generation unrelated to mineralization.

Regarding the results of Flatschach, the calcite veins can be subdivided into different generations, which are also noticeable in the optical microscope. Cal-1 gives an age of  $29.7 \pm 6.1$  Ma, so Oligocene in age. Cal-1 occurs in sample FL-AG-1, which was taken in the Urbani-Unterbau adit (northern portion of the mining district). This north-west portion is described to be predominated by chalcopyrite, rather than the southern-east part with arsenopyrite and pyrite (Raith *et al.*, 2015). The geochemical distinct sulfide minerals could be related to different stages of vein formation.

Table 18: Age results of Flatschach subdivided into 3 groups according to their age. Age range comes from U/Pb dating of this thesis.

	Geologic epoch	Age range
Cal-1	Oligocene	$\sim 29.7 \pm 6.1$ Ma
Cal-2	Miocene	$17.4 \pm 1.1 - 7.8 \pm 0.5$ Ma
Cal-3	Pliocene	$3.5 \pm 12 - 5.08 \pm 0.47$ Ma

A younger calcite generation (Cal-2) gives Miocene ages between  $17.4 \pm 1.1$  Ma and  $7.8 \pm 0.5$  Ma. These occur in different stages and crosscutting relationships in the samples and therefore represent different stages of Miocene fluid activity (for example F441).

Cal-3 comprises calcite of Pliocene age, between  $5.08 \pm 0.47$  and  $3.5 \pm 12$  Ma. This calcite generation is especially dominant in samples taken in the Fuchs 1 adit, which also contains generations of Cal-3 which crosscut Cal-2. In other samples (F562, FL Ca 1) the ages of Cal-3 are more variable and with larger uncertainties. For example, the core of the orange calcite ( $4.6 \pm 8.9$  Ma) gives a younger age than the rim ( $10.3 \pm 7.4$  Ma). An explanation for this difference could be the concentration of U, which Roberts *et al.* (2020) described as tending to concentrate at rims or cleavage zones and/or the large uncertainties of the ages themselves. Veinlets which appear to intersect the orange calcite and its rim are from Cal-2 but give a slightly older age ( $11.01 \pm 0.28$  Ma,  $14.74 \pm 0.53$  Ma,  $15.60 \pm 0.43$  Ma see Table 14). These calcites have less uncertainties and the ages are better constrained. The youngest age is  $0.0000069 \pm 0.171435$  Ma which is  $\pm$  modern but with a high uncertainty.

The different generations of calcite (Cal-1, Cal-2 and Cal-3) give a window into the tectonic evolution of Flatschach. Either two generations crosscut each other or in one generation several calcites intersect each other. Calcite is often associated as syn-kinematic precipitation filling in opening fractures (Roberts & Holdsworth, 2022), so one can assume ongoing tectonics in the area of Flatschach between the Oligocene and Pliocene.



Previous research dated the ore mineralization as pre-Miocene due to the mineralization not appearing to crosscut the overlying sediments. This observation comes to us from work one in the 1950s in a mine adit (Fortuna-Unterbau in the south of the mining district) which is not accessible anymore (Raith *et al.*, 2015). Cal-1 would fit with this observation, while Cal-2 and Cal-3 occurred much later. If we assume that the ore deposit must be pre-Miocene the only feasible age, we obtained would place the mineralization at ~30 Ma, although the calcites associated with sulfides are Pliocene age. The adjacent Flatschach tuff, part of the filling of the Fohnsdorf (pull-apart) basin, was dated  $14 \pm 0,6$  Ma (Ingering Fm.) (Sachsenhofer *et al.*, 2000; Strauss *et al.*, 2001; Strauss *et al.*, 2003), and would therefore match with the ages of Cal-2. This indicates complex tectonics setting which are plausible to result in several generations of calcite fluids.

## 6 Conclusion

The Au-As-Ag deposit of Straßegg has been shown to contain precious metals and CRMs. These elements are found as trace elements within arsenopyrite, chalcopyrite and pyrite. Depending on the sulfide mineral, different elements are incorporated in the mineral structure or as inclusions. Pyrite is occasionally a host for As, Au, Ni and Co, which is accommodated by As incorporation which in turn distorts the mineral structure. Arsenopyrite mainly contains Au, Co, Ni, Sb and Pb. In this arsenopyrite As seems to be substituting for S leading to a similar substitution mechanisms to pyrite which appears to allow Au (and potentially Sb and Pb) to be incorporated. Chalcopyrite contains inclusions rich in Ag and Zn; minor amounts of As, Cd, In, Pb and Sn; and trace amounts of Ga, Ge, Hg, Ni and Tl.

Elements that occur in the later base metal dominated ore stage give hints of different geochemical changes in the deposit evolution. In total 7 different ore minerals have been identified, which partly overlap which each other in the ore stages. The updated genetic model that is shown in this thesis states that the mineralization started with pyrite, which is mostly free from trace elements. This was followed by addition of an As rich fluid, which is evidenced by the growth of arsenian pyrite and arsenopyrite. Within an increasing As supply in the fluid, the formation of base metal mineralization started. Coeval with the of chalcopyrite and various sulfosalts (boulangerite, bournonite and galena), fractures in arsenopyrites and pyrites have been filled with Pb-sulfide phases which contain Pb, Ag, Cu, and Sb. Galena is the last ore mineral that was formed during the “main” mineralization process. It appears that later remobilization then leached Ag and Au to form inclusions of electrum in arsenopyrite and pyrite.

Age dating of Straßegg was not successful, but the samples from a neighboring deposit (Flatschach) showed promising results. Most samples varied with ages between  $3.5 \pm 12$  and  $29.7 \pm 6.1$  Ma, showing younger ages than are thought to be feasible for the ore formation (Raith *et al.*, 2015). Samples revealed multiple carbonate phases with different optical properties and ages which cross-cut each other. The calcite generations are highly complicated in this area and warrant further, more detailed, dating which might elucidate the ore forming process in more detail as well as the tectonic evolution of the Eastern Alps.

## References

- Antes, G. 1998. Geochemische und geophysikalische Anomalien im Bereich des Arsenkies-Goldvorkommens Strassegg, Steiermark (Die Strasseger Anomalie"). Unveröff. Diss., Formal- und Naturwisse. Fak. Univ. Wien, Wien.
- Black, L. P., Gulson B.L. 1978. *The age of the mud tank carbonatite, strangways range, northern territory*. pascal-francis.inist.fr/vibad/index.php?action=getrecorddetail&idt=pascalgeodebrgm7920121891.
- Bojar, H.P. 1989. Zur Geschichte der Bergbaue am Straßegg.
- Bojar, H.-P., Bojar, A.-V., Mogessie, A., Fritz, H. & Thalhammer, O. 2001. Evolution of veins and sub-economic ore at Strassegg, Paleozoic of Graz, Eastern Alps, Austria: evidence for local fluid transport during metamorphism. *Chemical Geology*, **175**, 757–777, [http://doi.org/10.1016/S0009-2541\(00\)00342-9](http://doi.org/10.1016/S0009-2541(00)00342-9).
- Bojar, H.-P., Mogessie, A. & Thalhammer, O. 1994. Die Arsenkies-Goldvererzung am Straßegg, Steiermark.- Mitt. Österr. Min. Ges., 139, (MinPet 94, Eggenburg), S. 277-278, Wien.
- Bojar, H.-P., Mogessie, A., Thalhammer, O. & Bojar, A.-V. 1998. Mineralogie, Sauerstoff- und Schwefelisotopen der Elektrum-Arsenopyrit Vererzung am Strassegg, Breitenau am Hochlantsch/Gasen, Steiermark, Österreich.- Mitt. Österr. Min. Ges., 143, S. 254-255, Wien.
- Cline, J.S., Hofstra, A.H., Muntean, J.L., Tosdal, R.M. & Hickey, K.A. 2005. Carlin-Type Gold Deposits in Nevada Critical Geologic Characteristics and Viable Models. In: Hedenquist, J.W., Thompson, J.F.H., Goldfarb, R.J. & Richards, J.P. (eds) *Economic geology: One hundredth anniversary volume*. Society of Economic Geology, Ottawa.
- Cook, N.J. & Chryssoulis, S.L. 1990. Concentrations of invisible gold in the common sulfides. *Canadian Mineralogist*, **1990**, 1–16.
- Cook, N.J., Ciobanu, C.L., Meria, D., Silcock, D. & Wade, B. 2013. Arsenopyrite-Pyrite Association in an Orogenic Gold Ore: Tracing Mineralization History from Textures and Trace Elements. *Economic Geology*, **108**, 1273–1283, <http://doi.org/10.2113/econgeo.108.6.1273>.
- Crameri, F. 2018. *Scientific colour maps*. Zenodo.
- Deditius, A.P., Reich, M., Kesler, S.E., Utsunomiya, S., Chryssoulis, S.L., Walshe, J. & Ewing, R.C. 2014. The coupled geochemistry of Au and As in pyrite from hydrothermal ore deposits. *Geochimica et Cosmochimica Acta*, **140**, 644–670, <http://doi.org/10.1016/j.gca.2014.05.045>.
- Deditius, A.P., Utsunomiya, S., Renock, D., Ewing, R.C., Ramana, C.V., Becker, U. & Kesler, S.E. 2008. A proposed new type of arsenian pyrite: Composition, nanostructure and geological significance. *Geochimica et Cosmochimica Acta*, **72**, 2919–2933, <http://doi.org/10.1016/j.gca.2008.03.014>.
- Dubosq, R., Rogowitz, A., Schweinar, K., Gault, B. & Schneider, D.A. 2019. A 2D and 3D nanostructural study of naturally deformed pyrite: assessing the links between trace element mobility and defect structures. *Contributions to Mineralogy and Petrology*, **174**, 1–16, <http://doi.org/10.1007/s00410-019-1611-5>.
- Duran, C.J. & Dubé-Loubert, H. *et al.* 2019. Applications of trace element chemistry of pyrite and chalcopyrite in glacial sediments to mineral exploration targeting: Example from the Churchill Province, northern Quebec, Canada. *Journal of Geochemical Exploration*, **196**, 105–130, <http://doi.org/10.1016/j.gexplo.2018.10.006>.
- Ebner, F., Fritz, H. & Hubmann, B. 2001. Das Grazer Paläozoikum: Ein Überblick.
- Fleet, M.E. & Mumin, A.H. 1997. Gold-bearing arsenian pyrite and marcasite and arsenopyrite from Carlin Trend gold deposits and laboratory synthesis. *American Mineralogist*, 182–193.
- Flügel, H.W. & Hubmann, B. 2000. Das Paläozoikum von Graz: Stratigraphie und Bibliographie. - Schriftenreihe der Erdwissenschaftlichen Kommission 13, **2000**, 118 pp.

- Fougerouse, D. & Reddy, S.M. *et al.* 2024. Dislocation-mediated interfacial re-equilibration of pyrite: An alternative model to interface-coupled dissolution-precipitation and gold remobilisation. *Geochimica et Cosmochimica Acta*, **374**, 136–145, <http://doi.org/10.1016/j.gca.2024.04.027>.
- Fougerouse, D., Reddy, S.M., Saxey, D.W., Rickard, W.D., van Riessen, A. & Micklethwaite, S. 2016. Nanoscale gold clusters in arsenopyrite controlled by growth rate not concentration: Evidence from atom probe microscopy. *American Mineralogist*, **101**, 1916–1919, <http://doi.org/10.2138/am-2016-5781CCBYNCND>.
- Friedrich, O.M. 1933. *Beiträge zur Kenntnis steirischer Erzvorkommen. 1 Teil.- o. V., 10 S., o. O.*
- Gasser, D., Gusterhuber, J., Krische, O., Pühr, B. & Stüwe, K. 2009. *Geology of Styria: an overview*.
- Gasser, D., Stüwe, K. & Fritz, H. 2010. Internal structural geometry of the Paleozoic of Graz. *International Journal of Earth Sciences*, **99**, 1067–1081, <http://doi.org/10.1007/s00531-009-0446-0>.
- George, L.L., Cook, N.J. & Ciobanu, C.L. 2016. Partitioning of trace elements in co-crystallized sphalerite–galena–chalcopyrite hydrothermal ores. *Ore Geology Reviews*, **77**, 97–116, <http://doi.org/10.1016/j.oregeorev.2016.02.009>.
- George, L.L., Cook, N.J., Crowe, B.B.P. & Ciobanu, C.L. 2018. Trace elements in hydrothermal chalcopyrite. *Mineralogical Magazine*, **82**, 59–88, <http://doi.org/10.1180/minmag.2017.081.021>.
- Gopon, P., Douglas, J.O., Auger, M.A., Hansen, L., Wade, J., Cline, J.S., Robb, L.J. & Moody, M.P. 2019. A Nanoscale Investigation of Carlin-Type Gold Deposits: An Atom-Scale Elemental and Isotopic Perspective. *Economic Geology*, **114**, 1123–1133, <http://doi.org/10.5382/econgeo.4676>.
- Hill, C.A., Polyak, V.J., Asmerom, Y. & P. Provencio, P. 2016. Constraints on a Late Cretaceous uplift, denudation, and incision of the Grand Canyon region, southwestern Colorado Plateau, USA, from U-Pb dating of lacustrine limestone. *Tectonics*, **35**, 896–906, <http://doi.org/10.1002/2016TC004166>.
- Jackson, S.E., Pearson, N.J., Griffin, W.L. & Belousova, E.A. 2004. The application of laser ablation-inductively coupled plasma-mass spectrometry to in situ U–Pb zircon geochronology. *Chemical Geology*, **211**, 47–69, <http://doi.org/10.1016/j.chemgeo.2004.06.017>.
- Jamieson, H.E. 2014. The Legacy of Arsenic Contamination from Mining and Processing Refractory Gold Ore at Giant Mine, Yellowknife, Northwest Territories, Canada. *Reviews in Mineralogy and Geochemistry*, **79**, 533–551, <http://doi.org/10.2138/rmg.2014.79.12>.
- Krenn, K., Fritz, H., Mogessie, A. & Schaflechner, J. 2008. Late Cretaceous exhumation history of an extensional extruding wedge (Graz Paleozoic Nappe Complex, Austria). *International Journal of Earth Sciences*, **97**, 1331–1352, <http://doi.org/10.1007/s00531-007-0221-z>.
- Mathieux, F., Ardente, F., Bobba, S., Nuss, P., Blengini, G., Alves Dias, P. & Blagoeva, D. 2017. *Critical raw materials and the circular economy: – Background report. JRC Science-for-policy report, EUR 28832 EN, Publications Office of the European Union, Luxembourg*.
- Mavrogonatos, C., Voudouris, P., Zaccarini, F., Klemme, S., Berndt, J., Tarantola, A., Melfos, V. & Spry, P. 2020. Multi-Stage Introduction of Precious and Critical Metals in Pyrite: A Case Study from the Konos Hill and Pagoni Rachi Porphyry/Epithermal Prospects, NE Greece. *Minerals*, **10**, 784, <http://doi.org/10.3390/min10090784>.
- MINEREX. 1987. Statusbericht Projekt: Gold - Strassegg. Berichtszeitraum VII - XII / 1986.- Unveröff. Ber. (Lagerst. Arch. Geol. B.-A.), 13 S., Wien, **1987**.
- Modl, D., Grundmann, G. & Bojar, H.-P. 2022. D. Modl – G. Grundmann – H.-P. Bojar, Der Arsenbergbau Zuckenhut/Straßegg (Breitenau/Gasen, Steiermark, Österreich)–Archäologische und mineralogische Untersuchungen zur Herstellung von künstlichen Arsensulfiden, *res montanarum* **62**, 2022, 107–123.
- Neubauer, F., Dallmeyer, R.D., Dunkl, I. & Schirnik, D. 1995. Late Cretaceous exhumation of the metamorphic Gleinalm dome, Eastern Alps: kinematics, cooling history and sedimentary response



- in a sinistral wrench corridor. *Tectonophysics*, **242**, 79–98, [http://doi.org/10.1016/0040-1951\(94\)00154-2](http://doi.org/10.1016/0040-1951(94)00154-2).
- Onuk, P., Melcher, F., Mertz-Kraus, R., Gäbler, H.-E. & Goldmann, S. 2017. Development of a Matrix-Matched Sphalerite Reference Material (MUL -ZnS-1) for Calibration of In Situ Trace Element Measurements by Laser Ablation-Inductively Coupled Plasma-Mass Spectrometry. *Geostandards and Geoanalytical Research*, **41**, 263–272, <http://doi.org/10.1111/ggr.12154>.
- Patel, K.S., Pandey, P.K., Martín-Ramos, P., Corns, W.T., Varol, S., Bhattacharya, P. & Zhu, Y. 2023. A review on arsenic in the environment: contamination, mobility, sources, and exposure. *RSC advances*, **13**, 8803–8821, <http://doi.org/10.1039/d3ra00789h>.
- Paton, C., Hellstrom, J., Paul, B., Woodhead, J. & Hergt, J. 2011. Lolite: Freeware for the visualisation and processing of mass spectrometric data. *Journal of Analytical Atomic Spectrometry*, **26**, 2508, <http://doi.org/10.1039/C1JA10172B>.
- Raith, J.G., Leitner, T. & Paar, W.H. 2015. Orogenic-type copper-gold-arsenic-(bismuth) mineralization at Flatschach (Eastern Alps), Austria. *Mineralogy and Petrology*, **109**, 531–553, <http://doi.org/10.1007/s00710-015-0391-5>.
- Rantitsch, G., Sachsenhofer, R.F., Hasenhüttl, C., Russegger, B. & Rainer, T. 2005. Thermal evolution of an extensional detachment as constrained by organic metamorphic data and thermal modeling: Graz Paleozoic Nappe Complex (Eastern Alps). *Tectonophysics*, **411**, 57–72, <http://doi.org/10.1016/j.tecto.2005.08.022>.
- Reich, M., Kesler, S.E., Utsunomiya, S., Palenik, C.S., Chryssoulis, S.L. & Ewing, R.C. 2005. Solubility of gold in arsenian pyrite. *Geochimica et Cosmochimica Acta*, **69**, 2781–2796, <http://doi.org/10.1016/j.gca.2005.01.011>.
- Roberts, N.M. & Holdsworth, R.E. 2022. Timescales of faulting through calcite geochronology: A review. *Journal of Structural Geology*, **158**, 104578, <http://doi.org/10.1016/j.jsg.2022.104578>.
- Roberts, N.M.W. & Drost, K. *et al.* 2020. Laser ablation inductively coupled plasma mass spectrometry (LA-ICP-MS) U–Pb carbonate geochronology: strategies, progress, and limitations. *Geochronology*, **2**, 33–61, <http://doi.org/10.5194/gchron-2-33-2020>.
- Roberts, N.M.W., Rasbury, E.T., Parrish, R.R., Smith, C.J., Horstwood, M.S.A. & Condon, D.J. 2017. A calcite reference material for LA-ICP-MS U-Pb geochronology. *Geochemistry, Geophysics, Geosystems*, **18**, 2807–2814, <http://doi.org/10.1002/2016GC006784>.
- Sachsenhofer, R.F., Kogler, A., Polesny, H., Strauss, P. & Wagreich, M. 2000. The Neogene Fohnsdorf Basin: basin formation and basin inversion during lateral extrusion in the Eastern Alps (Austria). *International Journal of Earth Sciences*, **89**, 415–430, <http://doi.org/10.1007/s005310000083>.
- Schedl, A. & Lipiarski, P. 2021. *Bundesweiter Ressourcenkatalog für Sekundärrohstoffe aus der Rohstoffgewinnung und -aufbereitung (Bergbau-, Aufbereitungshalden)* "Haldenressourcenkatalog": Abschlussdokumentation, Datenlieferung: Jahresbericht 2020.
- Schmid, S.M., Fügenschuh, B., Kissling, E. & Schuster, R. 2004. Tectonic map and overall architecture of the Alpine orogen. *Eclogae Geologicae Helvetiae*, **97**, 93–117, <http://doi.org/10.1007/s00015-004-1113-x>.
- Schneider, C.A., Rasband, W.S. & Eliceiri, K.W. 2012. NIH Image to ImageJ: 25 years of image analysis. *Nature methods*, **9**, 671–675, <http://doi.org/10.1038/nmeth.2089>.
- Steadman, J.A. & Large, R.R. *et al.* 2021. Pyrite trace element behavior in magmatic-hydrothermal environments: An LA-ICPMS imaging study. *Ore Geology Reviews*, **128**, 103878, <http://doi.org/10.1016/j.oregeorev.2020.103878>.
- Stepanov, A.S., Large, R.R., Kiseeva, E.S., Danyushevsky, L.V., Goemann, K., Meffre, S., Zhukova, I. & Belousov, I.A. 2021. Phase relations of arsenian pyrite and arsenopyrite. *Ore Geology Reviews*, **136**, 104285, <http://doi.org/10.1016/j.oregeorev.2021.104285>.

- Strauss, P., Wagreeich, M., Decker, K. & Sachsenhofer, R.F. 2001. Tectonics and sedimentation in the Fohnsdorf-Seckau Basin (Miocene, Austria): from a pull-apart basin to a half-graben. *International Journal of Earth Sciences*, **90**, 549–559, <http://doi.org/10.1007/s005310000180>.
- Strauss, P.E., Daxner-Höck, G. & Wagreeich, M. 2003. *Lithostratigraphie, Biostratigraphie und Sedimentologie des Miozäns im Fohnsdorfer Becken (Österreich)*. In: PILLER W. E. (Ed.): *Stratigraphia Austriaca*.
- Sung, Y.-H., Brugger, J., Ciobanu, C.L., Pring, A., Skinner, W. & Nugus, M. 2009. Invisible gold in arsenian pyrite and arsenopyrite from a multistage Archean gold deposit: Sunrise Dam, Eastern Goldfields Province, Western Australia. *Mineralium Deposita*, **44**, 765–791, <http://doi.org/10.1007/s00126-009-0244-4>.
- Tang, Q., Di, P., Yu, M., Bao, J., Zhao, Y., Liu, D. & Wang, Y. 2019. Mineralogy and Geochemistry of Pyrite and Arsenopyrite from the Zaozigou Gold Deposit in West Qinling Orogenic Belt, Central China: Implications for Ore Genesis. *Resource Geology*, **69**, 314–332, <http://doi.org/10.1111/rge.12203>.
- Tessema, D.A., Mogessie, A. & Kosmus, W. 2011. Arsenopyrite Weathering and Leaching of Arsenic in an Austrian Soil. *Soil and Sediment Contamination: An International Journal*, **20**, 550–563, <http://doi.org/10.1080/15320383.2011.587044>.
- Torró, L., Benites, D., Vallance, J., Laurent, O., Ortiz-Benavente, B.A., Chelle-Michou, C., Proenza, J.A. & Fontboté, L. 2022. Trace element geochemistry of sphalerite and chalcopyrite in arc-hosted VMS deposits. *Journal of Geochemical Exploration*, **232**, 106882, <http://doi.org/10.1016/j.gexplo.2021.106882>.
- Vermeesch, P. 2018. IsoplotR: A free and open toolbox for geochronology. *Geoscience Frontiers*, **9**, 1479–1493, <http://doi.org/10.1016/j.gsf.2018.04.001>.
- Weber, L. 1990. *Die Blei-Zinkerzlagertstätten des Grazer Paläozoikums und ihr geologischer Rahmen: Mit 25 Tabellen*. Geologische Bundesanstalt, Wien.
- Weber, L., Schedl, A. & Lipiarski, P. 2019. IRIS Online (Interaktives Rohstoff Informations System), ein Beispiel für ein weltweit einzigartiges digitales Rohstoff-Informationssystem. *BHM Berg- und Hüttenmännische Monatshefte*, **164**, 56–66, <http://doi.org/10.1007/s00501-018-0810-0>.
- Wen, Q., Yang, X., Yan, X. & Yang, L. 2022. Evaluation of arsenic mineralogy and geochemistry in gold mine-impacted matrices: Speciation, transformation, and potential associated risks. *Journal of Environmental Management*, **308**, 114619, <http://doi.org/10.1016/j.jenvman.2022.114619>.
- Wilson, S.A., Ridley, W.I. & Koenig, A.E. 2002. Development of sulfide calibration standards for the laser ablation inductively-coupled plasma mass spectrometry technique. *Journal of Analytical Atomic Spectrometry*, **17**, 406–409, <http://doi.org/10.1039/B108787H>.
- Wu, Y.-F., Fougereuse, D., Evans, K., Reddy, S.M., Saxey, D.W., Guagliardo, P. & Li, J.-W. 2019. Gold, arsenic, and copper zoning in pyrite: A record of fluid chemistry and growth kinetics. *Geology*, **47**, 641–644, <http://doi.org/10.1130/G46114.1>.
- Xie, Z. & Gopon, P. *et al.* 2024. Does SW China have Carlin-type gold deposits? A micro- to atomic-scale perspective. *Mineralium Deposita*, **59**, 757–772, <http://doi.org/10.1007/s00126-023-01231-6>.

## Abbreviations

Apy	Arsenopyrite
Bn	Bournonite
Bou	Boulangerite
BSE	Back-scattered electron detector
Ccp	Chalcopyrite
CRM	Critical Raw Material
EDS	Energy dispersive spectrometer
EI	Electrum
EPMA	Electron probe micro analyzer
Fm.	Formation
Gn	Galena
ICP	Inductively coupled plasma
ICP-MS	Inductively coupled plasma mass spectrometry
LA-ICP-MS	Laser ablation inductively coupled plasma mass spectrometry
LOD	Lower detection limit
Py	Pyrite
Qz	Quartz
SEM	Scanning electron microscope
SRM	Strategic Raw Material
WDS	Wavelength dispersive spectrometer

(mineral abbreviations after Warr 2021)

## List of Figures

- Figure 1: Straßegg (marked with a red dot) in Styria (in green) in Austria; (Basemap: OSM, 2023). \_\_\_ 3
- Figure 2: The Graz Paleozoic modified after Gasser et al. (2010); a) shows an overview of the tectonic units of the Eastern Alps; b) shows the Graz Paleozoic nappe complex. The red dot marks the location of Straßegg. \_\_\_\_\_ 4
- Figure 3: Nappes and units of the Graz Paleozoic nappe complex modified after Ebner et al. (2001), formation is abbreviated with fm. Straßegg is part of the Schöckel nappe (Bojar et al., 2001); 1) Kehr-fm., Kötschberg fm.; 2) Parmasegg fm.; 3) Flösserkogel fm., Bameder fm.; 4) Barrandeikalk; 5) Kollerkogel fm.; 6) Steinberg fm.; 7) Sanzenkogel fm.; 8) Höchkogel fm.; Hahngraben fm.; 9) Tyrnaueralm fm.; 10) Zachenspitz fm., Hochlantsch fm.; 11) Bärenschtütz fm.; 12) Hackensteiner fm., 13) Harrberger fm.; 14) St. Jakob fm.; 15) Dornerkogel fm.; 16) Kogler fm.; 17) Hubenhalt fm.; 18) Taschen fm.; 19) Schönberg fm.; 20) Schöckel fm., Hochschlag fm. \_\_\_\_\_ 5
- Figure 4: Geological map of Straßegg modified after Antes (1998), mining artefacts can be found within the Pramerkogel formation. \_\_\_\_\_ 8
- Figure 5: Geologic map of the Murtal after Raith et al. (2015); the area of Flatschach is marked within a green box. \_\_\_\_\_ 12
- Figure 6: Paragenetic table of the Cu-Au mineralization in Flatschach after Raith et al. (2015). \_\_\_\_\_ 13
- Figure 7: Photos of samples; a) sample 22JH07, which originates of a mine waste facility, shows an ore in quartz; b) sample 22JH10 is a float sample, which shows in quartz disseminated ores. These ores are mostly arsenopyrite, minor pyrite. \_\_\_\_\_ 14
- Figure 8: Map of the sample location; Lithology of Straßegg modified after Antes (1998); (Basemap: Esri satellite 2023). \_\_\_\_\_ 21
- Figure 9: Whole rock geochemistry element correlation. Each graph shows three elements compared to each other. Two elements are on the axis, the third is depicted by the color bar. Measurements below LOD were taken as one half of the LOD. The LOD range (on elements of the axis) are marked within the grey fields. In each graph an attempt was made to model a best fit function. a) Ag vs. Au in dependence of As; b) Ag vs. Au in dependence of Pb; c) Ag vs. Au in dependence of Cu; d) Ag vs. Cu in dependence of Pb; e) Ag vs. Cu in dependence of As; f) Pb vs. Cu in dependence of As; g) Ge vs. Ga in dependence of As; h) Ge vs. Ga in dependence of Pb. \_\_\_\_\_ 28
- Figure 10: Whole rock geochemistry element correlation. Each graph shows three elements compared to each other. Two elements are on the axis, the third is depicted by the color bar. Measurements below LOD were taken as one half of the LOD. The LOD range (on elements of the axis) are marked within the grey fields. In each graph an attempt was made to model a best fit function. a) Co vs. Ni in dependence of As; b) Co vs. Ni in dependence of Pb; c) Co vs. Ni in dependence of Au; d) Ag vs. Sb in dependence of Cu; e) Ag vs. Sb in dependence of As; f) Ag vs. Sb in dependence of Pb; g) Au vs. Sb in dependence of As; h) Au vs. Sb in dependence of Pb. \_\_\_\_\_ 29
- Figure 11: Whole rock geochemistry element correlation. Each graph shows three elements compared to each other. Two elements are on the axis, the third is depicted by the color bar. Measurements below LOD were taken as one half of the LOD. The LOD range (on elements of the axis) are marked within the grey fields. In each graph an attempt was made to model a best fit function. a) V vs. Mn in dependence of As; b) V vs. Mn in dependence of Pb; c) V vs. Cr in dependence of Mn; d) Cr vs. Ni in dependence of Co; e) Te vs. Se in dependence of As; f) Te vs. Se in dependence of Pb; g) Ag vs. Zn in dependence of As; h) Ag vs. Zn in dependence of Pb. \_\_\_\_\_ 30
- Figure 12: Whole rock geochemistry element correlation. Each graph shows three elements compared to each other. Two elements are on the axis, the third is depicted by the color bar. Measurements below LOD were taken as one half of the LOD. The LOD range (on elements of the axis) are marked within the grey fields. In each graph an attempt was made to model a best fit function. a) Bi vs. Au in dependence of As; b) Bi vs. Au in dependence of Pb; c) Cd vs. In in dependence of Cu; d) Cd vs. Zn in dependence of Cu. \_\_\_\_\_ 31
- Figure 13: Overview pictures of the polished round mounts; a) Sample 22JH07a - major components massive arsenopyrite vein, with smaller vein, which consist of disseminated arsenopyrite cross-cutting

it; b) sample 22JH07b -disseminated arsenopyrite; c) sample 22JH08a - disseminated arsenopyrite; d) sample 22JH09a major components are arsenopyrite, pyrite and boulangerite; e) sample 22JH09b - containing mostly disseminated arsenopyrite; f) sample 22JH10 - major component veins and disseminated arsenopyrite, minor occurs pyrite and electrum as well as Pb-inclusions. \_\_\_\_\_ 33

Figure 14: Overview pictures of the polished round mounts; a) Sample 22JH14a - major component is disseminated arsenopyrite; b) sample 22JH14b - arsenopyrite and pyrite are disseminated, galena occurs as minor component; c) sample 22JH014c - major component disseminated arsenopyrite; d) sample 22JH29a - veinlets of arsenopyrite, relatively abundant inclusions of especially electrum but as well Pb-phases; e) sample 22JH31a - consist mainly of arsenopyrite, chalcopyrite and pyrite, partly altered; f) sample 22JH34b - arsenopyrite and pyrite surrounded not just of quartz but as well of feldspars and mica. \_\_\_\_\_ 34

Figure 15: Overview pictures of the polished round mounts; a) sample A0976 - most abundant is galena, minor arsenopyrite; b) sample A0977 - pyrite together with boulangerite and minor arsenopyrite; c) sample A0978 – most abundant is boulangerite, minor arsenopyrite and pyrite; d) sample A0979 - arsenopyrite (mostly the smaller crystals) surrounding pyrite (bigger crystals) disseminated; e) sample A0980 - major component disseminated arsenopyrite; f) sample A0981- most abundant are arsenopyrite and pyrite. \_\_\_\_\_ 35

Figure 16: Overview picture sample A0982 - arsenopyrite, pyrite, bournonite, boulangerite and galena occur together as massive mineralization or in form of veinlets. \_\_\_\_\_ 36

Figure 17: Microscopy pictures of sample 22JH07a; a) Arsenopyrite (apy) with Pb-Sb-As-(Cu)-(Fe) inclusions, gangue mineral is quartz (qz); b) Arsenopyrite (apy) is dissected by an As-Fe-O phase (arrow), gangue mineral is quartz (qz). \_\_\_\_\_ 37

Figure 18: Zonation styles in sample 22JH07b and 22JH08; a) shows a concentric zoning in sample 22JH07b with a thickness size partly >100 µm. This crystal was also analyzed during the EPMA session (see Chapter 4.4.2 EPMA element map 22JH07b).; b) Shows a Sb-bearing arsenopyrite concentric zoning in sample 22JH08a. \_\_\_\_\_ 37

Figure 19: Sample 22JH09a; a) shows an BSE image of several veinlet generations in the sample; b) is an enlarged picture showing arsenopyrite (apy) and pyrite (py), which have been overgrowth by boulangerite (bou), cross-cutted by different Pb-veinlets; c) microscopy photo of arsenopyrite (apy) crosscut by boulangerite (bou); d) shows the BSE image of a zoned and fractured arsenopyrite(apy) in boulangerite (bou). \_\_\_\_\_ 38

Figure 20: Sample 22JH09b; a) BSE image of a fractured arsenopyrite (apy); b) show an enlarged part with Pb-As-S inclusions. The zonation in the arsenopyrite are rectangular, in several rims; b) arsenian pyrite (py) with concentric zoning and arsenopyrite inclusions. Pyrite is less abundant in the sample than arsenopyrite. \_\_\_\_\_ 39

Figure 21: Sample 22Jh10; a) microscope photo of pyrite(py) overgrowing arsenopyrite (apy); b) BSE image of the pyrite which contains several inclusion of Pb-phases or electrum(el); c) BSE image of the arsenopyrite with oscillatory zoning. This crystal was used during EPMA mapping BSE; d) image of a triangle zonation in a arsenopyrite(apy); the brighter parts contain less S compared to the darker parts. \_\_\_\_\_ 40

Figure 22: Sample 22JH14a; BSE image of a diffused and spotty zoned arsenopyrite (apy). The core seems totally unaffected by the zonation. \_\_\_\_\_ 41

Figure 23: Sample 22JH14b; a) BSE image of pyrite (py) crystal, zonation is diffuse in the crystal, arsenopyrite is in the surrounding. The pyrite was mapped with LA-ICP-MS (see Chapter 4.5.4 LA-ICP-MS element map 22JH14b-map 1); pyrite (py) contains in other parts of the sample often Pb-inclusions, best visible in the BSE image; c) another pyrite, that was mapped with LA-ICP-MS (see Chapter 4.5.5 LA-ICP-MS element map 22JH14b-map 2), the core is darker, the rim instead brighter. \_\_\_\_\_ 41

Figure 24: Sample 22JH14c; microscope photos of a) arsenopyrite (apy) veinlet and b) electrum (el) between disseminated arsenopyrite (apy). \_\_\_\_\_ 42

Figure 25: Sample 22JH29b; a) microscope photo of electrum (el) inclusions in arsenopyrite (apy); b) the BSE image shows the location of the inclusion in an arsenopyrite (apy), SEM results in Table 9. \_\_\_\_\_ 42



Figure 26: Sample 22JH31a; a) microscope photo of chalcopyrite (ccp), altered at fractures; b) microscope photo of slightly altered chalcopyrite (ccp) surrounding an idiomorph arsenopyrite (apy); c) BSE image of a zoned pyrite (py). Bright spots in the image are often Pb-phases. _____	44
Figure 27: Sample A0976; a) fractured arsenopyrite (apy) in the vicinity of galena (gn). The arsenopyrite is more affected by alterations; b) shows galena (gn) as fracture filling element in the gangue mineral quartz (qz). _____	44
Figure 28: Sample A0979; a) BSE image of pyrite (py) and arsenopyrite (apy) in quartz (qz). Arsenopyrite is altered on the edges of the crystal, inclusions are enriched mainly in Pb and Sb; b) BSE image of fracture in quartz (qz); in the junction is Pb-oxide enriched, As-Fe-O is filling the fractures. _____	45
Figure 29: Sample A0980; a) shows the alteration of an arsenopyrite (apy) by an As-Fe-O phase. Pb-phases are enriched at the rims; b) arsenopyrite with an electrum inclusion. _____	46
Figure 30: Sample A0982; a) microscopic photo of bournonite (bn), boulangerite (bou) and galena (gn) overgrowing arsenopyrite (apy); b) shows an insight of the minerals in the backscatter image. _____	47
Figure 31: Sample A0982; microscope picture of an fractured pyrite (py). The filling in the fracture consist of an Ag-Pb-phase. The pyrite includes as well arsenopyrite (apy). This pyrite was partly mapped during the LA-ICP-MS mapping sessions (red box) (see Chapter 4.5.3 LA-ICP-MS element map A0982-map 2). _____	47
Figure 32: Arsenopyrite element maps in sample 22JH08a; a) BSE image; b) Ag EDS spectrometer; c) As WDS spectrometer; d) Au WDS spectrometer; e) Co EDS spectrometer; f) Cu EDS spectrometer; g) Fe EDS spectrometer; h) Ni WDS spectrometer; i) Pb EDS spectrometer; j) S EDS spectrometer; k) Sb WDS spectrometer. _____	49
Figure 33: Arsenopyrite element maps in sample 22JH07b; a) BSE image; b) Ag EDS spectrometer; c) As WDS spectrometer; d) Au WDS spectrometer; e) Co EDS spectrometer; f) Cu EDS spectrometer; g) Fe EDS spectrometer; h) Ni WDS spectrometer; i) Pb EDS spectrometer; j) S EDS spectrometer; k) Sb WDS spectrometer. _____	51
Figure 34: Arsenopyrite element maps in sample 22JH14b-1; a) BSE image; b) Ag EDS spectrometer; c) As WDS spectrometer; d) Au WDS spectrometer; e) Co EDS spectrometer; f) Cu EDS spectrometer; g) Fe EDS spectrometer; h) Ni WDS spectrometer; i) Pb EDS spectrometer; j) S EDS spectrometer; k) Sb WDS spectrometer. _____	53
Figure 35: Arsenopyrite element maps in sample 22JH14b-map 2; a) BSE image; b) Ag EDS spectrometer; c) As WDS spectrometer; d) Au WDS spectrometer; e) Co EDS spectrometer; f) Cu EDS spectrometer; g) Fe EDS spectrometer; h) Ni WDS spectrometer; i) Pb EDS spectrometer; j) S EDS spectrometer; k) Sb WDS spectrometer. _____	54
Figure 36: Arsenopyrite element maps in sample 22JH10; a) BSE image; b) Ag EDS spectrometer; c) As WDS spectrometer; d) Au WDS spectrometer; e) Co EDS spectrometer; f) Cu EDS spectrometer; g) Fe EDS spectrometer; h) Ni WDS spectrometer; i) EDS spectrometer; j) S EDS spectrometer; k) Sb WDS spectrometer. _____	56
Figure 37: Pyrite LA-ICP-MS element map 22JH31a; a) BSE image; b) $^{107}\text{Ag}$ ; c) $^{75}\text{As}$ ; d) $^{197}\text{Au}$ ; e) $^{209}\text{Bi}$ ; f) $^{63}\text{Cu}$ ; g) $^{71}\text{Ga}$ ; h) $^{115}\text{In}$ ; i) $^{95}\text{Mo}$ ; j) $^{60}\text{Ni}$ ; k) $^{208}\text{Pb}$ ; l) $^{121}\text{Sb}$ ; m) $^{118}\text{Sn}$ ; n) $^{66}\text{Zn}$ . _____	59
Figure 38: Pyrite LA-ICP-MS element map A0982-map 1; a) BSE image; b) $^{107}\text{Ag}$ ; c) $^{75}\text{As}$ ; d) $^{197}\text{Au}$ ; e) $^{59}\text{Co}$ ; f) $^{63}\text{Cu}$ ; g) $^{60}\text{Ni}$ ; h) $^{208}\text{Pb}$ ; i) $^{121}\text{Sb}$ ; j) $^{118}\text{Sn}$ . _____	60
Figure 39: Pyrite LA-ICP-MS element map A0982-map 2; a) BSE image; b) $^{107}\text{Ag}$ ; c) $^{75}\text{As}$ ; d) $^{197}\text{Au}$ ; e) $^{209}\text{Bi}$ ; f) $^{59}\text{Co}$ ; g) $^{63}\text{Cu}$ ; h) $^{71}\text{Ga}$ ; i) $^{74}\text{Ge}$ ; j) $^{115}\text{In}$ ; k) $^{60}\text{Ni}$ ; l) $^{208}\text{Pb}$ ; m) $^{121}\text{Sb}$ ; n) $^{118}\text{Sn}$ ; o) $^{205}\text{Tl}$ ; p) $^{66}\text{Zn}$ . _____	62
Figure 40: Pyrite LA-ICP-MS element map 22JH14-map 1; a) BSE image; b) $^{107}\text{Ag}$ ; c) $^{75}\text{As}$ ; d) $^{197}\text{Au}$ ; e) $^{59}\text{Co}$ ; f) $^{63}\text{Cu}$ ; g) $^{60}\text{Ni}$ ; h) $^{208}\text{Pb}$ ; i) $^{121}\text{Sb}$ ; j) $^{118}\text{Sn}$ ; k) $^{66}\text{Zn}$ . _____	64
Figure 41: Pyrite LA-ICP-MS element map 22JH14-map 2; a) BSE image; b) $^{107}\text{Ag}$ ; c) $^{75}\text{As}$ ; d) $^{197}\text{Au}$ ; e) $^{59}\text{Co}$ ; f) $^{63}\text{Cu}$ ; g) $^{115}\text{In}$ ; h) $^{60}\text{Ni}$ ; i) $^{208}\text{Pb}$ ; j) $^{121}\text{Sb}$ ; k) $^{118}\text{Sn}$ ; n) $^{66}\text{Zn}$ ; m) $^{66}\text{Zn}$ . _____	65
Figure 42: a) Overview picture of sample 22JH11a; b) Tera-Wasserburg plot for sample 22JH11a (Straßegg). _____	69
Figure 43: a) Overview picture of sample 22GS52a; b) Tera-Wasserburg plot for sample 22GS52a. _	70
Figure 44: a) Overview picture of sample 22GS52b; b) Tera-Wasserburg plot for sample 22GS52b. _	70

Figure 45: a) Overview picture of sample 22GS52d; b) Tera-Wasserburg plot for sample 22GS52d, orange calcite and c) veinlet. _____	71
Figure 46: a) Overview picture of sample F562 with b) Tera-Wasserburg plot for the sample. _____	72
Figure 47: a) Overview of sample FL-CA-1; b) and c) are detailed photos of the different veins. _____	72
Figure 48: Tera-Wasserburg plots for FL-CA-1, a) shows the orange calcite; b) the rim of the orange calcite; c) shows the age of the small calcite veinlets in the orange calcite, d) is the age of the clear calcite veinlet; e) the red veinlet and f) the reddish veinlet. Compare with Figure 47. _____	73
Figure 49: a) Overview picture of sample F441 with Tera-Wasserburg plots for the sample b) yellow calcite 1; c) calcite which contains sulfides. The Tera-Wasserburg plot for the white calcite can be found in the appendix. _____	74
Figure 50: a) Overview picture of sample FL-AG-1 with Tera-Wasserburg plots for the sample b) white calcite 1; c) white calcite 2; d) white calcite 3; e) yellow calcite. The Tera-Wasserburg plot for the red veinlet can be found in the appendix. _____	76
Figure 51: a) Mudtank analyses for ALL analytical sessions; b) Duffbrown analyses for ALL analytical sessions. _____	78
Figure 52: Ore stage generations in arsenopyrite and pyrite; a) BSE image of map 22JH08a (arsenopyrite), indicating the primary Apy-1 and the later stage Apy-2. b) BSE image of map A0982-map 2 (pyrite) shows Py-0 to Py-2. _____	82
Figure 53: Cd:Zn ratio (n=9) of the results of the chalcopyrite in-situ spot analyses, correlated to the Cd:Zn ratios assigned to different types of deposits (after Duran et al., 2019, George et al., 2016). _	85
Figure 54: Genetic table of the elements that have been observed. Suggestions are following the occurrence of elements in the EPMA and LA-ICP-MS. _____	86
Figure 55: Genetic table of the minerals that have been observed in Straßegg (Table 7) with additional emergence of electrum which is probably related to remobilization processes. _____	87

## List of Tables

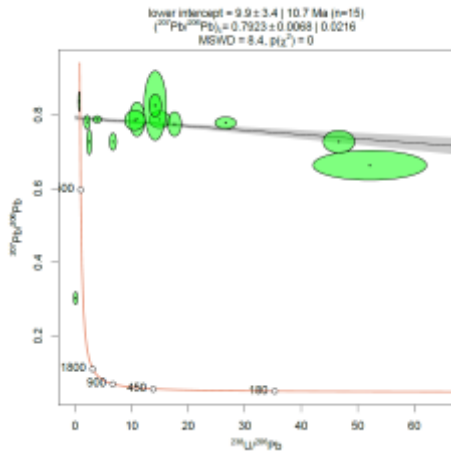
Table 1: Petrographic description of the formations in Straßegg modified after Antes (1998) and Bojar et al. (2001).	7
Table 2: Paragenetic table after Bojar et al. (1994) and Bojar et al. (1998). Main minerals that occur are assigned to the ore stages.	10
Table 3: Samples list and which methods were conducted on them marked with an “x”.	16
Table 4: EPMA spectrometer adjustments for element mapping on arsenopyrite.	17
Table 5: Sample ID, location, sampler, and description of the type. Samples of the Paar collection (A0976-A0982) have no distinct coordinates and are described to originate by a mine waste facility.	22
Table 6: Selected results of the whole rock geochemistry analysis. Samples 21TB01 to 02 and 21TB03 to 22JH34a have different detection limits and are analyzed in different laboratories. For further information see Chapter 3 and the appendix. The median value of the content is used to prevent strong influence by extrem outliers, for samples which do not reach the detection limit, half of the LOD was used.	25
Table 7: Most abundant minerals in the different epoxide mounts; (XXX) high abundance of the mineral; (xx) moderate abundance; (x) low abundance.	32
Table 8: Examples measurements of the zonation in arsenopyrite in Figure 21;a) 22JH10 20-21 refer to the dark zonation; 22JH10 22-23 to the brighter zone.	39
Table 9: SEM results of the inclusions in an arsenopyrite in sample 22JH29b (location can be found in Figure 25).	43
Table 10: Example of gradually element distribution in mass% in sample A0982. From measurement A0982 48 to A0982 50 the element distribution of Cu and Sb increases, while the Pb content decreases.	47
Table 11: Chalcopyrite in-situ spot analyses statistics with suspected inclusions. Mean value, P95, P05, N (number of individual analyses with the LA-ICP-MS) and n (number of analyses below the LOD) and the mean value of the LOD depicted. The mean value, P95 and P05 are in ppm.	67
Table 12: Chalcopyrite in-situ spot analyses statistics with deleted suspected inclusions. Mean value, P95, P05, N (number of individual analyses with the LA-ICP-MS), n (number of analyses below the LOD) and the mean value of the LOD. The mean value, P95 and P05 are in ppm.	68
Table 13: Final selected samples for U/Pb calcite dating and their location.	69
Table 14: Summary of the age dates (Straßegg and Flatschach).	77
Table 15: Primary reference material WC-1 carbonate in ALL sessions.	78
Table 16: Suggested ore stages of the mineralization in Straßegg. Beginning with a pre-ore stage which mainly consists of the pyrite generation Py-0. Followed by ore stage 1 which comprises the pyrite generations Py-1, Py-2, and arsenopyrite generation Apy-1 to Apy-2. Ore stage 1 can be subdivided into a and b. Ore stage 2 consists mainly of the occurrence of Cu in three different element assemblages. The first generation of ore stage 2 is Ag-Cu-Zn-1, where the occurrence of chalcopyrite is assigned to, to a probably intermediate stage of Bi-Ga-In-1 and finally Bn-1 with the occurrence of bournonite. This element assemblages marks the beginning transition to ore stage 3, which is dominated by Bou-1, with the main mineral boulangerite, and later Gn-1, which consists of galena. Post-ore mineralization can be assumed El-1, due to the formation of gold nanoparticles in form of electrum. Other remobilizations of elements occur due to the oxidation of arsenopyrite or Pb-phases.	83
Table 17: Chalcopyrite spot analysis results of the elements Cd and Zn. Measurements suspected as inclusions have been avoided. The ratio between both elements can be found on the right side.	84
Table 18: Age results of Flatschach subdivided into 3 groups according to their age. Age range comes from U/Pb dating of this thesis.	88

# Appendix

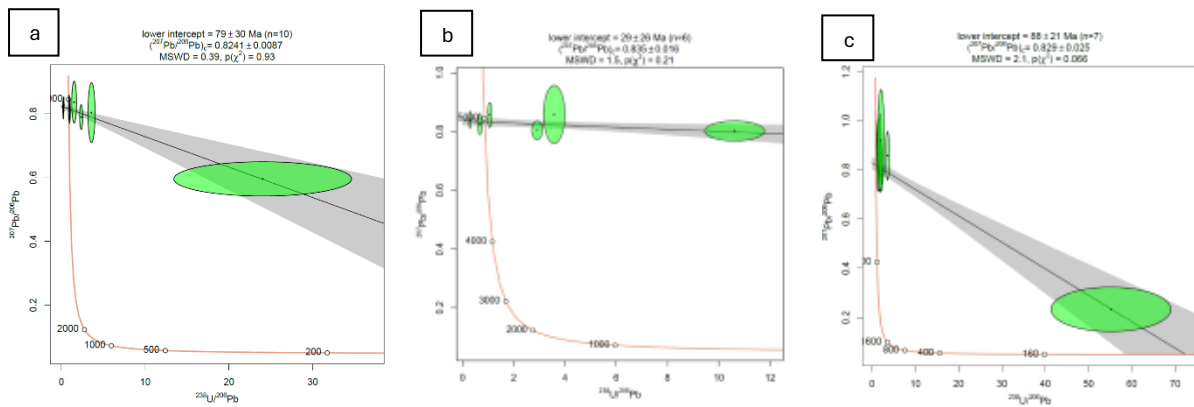
Additional information can be found in the electronic appendix.

## A U/Pb Tera-Wasserburg plots

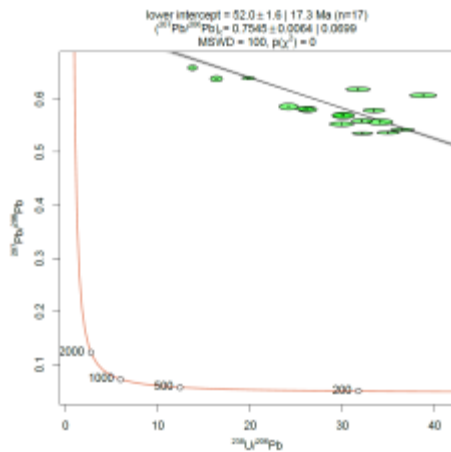
### A1 22GS52d white



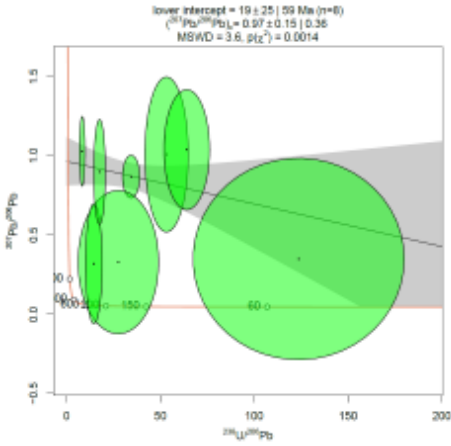
### A2 FL CA 1 White (separated in a) Analyse 1-10, b) analyses 11-17 and c) 18-22)



### A3 FL AG red



A4 F441 white





## Electronic Appendix

In the electronic appendix can the raw data of this thesis be found.

The folder is named “MA\_Hiller\_Appendix”. It contains the several subfolders.

Subfolders are

- Whole rock geochemistry (Excel sheet of data)
- Microcopy (Photos of the samples)
- SEM (BSE Images and analyses)
- EPMA (Data of the arsenopyrite maps)
- LA-ICP-MS (Data of the pyrite maps and chalcopyrite spot analysis)
- U-Pb age dating (Excel sheet of the results and raw data of the sessions)